Chair of Subsurface Engineering

Master`s Thesis

3D Finite Element Analysis of building lot "Wolframstraße"

Andreas-Nizar Granitzer, BSc

November 2019

EIDESSTATTLICHE ERKLÄRUNG

Ich erkläre an Eides statt, dass ich diese Arbeit selbständig verfasst, andere als die angegebenen Quellen und Hilfsmittel nicht benutzt, und mich auch sonst keiner unerlaubten Hilfsmittel bedient habe.

Ich erkläre, dass ich die Richtlinien des Senats der Montanuniversität Leoben zu "Gute wissenschaftliche Praxis" gelesen, verstanden und befolgt habe.

Weiters erkläre ich, dass die elektronische und gedruckte Version der eingereichten wissenschaftlichen Abschlussarbeit formal und inhaltlich identisch sind.

Datum 01.11.2019

Andreas Granitzer

Unterschrift Verfasser/in
Andreas-Nizar, Granitzer

Danksagung

Die Erstellung der Masterarbeit erfolgte gemäß dem Slogan eines namhaften heimischen Baukonzerns “TEAMS WORK”, welcher mir eine Vielzahl an neuen Perspektiven eröffnet hat, für die ich sehr dankbar bin.

Dem Kernteam, bestehend aus Ass.-Prof. Dipl.-Ing. Dr.techn. Franz Tschuchnigg, Dipl.-Ing. Dr.mont. Thomas Stoxreiter und Dipl.-Ing. Wolfgang Summerer, gilt mein ganz besonderer Dank. Eine Zusammenarbeit in dieser Qualität, über die Landes-, Unternehmens- und Universitätsgrenzen hinweg, hat - zumindest für mich - neue Maßstäbe gesetzt.

Dem Team „Subsurface Engineering“ der Montanuniversität Leoben, bestehend aus Univ.-Prof. Dipl.-Ing. Dr.mont. Robert Galler, Dipl.-Ing. Erik Schuller, Dipl.-Ing. Robert Wenighofer, Nadja Juritsch, Michaela Schmid und Jörg Krainz, gilt mein Dank ebenso für die hervorragende Betreuung während der gesamten Studienzeit.

Dem Team „Geotechnik“ der ILF Consulting Engineers Austria in Rum bei Innsbruck bestehend aus Dipl.-HTL-Ing. Andreas Spiegl, Dipl.-Ing. Sebastian Höser, Ing. Vladimir Bartos PhD, Dr.techn. Iman Bathaeian M.Sc., Dipl.-Ing. Christian Volderauer, Dipl.-Ing. Hannah Goettgens, Dipl.-Ing. Nina Obereder, Dipl.-Ing. Stefan Baier, Dipl.-Ing. Beatrice Hildebrand, Dipl.-Ing. Atieh Mirzaei und Dipl.-Ing. Frank Remmert gilt mein Dank für das vorgelebte Verständnis von Teamwork.

Zu guter Letzt möchte ich mich ganz besonders bei meinen Eltern und Freunden bedanken, die meine Faszination für die ihnen häufig fremden Themen geduldet und viel mehr noch gefördert haben. Dankeschön!

Leoben, November 2019 Andreas Granitzer

Kurzfassung

3D Finite-Elemente-Analyse des Bauloses “Wolframstraße”

In dieser Arbeit wird der Einfluss der Herstellung einer unterirdischen Eisenbahntrasse auf das Deformationsverhalten und die Schnittgrößen eines darunter angrenzenden Drainagetunnels im Baulos „Wolframstraße“ untersucht. Zuerst erfolgt die Bestimmung anisotroper Modellierungsparameter des Tunnels, welche im Anschluss zur detaillierten Untersuchung seines Strukturverhaltens während der Bauphase zur Anwendung kommen. Die numerischen Untersuchungen erfolgten dabei mittels der FE Software PLAXIS.

Das Strukturverhalten schildvorgetriebener Tunnel wird maßgeblich durch die Tübbing-Fugen beeinflusst. Zur besseren Abschätzung der auftretenden Deformationen und Schnittgrößen des Tunnels können anisotrope Modellierungsansätze herangezogen werden. Im Rahmen einer Vorstudie wurde daher ein Leitfaden zur Bestimmung der anisotropen Modellierungsparameter des Drainagetunnels entwickelt. Dabei wird dem Einfluss der Fugen sowohl durch explizite Modellierung als auch durch den Ansatz „verschmierter“ Steifigkeiten Rechnung getragen. In der Vorstudie wird das Be- und Entlastungsverhalten separat untersucht, da der gegenständliche Drainagetunnel im Zuge der Bauarbeiten beide Belastungssituationen aufweist. Die Ergebnisse führten bei der betrachteten Tunnelgeometrie zu dem Schluss, dass die Rotationssteifigkeit der Längsfugen keinen Einfluss auf das Querschnittsverhalten des Tunnels hat. Im Gegensatz dazu ließen die Ergebnisse darauf schließen, dass das axiale Strukturverhalten durch die Ringfugen signifikant beeinflusst wird. Zudem zeigte sich ein wesentlicher Einfluss der gewählten Schubsteifigkeit in der Ringfuge auf die Schnittgrößen der Tübbingsegmente, wobei unterschiedliche Tendenzen bei Be- und Entlastung auftraten.

Die komplexe Geometrie des betrachteten Projektes erforderte eine dreidimensionale Betrachtung der einzelnen Bauphasen. Eine Baustellenbesichtigung vor Ort bildete die Basis zur Bestimmung relevanter Modellierungsrandbedingungen (z.B. Berücksichtigung benachbarter Gebäude im direkten Einflussbereich der Baustelle). Das Bauvorhaben führte zur Hebung des gesamten Drainagetunnels, wobei die größten Firsthebungen im Bereich der Baugrube auftraten. Die maximalen Biegemomente des Tunnelquerschnittes stellten sich vor dem Endbauzustand ein, weshalb eine genauere Betrachtung der Zwischenbauzustände notwendig war. Der erhöhte Abfluss bei starken Regenfällen wurde durch einen radialen Innendruck im Tunnel berücksichtigt und führte zur Setzung des gesamten Drainagetunnels.

Abstract

3D Finite Element Analysis of building lot “Wolframstraße”

The objective of this thesis is to analyse the structural response of the existing drainage tunnel HWS to the excavation of the suburban railway project “Wolframstraße” conducted above the tunnel axis. Of main concern are the determination of anisotropic lining parameters as well as the structural performance during different construction phases using the FE software PLAXIS.

Due to the presence of construction joints, shield-driven tunnel linings, such as the HWS, are expected to behave anisotropic rather than isotropic. A parameter derivation process, which poses the core of the preliminary study, is therefore established in order to model the structural behaviour of the tunnel lining as realistically as possible. To this end, the lining is considered as direct-joint model as well as indirect-joint model. For the latter, the basic idea of adapting the stiffness components of the lining as a consequence of segmental joints is discussed in detail. In addition, a distinction is made between loading and unloading conditions to account for the actual spatial boundary conditions of the HWS. The results showed that the cross-sectional behaviour of the concerned lining configuration is not affected by the rotational stiffness of the longitudinal joints at all. In contrast, ring joints were expected to affect the longitudinal deformation behaviour significantly. Similarly, the structural forces of the lining were particularly influenced by the ring joint-induced shear stiffness reduction. However, different tendencies were observed for loading and unloading conditions.

As a consequence of both, the complex geometrical conditions and the construction program of the considered project, full 3D modelling was required. The results of the performed sensitivity study underlined the importance of the considered model dimensions on the calculation output. To this end, the model depth was validated based on the distribution of the Small Strain Stiffness ratio. The results showed that the heave of the tunnel crown decreases as the distance between the excavation axis and the tunnel increases. Moreover, the structural behaviour of the lining appeared to be less affected as the above excavation proceeds. It was further inferred from the results that the structural forces significantly vary between the construction phases which might be critical to the lining design. The general response of the lining due to heavy rainfall effects was longitudinal settlement.

Table of contents

1 Introduction 1

1.1 Background 1
1.2 Scope and outline of this thesis 1

2 Complex tunnel lining assembly: Preliminary study 2

2.1 Literature research 3
  2.1.1 General introduction to segmental tunnel linings 3
  2.1.2 Design considerations for segmental tunnel linings 6
  2.1.3 Advanced design of segmental tunnel linings 8
2.2 Modelling approach 17
  2.2.1 Problem definition 17
  2.2.2 Soil conditions and constitutive models 19
  2.2.3 Geometry and calculation phase sequence 20
  2.2.4 HWS model 23
2.3 Results and discussion 34
  2.3.1 Cross-sectional structural behaviour 35
  2.3.2 Longitudinal structural behaviour 40
  2.3.3 Indirect-joint vs. direct-joint modelling 43
  2.3.4 Joint-induced shear stiffness reduction 47
2.4 Implications for large-scale model 50

3 Construction lot “Wolframstraße”: 3D-FEA 54

3.1 Project description and construction process 55
3.2 Modelling Approach 58
  3.2.1 Geometry and mesh configuration 58
  3.2.2 Soil conditions and constitutive model 59
  3.2.3 Structural elements 61
  3.2.4 Calculation phase sequence 65
  3.2.5 Simplification of complex structures 67
3.3 Results and discussion 68
  3.3.1 Sensitivity study 69
  3.3.2 Cross-sectional structural behaviour (HWS) 73

3.3.3 Longitudinal structural behaviour (HWS) 76
3.3.4 Overall structural behaviour 78
3.4 Conclusions and further perspective 82

4 References 86

5 Appendix A 88

6 Appendix B 90

7 Appendix C 92

List of tables

Tab. 1: HWS-related parameters 18
Tab. 2: HWS preliminary study - soil parameters (part A) 19
Tab. 3: HWS preliminary study - soil parameters (Part B) 20
Tab. 4: Specifications of calculation models (2D / “2.5D”) 21
Tab. 5: Overview of performed analyses 34
Tab. 6: Abbreviations used in outputs 34
Tab. 7: Absolute lining displacements (loading conditions) 35
Tab. 8: Absolute lining displacements (unloading conditions) 37
Tab. 9: Relative differences of deformations (different model depths – joint configuration: rigid) 39
Tab. 10: HWS-related input data required to determine $\xi_{Cont.}$ 40
Tab. 11: Lining parameters considered in the 3D FEA of section 2.3.2 41
Tab. 12: Lining parameters considered in the 3D FEA of section 2.3.3 43
Tab. 13: Lining parameters considered in the 3D FEA of section 2.3.4 47
Tab. 14: Recommended lining parameters for the large-scale model 52
Tab. 15: Construction lot “Wolframstraße” - soil parameters 60
Tab. 16: Modelling options considered in large-scale model 68
Tab. 17: Max. crown displacements obtained with different modelling approaches 82
Tab. 18: Absolute lining displacements 91
Tab. 19: Relationship between shear stiffness coefficient ζ_{Joint} and max. cross-sectional bending moment M_{max} of tunnel lining (loading, *HSS*) 91
Tab. 20: Relationship between shear stiffness coefficient ζ_{Joint} and max. cross-sectional bending moment M of tunnel lining (unloading, *HSS*) 91
Tab. 21: Raft foundation parameters 92
Tab. 22: HWS lining parameters (isotropic material behaviour) 92
Tab. 23: HWS lining parameters (anisotropic material behaviour) 92
Tab. 24: Waling parameters 93
Tab. 25: Strut parameters 93
Tab. 26: Massive concrete wall parameters 93
Tab. 27: Soil nail parameters (tunnel stop wall support) 94
Tab. 28: Tunnel stop wall parameters 94
Tab. 29: Roof slab and header bar parameters 95
Tab. 30: Pile wall parameters (explicitly modelled piles) 95
Tab. 31: Pile wall parameters (simplified as diaphragm wall) 95
Tab. 32: Lateral shotcrete wall parameters 96
Tab. 33: Lateral soil nail parameters (*rdb*) 96
Tab. 34: Lateral soil nail parameters (*ldb*) 97
Tab. 35: Reinforced invert parameters 97
Tab. 36: Vertical soil nail parameters (micropiles) 98
Tab. 37: Pre-stressed anchor parameters 98

List of figures

Fig. 1: Straight-jointed assembly (top); stagger-jointed assembly (bottom) (Yu et al., 2019) ... 3
Fig. 2: Definition of lining components (Zhang et al., 2019) ... 4
Fig. 3: Split tensile stresses caused by jack forces (Blom, 2002) ... 4
Fig. 4: Bending moment transfer between adjacent rings (Guan et al., 2015) 5
Fig. 5: Longitudinal joint types (FSV, 2013) ... 5
Fig. 6: Flattening-related tunnel deformations (Lee and Ge, 2001) ... 7
Fig. 7: Typical failure modes of joint waterproofing (Gong et al., 2019) ... 8
Fig. 8: Stiffness reduction of geotechnical structures due to the presence of construction joints (Zdravkovic et al., 2005) ... 9
Fig. 9: Edge values of joint behaviour (left); experimental facility (right) (Faltýnek and Pruška, 2019) ... 11
Fig. 10: Typical moment-rotation relation of a segmental joint (Luttikholt, 2008) ... 11
Fig. 11: Moment-rotation relation resulting from touching of the outer edges of the segments (Luttikholt, 2008) ... 12
Fig. 12: K_A, K_R, K_{RO} stiffness in axial, radial and rotational directions of a joint (Do et al., 2013) ... 13
Fig. 13: Ring joint interaction restricting radial deformations (Winselmann et al., 2000) ... 14
Fig. 14: Longitudinal deformation modes (Cui et al., 2015) ... 15
Fig. 15: Pure bending (top), shear distortion (bottom) (Selke, 2013) ... 16
Fig. 16: Excavation-induced ground heave below roof slab in Block 18 ... 17
Fig. 17: Stagger-jointed assembly (left) and ring joint (right) of HWS ... 18
Fig. 18: Cross-section (left) and longitudinal joint (right) of HWS ... 18
Fig. 19: Soil profile (2D/“2.5D”) and results of triaxial compression test (*CD*) ... 19
Fig. 20: General model geometries used within preliminary study ... 20
Fig. 21: 2D finite element mesh (left), “2.5D” finite element mesh (right) ... 21
Fig. 22: 2D step simulation sequence (loading: upper path, unloading: lower path) ... 22
Fig. 23: 3D finite element mesh and model dimensions ... 22
Fig. 24: 3D step simulation sequence (unloading: upper path, loading: lower path) ... 23
Fig. 25: Definition of local system of axes for plate elements with respect to structural forces, strains and stiffness parameters (Brinkgreve et al., 2018b) ... 25
Fig. 26: Joint-induced stiffness reduction of diaphragm walls ... 26
Fig. 27: Basic idea of the joint-induced stiffness reduction ... 27
Fig. 28: Derivation procedure based on six steps to determine anisotropic parameters ... 28

Fig. 29: Simplified geometry - longitudinal joints (orange), ring joints (blue) and deduced cross-section 28
Fig. 30: Model transformation: indirect-joint model (left); direct-joint model (right) 30
Fig. 31: Axial orientation of shear forces, shear moduli and shear deformations 32
Fig. 32: Basic idea to account for the ring-joint-induced shear stiffness reduction 32
Fig. 33: Position of examined cross-sections 33
Fig. 34: Internal forces acting in the direction shown are considered as positive 34
Fig. 35: Bending moment diagram considering different longitudinal joint configurations (loading conditions) 36
Fig. 36: Shear force diagram considering different longitudinal joint configurations (loading conditions) 36
Fig. 37: Normal force diagram considering different longitudinal joint configurations (loading conditions) 36
Fig. 38: Bending moment diagram comparing different model types (unloading conditions) 38
Fig. 39: Shear force diagram comparing different model types (unloading conditions) 38
Fig. 40: Normal force diagram comparing different model types (unloading conditions) 38
Fig. 41: Model size recommendations (EANG, 2014) 39
Fig. 42: Relationship between the influence length of the ring joint L_f and the longitudinal bending rigidity ratio $\xi_{Cont.}$ 41
Fig. 43: Longitudinal distribution of vertical crown displacements (3D, loading) 42
Fig. 44: Longitudinal distribution of vertical crown displacements (3D, unloading) 42
Fig. 45: Model calibration based on the longitudinal distribution of vertical crown displacements (3D, loading) 44
Fig. 46: Model calibration based on the longitudinal distribution of vertical crown displacements (3D, unloading) 44
Fig. 47: Relationship between the longitudinal bending rigidity ratio in the ring joint area ξ_{Joint} and the max. bending moment M (3D, loading, middle cross section) 44
Fig. 48: Bending moment diagram (3D, loading) 45
Fig. 49: Shear force diagram (3D, loading) 46
Fig. 50: Normal force diagram (3D, loading) 46
Fig. 51: Effect of the shear stiffness reduction on the longitudinal distribution of vertical crown displacements (3D, loading) 48
Fig. 52: Effect of the shear stiffness reduction on the longitudinal distribution of vertical crown displacements (3D, unloading) 48

Fig. 53: Relationship between shear stiffness coefficient ζ_{Joint} and max. bending moment M_{max} 49
Fig. 54: Relationship between shear stiffness coefficient ζ_{Joint} and ovalization δ_H 49
Fig. 55: 3D model illustrating the newly-built cut-and-cover construction and the existing subjacent HWS drainage tunnel 54
Fig. 56: General project overview (left); Plan view of Block 18 and HWS (right) 55
Fig. 57: Cross section of Block 18 56
Fig. 58: Plan view of Block 18 covering structural elements and on-site photos.. 56
Fig. 59: Plan view of reinforced invert and corresponding on-site photo 56
Fig. 60: Soil profile as well as respective core sample 57
Fig. 61: FE mesh and geometric model 58
Fig. 62: Extract of the respective geotechnical report concerning conducted soil tests 59
Fig. 63: Influence of plasticity index on stiffness reduction (Vucetic and Dobry, 1991) 60
Fig. 64: Overview of entire 3D model and photo of the considered multi-storey building 61
Fig. 65: FE model taking into account the surface load of the adjacent building 62
Fig. 66: Specifications regarding the HWS geometry 62
Fig. 67: On-site photos replicating the construction process of Block 20 63
Fig. 68: FE model considering the construction of Block 20 63
Fig. 69: FE model considering the construction of Block 18 (top-view) 64
Fig. 70: FE model considering the construction of Block 18 (bottom-view) 64
Fig. 71: Calibration process performed in order to determine the load reduction factor 65
Fig. 72: Preparation of the working plane 65
Fig. 73: Calculation phase sequence 66
Fig. 74: Results are evaluated in the defined sections 68
Fig. 75: Vertical crown displacement curve of the tunnel lining obtained with different model depths z_{Model} 69
Fig. 76: Distribution of Small Strain Stiffness ratio as a function of model depth (vertical cross-sections) 70
Fig. 77: Distribution of Small Strain Stiffness ratio as a function of model depth (horizontal cross-sections 1 m above bottom model boundary) 70
Fig. 78: Vertical crown displacement curve of the tunnel lining obtained with different load reduction factors β 71
Fig. 79: The final excavation step is subdivided in six phases (Part A) 71
Fig. 80: The final excavation step is subdivided in six phases (Part B) 72
Fig. 81: Contours of vertical displacements u_z (left: sequential excavation; right: all-in-once excavation) 73

Fig. 82: Vertical crown displacement curve of the tunnel lining obtained with different calculation phase sequences during excavation step 3 73
Fig. 83: Development of vertical crown displacements at different cross-sections 74
Fig. 84: Development of cross-sectional bending moment at different positions of the lining (Cross-section B-B) 75
Fig. 85: Location and magnitude of max. lining displacement 75
Fig. 86: The results are obtained considering the marked viewing direction.. 76
Fig. 87: Vertical crown displacement curve obtained with different material properties of the tunnel lining 77
Fig. 88: Crown deflection angle δ obtained with different material properties of the tunnel lining 78
Fig. 89: Contours of vertical displacements u_z (overall behaviour) 79
Fig. 90: Vertical displacements u_z at different stages in Block 18 (cross-section B-B) 79
Fig. 91: Vertical crown phase displacements (Phase 12) obtained with different material properties of the tunnel lining 80
Fig. 92: Contours of vertical phase displacements Pu_z (hydraulic pressure)... 80
Fig. 93: Structural analysis of selected piles 81
Fig. 94: Stress-strain relationship at different stress states (reinforced concrete beam) (Nguyen, 2018) 81
Fig. 95: Theoretical model of tunnel lining (Murakanu and Koizumi, 1978) . 88
Fig. 96: Definition of cross-sectional parameters (Murakanu and Koizumi, 1978) 89
Fig. 97: Bending moment diagram considering different longitudinal joint configurations (unloading conditions) 90
Fig. 98: Shear force diagram considering different longitudinal joint configurations (unloading conditions) 90
Fig. 99: Normal force diagram considering different longitudinal joint configurations (unloading conditions) 90

List of symbols and abbreviations

Small letters

c'	[kPa]	Effective cohesion
m	[-]	Parameter which controls the amount of stress dependency
p_{ref}	[kPa]	Reference pressure for stress dependent stiffness
u_z	[m]	Vertical displacement (3D)
w_b	[m]	Bending-induced displacement
w_s	[m]	Shear-induced displacement
z_{Model}	[m]	Model depth

Capital letters

A	[m^2]	Cross-sectional area
D	[-]	Analysis performed under drained conditions
E	[GPa]	Young’s modulus
$E_{50,ref}$	[kPa]	Reference secant stiffness modulus in a drained triaxial test
$E_{oed,ref}$	[kPa]	Reference oedometric stiffness
$E_{ur,ref}$	[kPa]	Reference Young’s modulus for unloading and reloading
G	[GPa]	Shear modulus
G_0	[GPa]	Initial shear modulus at very small strains
I	[m^2]	Second moment of area
K_0	[-]	Coefficient of lateral earth pressure
K_A	[kN/m]	Axial joint stiffness
K_R	[kN/m]	Radial joint stiffness
K_{RO}	[kNm/°]	Rotational joint stiffness
L_f	[m]	Influence length of the ring joint (analytical solution)
L_{joint}	[m]	Length of the ring joint area (direct-joint model)
L_S	[m]	Segmental length (analytical solution)
$L_{segment}$	[m]	Length of the concrete segment (direct-joint model)
M	[kNm/m]	Bending moment
M_{max}	[kNm/m]	Max. cross-sectional bending moment

N	[kN/m]	Axial force
Pu_z	[m]	Vertical phase displacement
Q	[kN/m]	Shear force
R_{inter}	[-]	Interface reduction factor

Small Greek letters

α_s	[°]	Shear correction factor
β	[-]	Load reduction factor
γ	[kN/m^3]	Unit weight of soil
$\gamma_{0.7}$	[-]	Shear strain level where G_0 is reduced to 70%
γ_{sat}	[kN/m^3]	Unit weight of saturated soil
δ	[°]	Deflection angle at different positions along the tunnel crown
δ_H	[-]	Ovalization
ζ_{Joint}	[-]	Shear stiffness reduction ratio of the ring joint area
η	[-]	Transversal bending rigidity ratio
ν'	[-]	Poisson's ratio (MC)
ν'_{ur}	[-]	Poisson's ratio for unloading/reloading (HSS)
ξ (a)	[-]	Transfer ratio of bending moment
ξ (b)	[-]	Longitudinal bending rigidity ratio
ξ_{Joint}	[-]	Longitudinal bending rigidity ratio of the ring joint area (direct-joint model)
$\xi_{Cont.}$	[-]	Longitudinal bending rigidity ratio of the overall structure (indirect-joint model)
φ'	[°]	Effective friction angle
ψ	[°]	Dilatancy angle

Abbreviations

CD	[-]	Consolidated drained triaxial compression test
EA	[kN]	Normal stiffness
EI	[kNm^2]	Bending rigidity
FEA	[-]	Finite element analysis
GA	[kN]	Shear stiffness

GHS	[-]	Generalized Hardening Soil model
HSS	[-]	Hardening Soil Small model
ldb	[-]	Defined position of pile wall axis
MC	[-]	Mohr-Coulomb model (linear elastic - perfectly plastic model)
rdb	[-]	Defined position of pile wall axis

1 Introduction

1.1 Background

As part of the large-scale project “Stuttgart 21”, the construction of building lot “VE S-Bahn Los 4 Süd” (herein also referred to as “Wolframstraße”) was successfully completed in the first half of 2019. The aim of this project was to establish the underground railway passage to the newly-built central station “Kopfbahnhof” in Stuttgart coming from northeast. In this context, the cut-and-cover construction of Block 18 was executed in the vicinity of the existing drainage tunnel HWS which substantially contributed to the drainage of the urban area in Stuttgart. As a consequence, the construction program had to be developed such that the serviceability of the drainage tunnel was ensured at any time during construction. To this end, extensive 2D *FEA* were performed during the design phase to define appropriate constructional measures in order to restrict the tunnel heave induced by excavations above the tunnel axis. However, certain issues required full three-dimensional modelling. To this end, this thesis extends the existing design considerations and mainly focuses on 3D finite element analyses.

1.2 Scope and outline of this thesis

Chapter 2 starts with a brief literature survey providing basic knowledge regarding the constitution and the design of segmental tunnel linings; moreover, this section points out relevant modelling aspects. Next, geometric specifications of the actual HWS structure as well as its spatial boundary conditions are described. Chapter 2 then discusses the basic idea of a joint-induced stiffness reduction due to the presence of segmental joints from several perspectives. As core of this chapter, a parameter derivation procedure is established which allows to account for the effect of segmental joints on the overall behaviour of the tunnel lining. Based on the results of the conducted preliminary study, recommendations are given with respect to appropriate modelling of the HWS which are consequently applied to the 3D *FEA* of the construction lot “Wolframstraße”.

Based on the findings of the preliminary study presented in chapter 2, 3D analyses are performed in chapter 3 mainly concerning the structural response of the HWS lining to the construction of building lot “Wolframstraße”. To this end, the entire construction process in the vicinity of Block 18 was modelled by means of a 3D model consisting of around 1.150.000 10-noded elements (quadratic shape function). In the results section, the development of both, structural forces and displacements of the lining during construction are explained in detail. In addition, the deformation behaviour as a consequence of extensive rainfalls as well as structural forces obtained from the retaining structure are discussed. Chapter 3 closes by highlighting aspects that should be subject of further research.

2 Complex tunnel lining assembly: Preliminary study

As the lining of a shield-driven tunnel is not a continuous ring structure due to the presence of joints, the effect of the joints on displacements and structural forces should be considered in the design of segmental tunnel linings. This holds particularly true for complex lining assemblies such as the existing drainage tunnel HWS whereas the latter contributes to the drainage of the urban area of Stuttgart. In the present chapter, the latter serves as object of investigation whereas a number of modelling aspects are examined; for example, the effect of the joint rotational stiffness K_{RO} on the structural lining forces or the consideration of joint slipping by means of a joint-induced shear stiffness reduction are discussed. The presented results mainly aim to establish an appropriate modelling approach for the HWS.

The preliminary study presented in this chapter is structured as follows:

- Section 2.1 provides a brief introduction into the basics of segmental linings such as lining components and common failure mechanisms. In addition, the last part of this section gives a basic idea on advanced modelling aspects of segmental linings compared to the widely used isotropic continuous ring approach.
- Section 2.2 reflects on the spatial boundary conditions of the lining structure as well as on the geometric properties of the HWS. Moreover, the basic idea of reducing the stiffness components of the structure in order to account for the presence of joints is described in detail. This section further recaps the framework of the numerical studies as well as the established parameter derivation procedure which is consequently applied in the preliminary study.
- Section 2.3 summarizes the results of the performed analyses. Firstly, the effect of joints on the cross-sectional behaviour of the lining structure is analysed. Secondly, the derived findings are used to examine the effect of joints on the longitudinal structural behaviour. Finally, the ring joints are explicitly modelled in order study the effect of a joint-induced shear stiffness reduction on the structural behaviour of the lining.
- Section 2.4 aggregates the key findings of the preliminary study and presents the final modelling recommendations of the HWS.

Consequently, the recommendations given in this chapter are further applied to the large-scale model presented in chapter 3 of this thesis whereas the latter mainly aims to analyse the structural response of the existing HWS to the construction of building lot “Wolframstraße”.

2.1 Literature research

A literature research was performed to obtain the required data and state-of-the-art for the approached subjects. Section 2.1.1 provides relevant information regarding precast segmental tunnel linings such as lining components and their functions. Next, selected failure mechanism types are discussed to gain a general understanding of aspects which have to be considered in the design of segmental tunnel linings. Reflecting on both, analytical and numerical calculation models, the literature survey is concluded.

2.1.1 General introduction to segmental tunnel linings

In the latter half of the 20th century, mechanical tunnel driving has made remarkable progress; a brief overview of tunnel methods and their applicability is given in ÖBV (2009). Accordingly, the shield driven tunnelling method is nowadays widely adopted for the construction of urban underground tunnels in soft soils and, in many cases, provides several advantages such as flexibility, cost effectiveness and a minimum impact on ground traffic and surface structures compared to the conventional tunnelling method (Lee et al., 2001).

In general, shield driven tunnel linings are segmented and represent an assembly of prefabricated reinforced concrete segments as shown in Fig. 1. A general differentiation can be made between linings with flat joints (straight-jointed assembly) and linings with joint offsets (stagger-jointed assembly) (German Tunnelling Committee, 2013). The latter is broadly used as it improves the overall stiffness and the waterproofness (Guan et al., 2015).

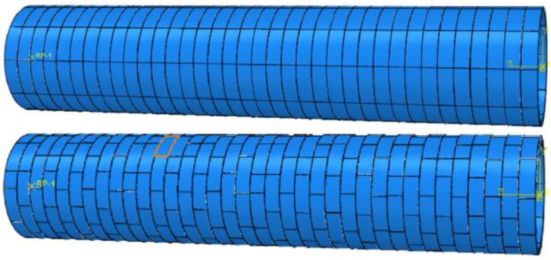

Fig. 1: Straight-jointed assembly (top); stagger-jointed assembly (bottom) (Yu et al., 2019)

Each ring consists of a set concrete segments which in turn interact via segment-to-segment interfaces (also referred to as “longitudinal joints”). The interaction between the concrete segments of different rings is again established via ring-to-ring-interfaces (also referred to as “circumferential” or “ring joint”) and illustrated in Fig. 2. Subsequently, the following paragraph reflects on the main parts of the lining and highlights important related issues.

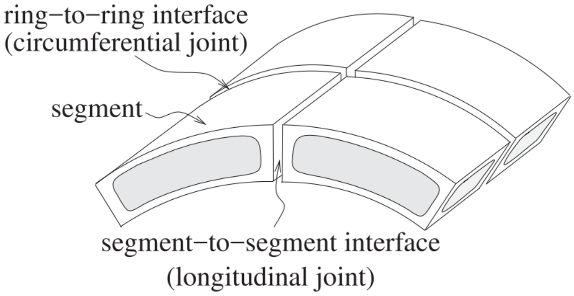

Fig. 2: Definition of lining components (Zhang et al., 2019)

- **Concrete segments**

Pre-fabricated reinforced concrete elements pose the core of the lining structure; the segmental ring then gains its bearing capacity primarily through the bedding in the surrounding rock. In this context, the general statement can be made that both the maximal bending moment and normal force depend on the relative stiffness of surrounded soil and lining structure (Erdmann and Duddeck, 1983).

Based on static specifications and constructional requirements (such as durability or quality of waterproofness), the segments usually have a thickness of 15-75 cm and, depending on the ring diameter, a height of 75-250 cm. German Tunnelling Committee (2013) provides the reader further information about requirements regarding tolerances and types of concrete segments, Möller (2006) describes the lining assembly process, respectively.

Noteworthy, the design of reinforcement tubing segments is mostly governed by bending moments and tensile splitting forces occurring throughout their lifetime; critical forces acting on the prefabricated concrete segments may occur even before the segments are put in their final positioning and exerted to earth, swelling or water pressure (Luttikholt, 2008). Substantial tensile splitting forces caused by jack forces of the TBM during tunnel advancement (see Fig. 3) or flexural tension stresses caused by dead loads during warehousing serve herein as good examples.

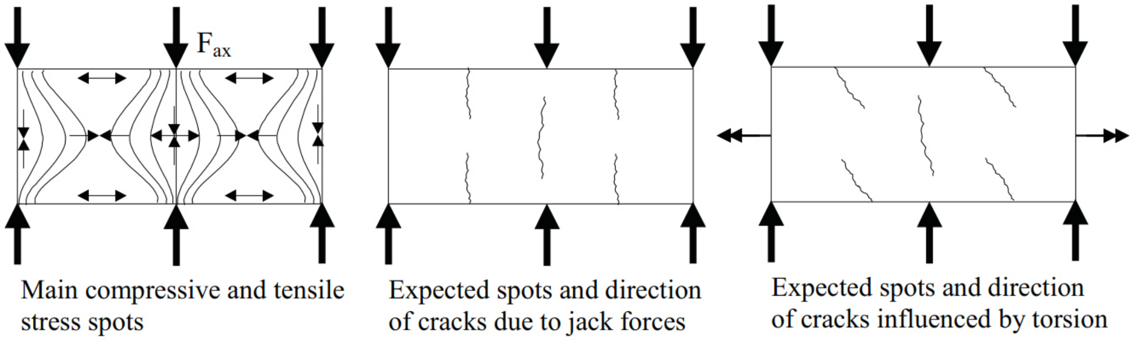

Main compressive and tensile stress spots

Expected spots and direction of cracks due to jack forces

Expected spots and direction of cracks influenced by torsion

Fig. 3: Split tensile stresses caused by jack forces (Blom, 2002)

Furthermore, the interaction of concrete segments needs to be considered. A case in point is, provided that a strong interaction between the segmental rings exists, that bending moments are transferred between them since the longitudinal joint cannot sustain the same bending moment as the segment body itself does.

Hence, bending moments imposed on the longitudinal joint are partly transferred to the segments of adjacent rings through the shearing mechanism of ring joints as shown in Fig. 4. Guan et al. (2015) suggested to apply the transfer ratio of bending moment ξ to account for these additional bending moments acting on concrete segments. At this point, it has to be noted that segmental linings bear the bending moments in the longitudinal joint by eccentric normal force transfer whereas hardly any tension forces occur (i.e. this is in particular the case if no bolts are installed) (Zhang et al., 2019).

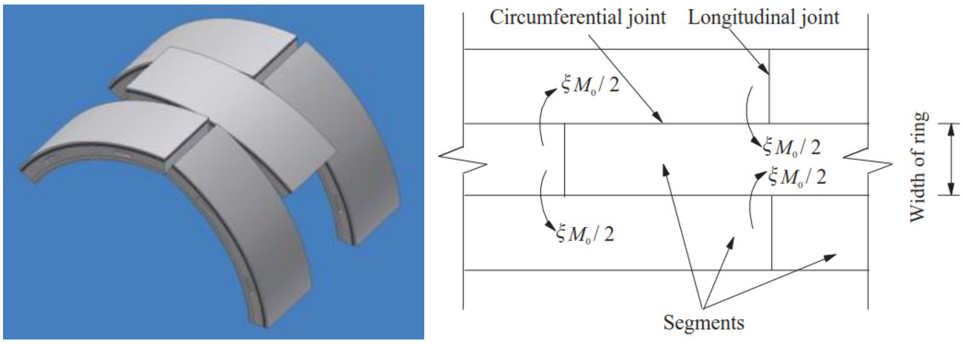

Fig. 4: Bending moment transfer between adjacent rings (Guan et al., 2015)

Both previously described peculiarities emphasize the complexity of the task to design concrete segments for mechanized tunnelling applications. An in-depth description of different loading states is presented in Zhang et al. (2019) as well as in German Tunnelling Committee (2013).

- **Longitudinal joints**

The contact surface between adjacent segments within a single ring is denoted as longitudinal joint. Regarding the constructional shape, a differentiation is made between three geometric types, namely: flat joint (a), double-convex joint, concave-convex joint (b) and tongue-groove joint (c) as shown in Fig. 5. For the interested reader, Osgoui et al. (2016) provides a critical comparison between double-convex and flat longitudinal joints.

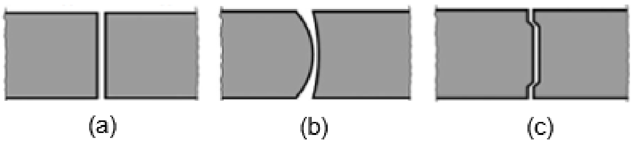

Fig. 5: Longitudinal joint types (FSV, 2013)

Ring interface forces induced by external and internal loads are mainly transferred via longitudinal joints. Further, the longitudinal joint has to sustain stress concentrations caused by pre-tension forces from the sealing elements. Hence, a good understanding of the joint behaviour results in a more realistic analytical and numerical modelling. The theoretical and experimental behaviour of longitudinal joints is well documented in Luttikholt (2008); a brief introduction is given in under section 2.1.3.

- **Ring Joints**

The contact surface between concrete segments of different rings is referred to as circumferential or ring joint as defined in Fig. 2. In practice, the following joint geometries are deployed: flat joint, tongue-groove joint and flat joint including additional centering or coupling elements such as dowels, centering cones or cam and pocket systems (German Tunnelling Committee, 2013). The latter, in particular, allows for transferring coupling forces between rings as described in Fig. 4. According to Winselmann et al. (2000), this increases the ring load bearing capacity and reduces lining deformations as illustrated in Fig. 13.

Considerable longitudinal forces resulting from the jack forces of the TBM are transferred via longitudinal joints; see Fig. 3. Hence, in many cases, additional reinforcement covering tensile split forces needs to be mounted. Further information on the theoretical behaviour of ring joints is given in Luttikholt (2008).

2.1.2 Design considerations for segmental tunnel linings

In general, the lining can fail due to both, failure of the tunnel lining itself or as a consequence of failure of the soil behind the lining (Luttikholt, 2008). To prevent failure, several design requirements and quality standards have to be considered. This includes also preventive measures to eliminate the risk of brittle edges or corner spalling in case of unplanned marginal pressures occurring during transport or installation. To demonstrate the importance of reliable designing methods, two design considerations are briefly discussed: additional internal forces occurring as a result of flattening of a jointed tunnel lining as well as excessive joint opening leading to water leakage. Further information on tunnel lining related damage mechanisms are found in Blom (2002).

- **Consequences of tunnel flattening with respect to internal forces**

Depending on the loading conditions, a segmental tunnel lining tends to flatten in a certain direction as shown in Fig. 6. Due to the compression of the soil at the sides of the tunnel, a lateral stress increase will be observed that effects horizontal and vertical stresses in the soil. As a result, bending moments in the tunnel lining change. Consequently, hoop forces can increase; hence, the likelihood of compressive failure may become crucial.

However, excessive flattening deformations result in additional bending moments due to geometric effects (Blom, 2002). Especially for soft soil conditions, large deformation effects eliminate the bending moment reducing effect of the activated ground resistance. In this case, second order bending moments govern the lining design as they increase until the ultimate bearing capacity is reached (Bakker, 2000).

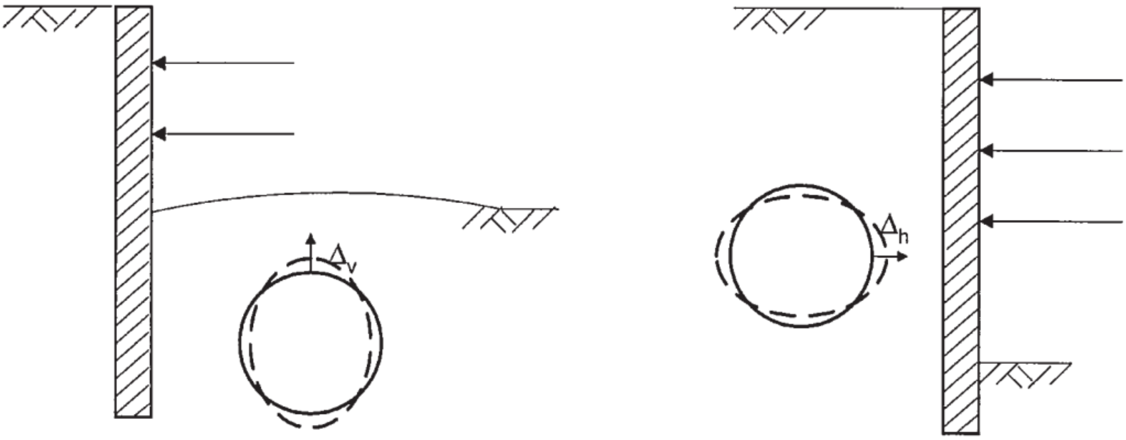

Fig. 6: Flattening-related tunnel deformations (Lee and Ge, 2001)

Furthermore, longitudinal differential settlements of shield-driven tunnels contribute to cross-sectional ovalization. Longitudinal settlements themselves are determined by the tunnel diameter, lining thickness and bending curvature. Huang et al. (2012) therefore developed analytical solutions to estimate additional forces and deformations derived from longitudinal differential settlements. In this study, the aforementioned effect becomes apparent if the longitudinal bending radius falls below a threshold value. Consequently, plane strain conditions should only be applied when differential settlements in the longitudinal direction are negligible in order to avoid unsafe design.

- **Water leakage due to joint birdsmouthing**

Lining structures service lives of 100 years or more. Further, repair options are limited and expensive regarding the seals of drainage tunnels. Hence, high importance has to be attached to tightness against water under pressure (German Tunnelling Committee, 2013).

Joint opening (i.e. resulting in water leakage) is induced by loading effects, imperfections or construction errors (Caratelli et al., 2018). From a static point of view, joint opening occurs if the bending stresses cannot be compensated by the normal force and considerable tensile stresses arise (Luttikholt, 2008). This is due to the fact that the tensile strength of lining structures within the area of joints is negligible and, thus, often ignored.

To this date, serviceability limit states for segmented tunnel linings regarding a required level of waterproofness are not accessible and mainly rely on the assessment of differential settlements or critical bending curvatures. In a first approximation, Gong et al. (2019) proposed a conceptual model to interpret the sealant behaviour of gasketed joints subjected to later water pressure. Thereby, a differentiation between four failure scenarios is made, namely: joint opening (a), joint offset (b), positive (c) and negative joint rotation (d); they are illustrated in Fig. 7.

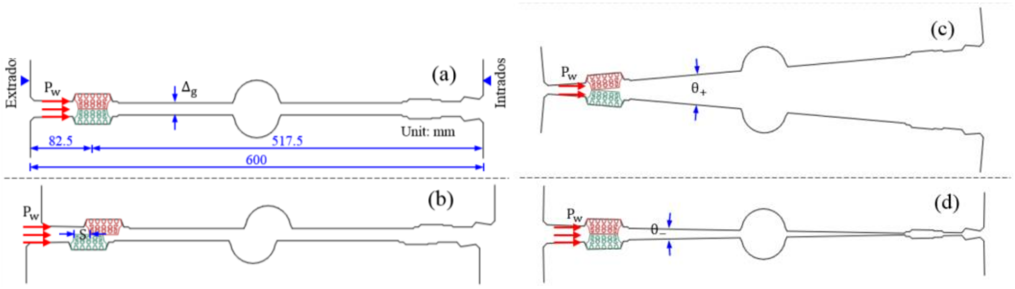

Fig. 7: Typical failure modes of joint waterproofing (Gong et al., 2019)

However, the interaction between system stiffness, water pressure, external force, joint rotation and gap opening is rarely reported in the literature. The same applies for the effect of external displacements and load boundary conditions. Hence, further research should concentrate on the investigation of sealant failure mechanisms in order to determine a required level of waterproofness reasonably.

2.1.3 Advanced design of segmental tunnel linings

In general, geotechnical structures, such as concrete retaining walls or pile walls, consist of continuous vertical elements. These panels are discontinuous in the horizontal directions due to the presence of constructional joints; thus, Zdravkovic et al. (2005) concluded that the axial and bending stiffness of any excavation supporting wall along its perimeter should be reduced (i.e. applying anisotropic material properties) to bring the discussion of deformations closer to practical realities. The latter is demonstrated in Fig. 8. Based on the aforementioned findings, Voit (2016) confirmed the general conclusions of Zdravkovic et al. (2005) and underlined the significant importance of the current drainage conditions for structures which are considered as anisotropic.

Shield tunnel linings are, in comparison, more complex because their structure is assembled by segments, joints, bolts and rubber gaskets. In addition to the previously described geotechnical structures related to excavations, shield tunnel linings are separated by joints in two directions. Longitudinal as well as circumferential joints have to be considered since they substantially govern the behaviour of a shield driven tunnel lining considerably (Teachavorasinskun and Chub-uppakarn, 2010).

The presence of joints affects the overall lining stiffness resulting in decreasing lining stresses; ignoring them leads to a very conservative design. On the contrary, overestimating the influence of joints and thereby reducing the stiffness of a tunnel structure extensively may result in larger deformations; thus, the level of waterproofness might be misinterpreted (Yu et al., 2019).

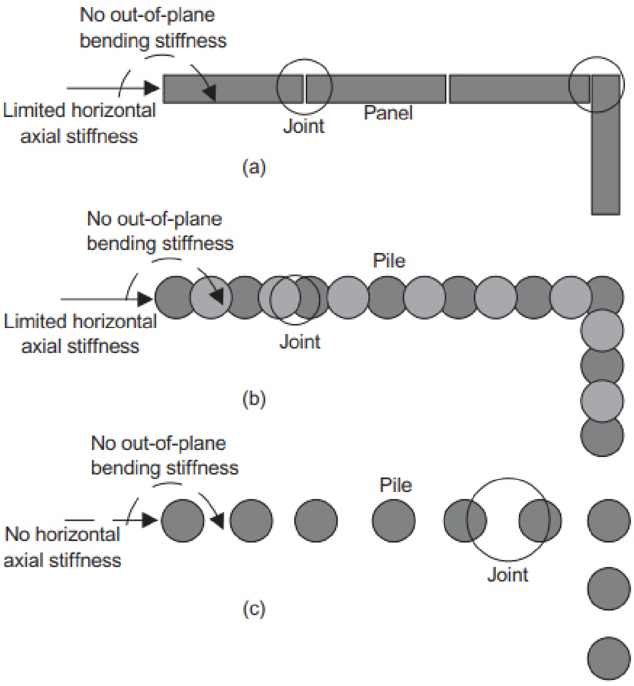
No out-of-plane bending stiffness
Limited horizontal axial stiffness
Joint
Panel
(a)
No out-of-plane bending stiffness
Pile
Limited horizontal axial stiffness
Joint
(b)
No out-of-plane bending stiffness
Pile
No horizontal axial stiffness
Joint
(c)

Fig. 8: Stiffness reduction of geotechnical structures due to the presence of construction joints (Zdravkovic et al., 2005)

The effect of joints on the behaviour of shield driven tunnel linings has been an object of research ever since. This section gives an overview of related issues and provides a general understanding, necessary for section 2.2.

- **Principal distinction between calculation models for tunnel linings**

Regarding the design of segmental tunnel linings, three categories exist: empirical methods, analytical solutions and numerical methods (Fu et al., 2016); an overview is given in Potts and Zdravković (2001).

The joint configuration (i.e. rotational stiffness, number and orientation of joints) governs the structural behaviour of segmental tunnel linings in the cross-sectional area (Do et al., 2013). Therefore, the joint-related behaviour of a segmental lining can either be approached as indirect-joint model or direct-joint model. Indirect-joint models consider lining structures as uniform rings with adjusted rigidities with respect to construction joints; on the contrary, construction joints are explicitly modelled in direct-joint models.

Furthermore, a distinction is made between two loading modes imposed by the surrounding soil, namely the active-loading mode and the passive-loading mode. For the active loading mode, the load acting on the lining is calculated by empirical or analytical formulas, for the passive loading mode, the load acting on the lining is calculated taking into account the soil-lining interaction by means of displacement compatibility (Guan et al., 2015).

To reduce calculation time and modelling effort, the structural behaviour of tunnel linings is commonly considered as two-dimensional problem both in the transverse and in the longitudinal direction, though it is a three-dimensional problem; in this context, Cui et al. (2015) gives an overview of modelling approaches in which the longitudinal deformation behaviour is considered as two-dimensional problem. Hence, it is best practice to regard segmental tunnel linings as three-dimensional structures since the longitudinal and the transverse stiffness are related to each other (Yu et al., 2019).

- **2D indirect-joint models (plane-strain conditions)**

Construction joints affect the overall rigidity of lining structures. To take this into consideration, Wood (1975) proposed to reduce the effective second moment of area of the overall lining I_L as follows:

$$I_L = \left[\frac{4}{N}\right]^2 \cdot I_0 + I_j < I_0 \tag{1}$$

where N is the number of concrete segments per ring ($N > 4$), I_0 is the second moment of area of concrete segments per unit length of a segmental tunnel and I_j the second moment of area at the longitudinal joints per unit length of a segmental tunnel. This approach accounts for an indirect proportional relationship between the number of longitudinal joints and the circumferential bending rigidity. Further, Wood (1975) concluded that the existence of longitudinal joints would not affect the rigidity of the lining if the number of segments is less or equal four.

Liu and Hou (1991) expanded this research and put forward an analytical solution to estimate the effective transversal bending rigidity ratio η:

$$\eta = \frac{(EI)_{jointed}}{(EI)_{continuous}} \leq 1 \tag{2}$$

where $(EI)_{jointed}$ is the effective flexural rigidity of the jointed ring structure and $(EI)_{continuous}$ is the flexural rigidity of the equivalent continuous ring structure. In addition to Wood (1975), the presented analytical solution takes the effects of joint stiffness and joint distribution into consideration.

However, these analytical solutions have its downside with respect to the in-depth analysis of internal forces and displacements as the bending rigidity is uniformly distributed; no regional distinction is made between concrete segment and joint area. Thus, complex joint characteristics such as joint stiffness, joint distribution and lining interaction with the surrounding soil are ignored. As a result, the application of indirect-joint models is restricted to the estimation of the maximum bending moment which is generally used for the preliminary design of a precast segmental tunnel lining (Teachavorasinskun and Chub-uppakarn, 2010).

- **2D direct-joint models (plane-strain conditions)**

Joints can also be directly integrated into the lining structure to account for the interaction of the adjoining concrete segments. In general, this is done via semi-rigid elastic elements inserted at the position of the longitudinal joints (Faltýnek and Pruška, 2019). In Teachavorasinskun and Chub-uppakarn (2010), for example, joints were simulated using a set of rotational springs to investigate the effect of the joint rotational stiffness K_{RO} on the effective transversal bending rigidity ratio η. The joint rotational stiffness value, K_{RO}, is defined as the bending moment-per-unit length required to develop a unit rotation angle along the joints of the assembled segments as shown in Fig. 9.

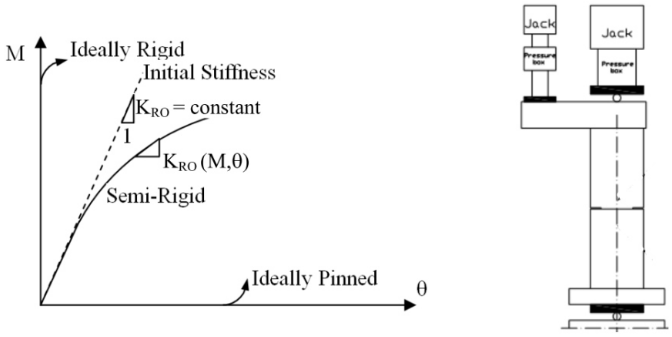

Fig. 9: Edge values of joint behaviour (left); experimental facility (right) (Faltýnek and Pruška, 2019)

Advanced moment-rotation relations such as presented by Janßen (1983) can be implemented in numerical models in order to bring the discussion closer to reality. Janßen (1983) distinguishes between a linear branch, where the rotational rigidity is only affected by the Young’s modulus of the concrete and the height of the joint (h) and a non-linear branch, where K_{RO} is additionally governed by the normal force (F_N) acting in the circumferential direction. The non-linear branch describes a less stiff behaviour as soon as the normal force acts outside the core of the contact area and, as a result, the contact stress becomes zero and a gap starts to form. The described behaviour is illustrated in Fig. 10. The moment capacity is reached for $M = 1/2 \cdot F_N \cdot h$ resulting in an ideally pinned joint behaviour (see Fig. 9).

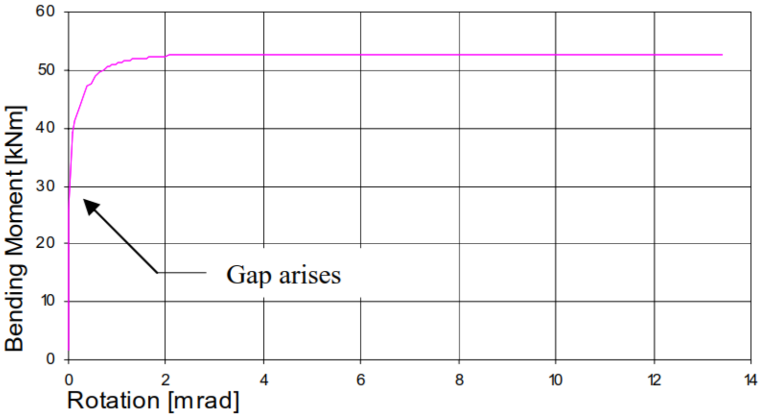

Fig. 10: Typical moment-rotation relation of a segmental joint (Luttikholt, 2008)

In case of very thin longitudinal joints present, the rotational behaviour may be governed by direct contact of the outer edges. Minor rotations increase as long as the outer edges stay separated. At that point the outer edges touch the moment-rotation relation is characterized by strengthening as illustrated in Fig. 11. As a result, the moment-rotation relation theory presented by Janßen (1983) is more applicable for describing thick joints.

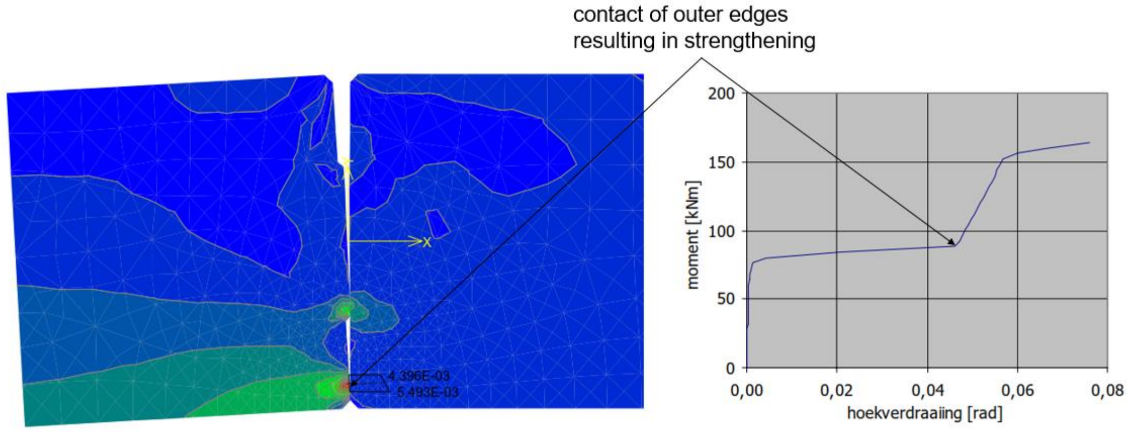

Fig. 11: Moment-rotation relation resulting from touching of the outer edges of the segments (Luttikholt, 2008)

However, the bending moment capacity of the longitudinal joint is not a constant. Apart from the applied load (i.e. normal force and bending moment), further aspects should be considered when determining the bending moment capacity such as a non-linear stress-strain-relation of concrete or a non-linear stress distribution in the joint (i.e. at the edges of the contact surface stresses reach infinity).

Blom (2002) expanded Janßen's theory accounting for a bilinear stress-strain behaviour allowing for plastic deformations. Further, he distinguished between two loading cases with the initial normal force being close to the concrete compressive strength or not. Based on numerical calculations, Faltýnek and Pruška (2019) presented an approach for practical numerical modelling with respect to Blom's theory.

In Lee et al. (2001), model tests showed that the joint rotational stiffness K_{RO} is higher when the joint is subjected to a positive bending moment than that when subjected to a negative bending moment (i.e. $K_{RO}^{-} = (1/2\text{-}1/3)\ K_{RO}^{+}$)[1]. In addition to the formulation of the rotational stiffness K_{RO}, Do et al. (2013) added axial (K_A) and radial (K_R) stiffness parameters to characterize the translational joint behaviour as pictured in Fig. 12. Accordingly, K_A and K_R are defined as the axial force and the shear force-per-unit-length required to develop a unit axial and radial displacement at a given joint. They concluded that both K_A and K_R have a negligible effect on segmental lining behaviour.

---

[1] The bending moment is defined as positive when the inner curve of the lining is subjected to tension.

Finite element modelling often restricts the application of advanced joint formulations. A case in point is that in Plaxis 2D, the settings allow for four options to simulate longitudinal joints, namely: fixed, rigid, elastic as well as elasto-plastic spring (Brinkgreve et al., 2019). If the latter option is selected, the maximum bending moment can be specified besides the rotational stiffness. However, in Plaxis 3D these connection options are further limited to fixed or free (Brinkgreve et al., 2018a). Thus, one should first check whether advanced joint formulations can be adopted or not. The previous disclosure, to some extent, demonstrates the complexity of ring joint models which is subject to ongoing research activities.

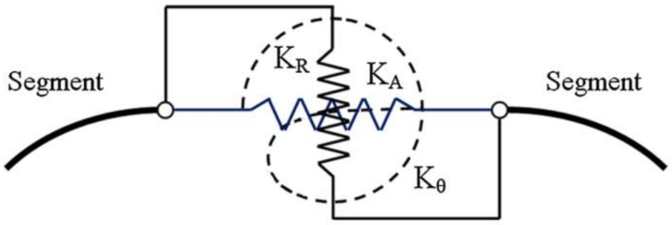

Fig. 12: K_A, K_R, K_{RO} stiffness in axial, radial and rotational directions of a joint (Do et al., 2013)

- **Soil-structure interaction**

To this point, the influence of the surrounding ground on the calculated results was not discussed. Teachavorasinskun and Chub-uppakarn (2010), for instance, quoted that a lining simulated in a stiffer soil yields lower maximum bending moments acting on it. Furthermore, Guan et al. (2015) verified that the effective transversal bending rigidity ratio η decreases with stiffer soil properties. This clearly shows that the soil-structure interaction, apart from joints, has a considerable effect on the structural response of a segmental tunnel lining.

In numerical analyses, the soil-structure interaction is either considered by applying discrete springs (i.e. tangentially and radially) or a full ground model using the finite element or finite difference method. The latter options enable the user to implement advanced interface elements, for example, taking into consideration the thin zone of intensely sheared material. Thus, Do et al. (2013) deduced that more accurate results regarding the structural response of lining structures are produced by this approach.

- **Longitudinal rigidity of segmental tunnel linings**

Generally, the design of a segmental tunnel lining is made under plane-strain conditions, ignoring its structural response in the longitudinal direction. However, the structural behaviour in the axial direction should be considered for the analysis of internal forces and the waterproof design of the structure Cui et al. (2015). In particular, this applies for jointed shield tunnels in soft soil layers since they are exposed to considerable longitudinal deformations.

Cui et al. (2015) provide a comprehensive list of calculation models taking the longitudinal response of shield tunnels into consideration. Similarly to calculation models describing the cross-sectional behaviour, a distinction is made between indirect and direct-joint models to account for a discounted rigidity due to the ring joint. For indirect-joint models, the concept of the effective longitudinal bending rigidity ratio ξ was put forward analogously:

$$\xi = \frac{(EI)_{jointed}}{(EI)_{continuous}} \leq 1 \tag{3}$$

where $(EI)_{jointed}$ is the effective flexural rigidity of the jointed ring structure and $(EI)_{continuous}$ is the flexural rigidity of the equivalent continuous ring structure. Different to the previously described effective transversal bending rigidity ratio η, the effective longitudinal bending rigidity ratio ξ addresses a discounted flexural rigidity in the longitudinal direction due to the presence of ring joints.

However, the effect of rings joints on the structural behaviour of tunnel linings can only be examined in detail if ring joints are modelled explicitly (herein referred to as direct-joint model). A case in point is the migration of bending moments between adjacent rings increasing the load bearing capacity of the overall lining (Luttikholt, 2008); unless ring joints are modelled explicitly, this results in a conservative design of tunnel linings. Furthermore, the consequences of shear forces counteracting radial and tangential deformations can only be considered if direct-joint models are used; see Fig. 13.

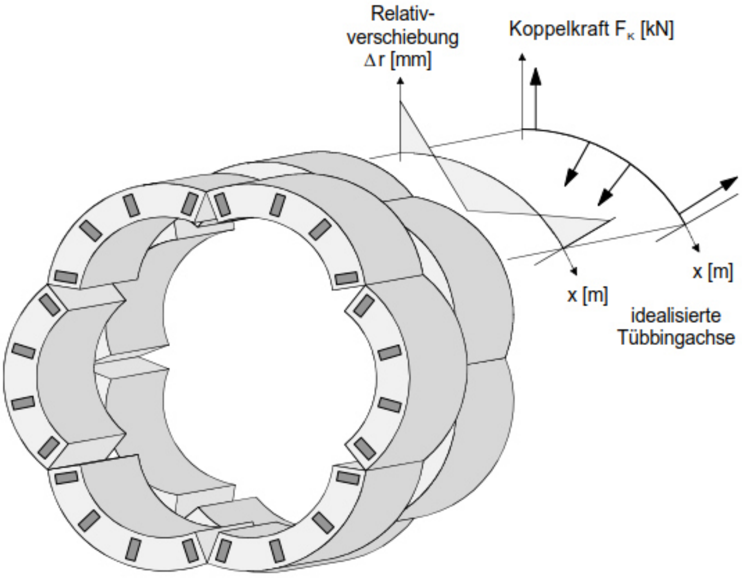

Fig. 13: Ring joint interaction restricting radial deformations (Winselmann et al., 2000)

Bao (2015) examined differences between straight-jointed and stagger-jointed lining assemblies in the light of longitudinal bending rigidity and ring joint opening; in straight-jointed lining assemblies, concrete segments are separated by flat joints whereas stagger-jointed lining assemblies are characterized by joint offsets as illustrated in Fig. 1. In this publication, it was revealed that only an insignificant difference between the straight and stagger-jointed tunnel assembly occurred with regards to longitudinal displacements. On the contrary, the influence of the assembly pattern on joint opening is evident Bao (2015). As shield driven tunnels are sensitive to failure due to excessive joint opening, the assembly pattern should be taken into consideration during the design.

Cui et al. (2015) highlight two general longitudinal deformation modes, namely: bending deformation mode and deformation mode of dislocation as illustrated in Fig. 14. The bending deformation mode describes flexural deformation under pure bending (following the Euler-Bernoulli beam theory), whereas the latter is characterized by differential dislocation of adjoining rings under shear force Cui et al. (2015).

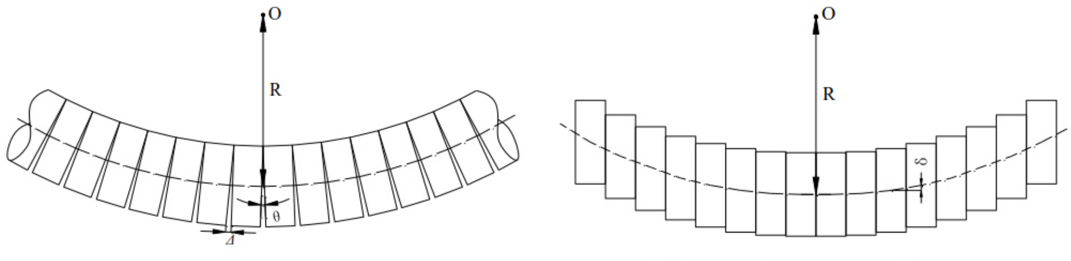

(a) bending deformation mode (b) deformation mode of dislocation

Fig. 14: Longitudinal deformation modes (Cui et al., 2015)

The Euler-Bernoulli beam theory omits shear distortion. Further, it is inter alia based on the assumption that cross-sections stay perpendicular to the beam axis throughout deformation. Strictly spoken, under the presence of considerable shear forces this assumption becomes invalid as shown in Fig. 15 (Selke, 2013). Accordingly, the total deformation comprises both shear induced deformation w_s and pure bending deformation w_b. The ratio for a simply supported beam on two supports subjected to a uniformly distributed load can be written as in Equ. (4).

$$\frac{w_s}{w_b} = \frac{9{,}6 \cdot E \cdot I}{G \cdot A \cdot \alpha_s \cdot l^2} \tag{4}$$

In Equ. (4), E is the Young’s modulus; I is the relevant second moment of area; G is the shear modulus; A is the cross section area; α_s is the correction factor accounting for different cross-sectional shapes; l is the beam length. Assuming that E, I, G, A and α_s are constant values, the shear induced deformation becomes more dominant with decreasing beam length. Given that this in general applies for tubular structures as well the following conclusion is drawn: The deformation mode of dislocation becomes more distinct with decreasing tunnel length.

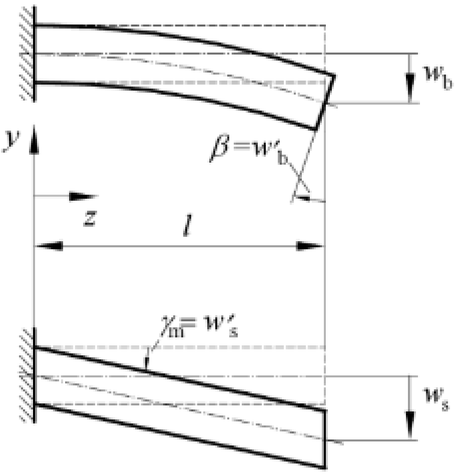

Fig. 15: Pure bending (top), shear distortion (bottom) (Selke, 2013)

Although Cui et al. (2015) reported that the deformation of a tunnel in staggered arrangement is dominated by the dislocation between rings, most theories are still based on the bending deformation mode ignoring the dislocation between rings. Moreover, the interaction between longitudinal and transverse behaviour is, in many cases, omitted. Thus, the last paragraph highlights particularities of segmental tunnel linings that occur if they are considered as three-dimensional problem.

- **Segmental tunnel lining considered as three-dimensional structure**

So far, the transverse and longitudinal behaviour of segmental tunnel linings have been approached as two-dimensional problems, though it is a three-dimensional one. Particularly, because the longitudinal and the transverse stiffness of a liner are related to each other (Yu et al., 2019). In accordance, Bao (2015) performed parametric studies which indicate that the longitudinal bending stiffness of the segmental liner increases with the transverse bending stiffness η of the tunnel cross-section.

Huang et al. (2012) proved that longitudinal differential settlements lead to additional tangential bending moments due to flattening; unless this is taken into consideration, the design might be unsafe. Liao et al. (2008) further investigated the longitudinal load transfer mechanism of tunnel linings by means of a cylindrical shell within an elastic foundation. Their calculations led to the conclusion that both the increase of circumferential and radial shear stiffness results in a decreasing bending moment in the cross-section of a tunnel lining. Hence, structural measures should be taken to strengthen the shear stiffness between rings in order to reduce the additional bending moment induced by ground displacement. The presented research clearly demonstrates the effects of 3D calculations on the relevant results. These effects are only insufficiently captured by 2D analyses. Thus, 3D analyses are highly recommended to assess the structural behaviour of segmental tunnel linings.

2.2 Modelling approach

The previous chapter provides a general introduction to segmental tunnel linings including basic lining components, design considerations and calculation approaches. Based on these considerations, this chapter presents an approach to determine the parameters necessary for modelling complex lining structures as indirect-joint model (i.e. circular plate elements with anisotropic material behaviour). Thereby, a semi-analytical derivation procedure is employed to model the existing drainage tunnel “Hauptsammler West” of building lot “VE S-Bahn Los 4 Süd” in Stuttgart. In the following, the reference structure is referred to as HWS. The presented numerical calculations are conducted using the FE software Plaxis 2D 2018.01 (Brinkgreve et al., 2019) and Plaxis 3D 2018.01 (Brinkgreve et al., 2018a). The input data including plans, soil profile and lining parameters are taken from the related technical report of construction lot “Wolframstraße” (Summerer and Hosp, 2018).

2.2.1 Problem definition

As part of the large-scale project “Stuttgart 21”, the construction lot “VE S-Bahn Los 4 Süd” (herein also referred to as “Wolframstraße”) establishes the underground railway link to the central station “Kopfbahnhof” coming from northeast. The project covers a total length of approximately 475 m and comprises 45 tunnel blocks. In this Master's Thesis, the construction process of Block 18 is examined in detail; see Fig. 16. The excavation activity below the roof slab is expected to have a considerable effect on the performance of the subjacent HWS due to spatial boundary conditions: When the excavation base is reached, the remaining overburden approaches a minimum value of less than 1 m, whereas ground heave is induced. In addition, the load case of hydraulic inner pressure resulting from excessive rainfalls has to be considered which, inter alia, increases the risk of water leakage due to birdsmouthing; see 2.1.2. Hence, FE analyses are performed to gain in-depth understanding of the HWS-related structural consequences resulting from the excavation activities.

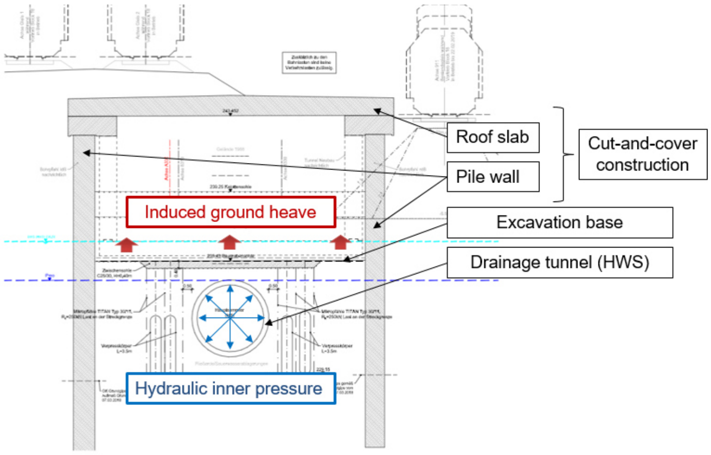

Fig. 16: Excavation-induced ground heave below roof slab in Block 18

- **HWS specifications**

The HWS serves as drainage tunnel transporting rainwater from the urban area in Stuttgart to the local river called Neckar. Since no reliable information about the current condition of the construction elements is available, these eventual effects are not subject of this study (for example, consequences due to altering). Key parameters used in the calculations are listed in Tab. 1.

Tab. 1: HWS-related parameters

parameter		value	unit
thickness	d	0.28	m
segment height	h	0.80	m
mean radius	R	2.0	m
conrete quality	-	C 35/45	-
Young's modulus	E	34	GPa
assembly type	-	honeycombed	-
Poisson's ratio	ν	0.2	-
unit weight	γ	25	kN/m^3

The HWS structure consists of sequentially aggregated rings with staggered ring joints. This lining configuration is also referred to as hexagonal ring or honeycomb ring (German Tunnelling Committee, 2013); see 2.1.1. Adjacent concrete segments are attached by steel anchors in the axial direction as shown in Fig. 17. In circumferential direction, adjacent concrete segments interact via steel-pin-fixed plates; see Fig. 18.

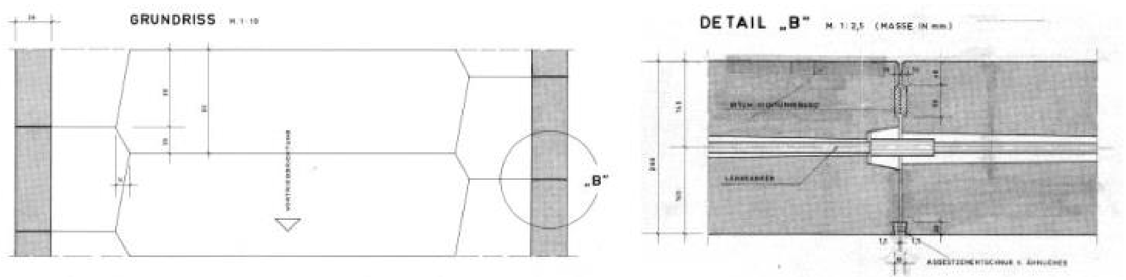
GRUNDRISS
„B“
DETAIL „B“
BITUM. DICHTUNGSBAND
LÄNGSANKER
ASBESTZEMENTSCHNUR u. ÄHNLICHES

Fig. 17: Stagger-jointed assembly (left) and ring joint (right) of HWS

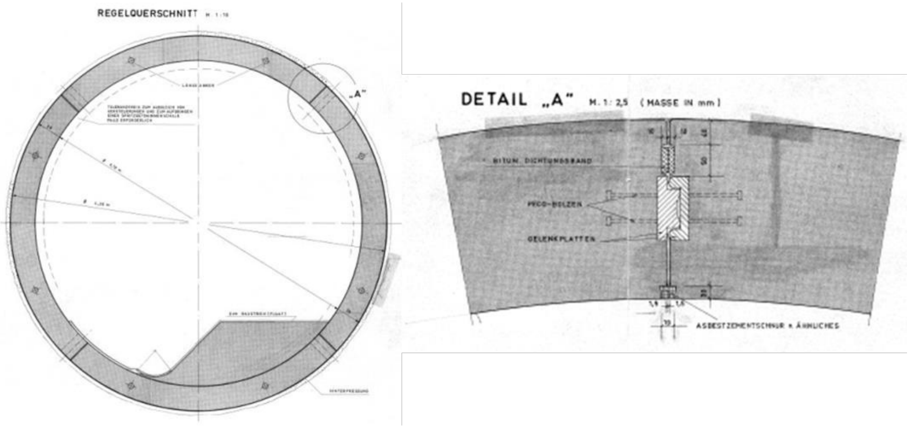
REGELQUERSCHNITT
„A“
DETAIL „A“
BITUM. DICHTUNGSBAND
PECO-BOLZEN
GELENKPLATTEN
ASBESTZEMENTSCHNUR u. ÄHNLICHES

Fig. 18: Cross-section (left) and longitudinal joint (right) of HWS

2.2.2 Soil conditions and constitutive models

Herein adopted soil parameters stem from both triaxial compression tests (*CD*) as well as pressiometer tests which were conducted on the construction site in 2018. They represent a typical soil profile in Stuttgart (Benz and Wehnert, 2015) composed of stiff sandy-clayey silt (herein referred to as “Fließerde”) and Keuper marl; see Fig. 19.

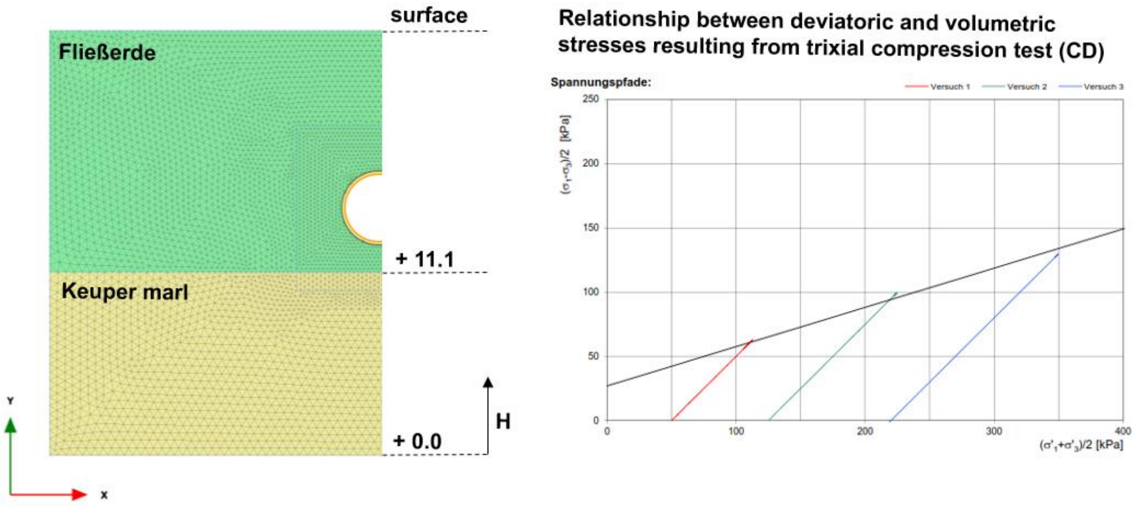

Fig. 19: Soil profile (2D/“2.5D”) and results of triaxial compression test (*CD*)

The non-linear elasto-plastic Hardening Soil Small model (*HSS*) was used to model all soil units (Benz, 2007). The *HSS* soil parameters of both soil layers are summarised in Tab. 2 and Tab. 3. The soil-structure-interaction was established via interface elements allowing for relative displacements between the soil and the lining (Tschuchnigg, 2013). The presented results refer to drained conditions with no groundwater table present.

Tab. 2: HWS preliminary study - soil parameters (part A)

Symbol	Fließerde	Keuper marl	Unit
Model	HSS	HSS	-
Type	D	D	-
γ	20	21	kN/m^3
γ_{sat}	20	21	kN/m^3
$E_{50,ref}$	8500	21000	kPa
$E_{ur,ref}$	8500	21000	kPa
$E_{oed,ref}$	17800	42000	kPa
φ'	25	25	°
ψ	0	0	°
c'	15	20	kPa

Tab. 3: HWS preliminary study - soil parameters (Part B)[2]

Symbol	Fließerde	Keuper marl	Unit
h (2D I 2.5D)	11.1 - surface	0 - 11.1	m
h (3D)	31.1 - surface	0 - 31.1	m
ν'_{ur}	0.2	0.2	-
p_{ref}	100	100	kPa
m	0.6	0.55	-
$\gamma_{0.7}$	0.00015	0.00015	-
G_0	21250	52500	kPa

2.2.3 Geometry and calculation phase sequence

In this study, both 2D- and 3D-*FEA* are performed in order to investigate the structural response of the HWS drainage tunnel subjected to loading and unloading conditions, respectively. A differentiation between three general model types is made, namely: 2D, “2.5D” and 3D. 2D analyses are conducted to examine the effect of longitudinal joints on the cross-sectional behaviour of the HWS. In the same way, “2.5D” analyses are performed by extending the 2D geometry by three metres in the third dimension as shown in Fig. 20. The latter serve as reference for comparison with 2D results as they allow to study differences derived from geometrically equivalent models. While shape functions of fourth order are used for the majority of the 2D calculations, quadratic shape functions are used for reasons of comparison between 2D and “2.5D”[3]. The 3D models are adopted to study 3D effects such as described in 2.1.3.

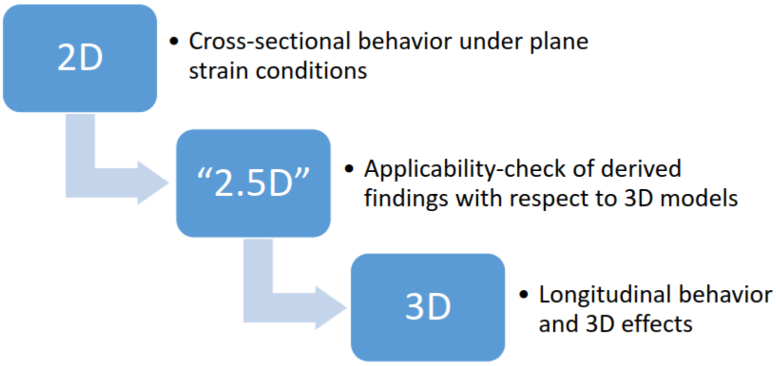
2D
• Cross-sectional behavior under plane strain conditions
“2.5D”
• Applicability-check of derived findings with respect to 3D models
3D
• Longitudinal behavior and 3D effects

Fig. 20: General model geometries used within preliminary study

---

[2] In *FEA*, if model dimensions are set too small, calculation results are affected by model boundaries and, thus, falsified. To eliminate this influence, reference analysis with varying model depth h and width are performed in 2D and 3D. As a result, the lower 3D model boundary is shifted by 20 m in the negative vertical direction compared to the 2D/2.5D model whereas the lining still remains embedded in the “Fließerde” soil layer. In this way, the effect of the model depth on the calculation results is reduced.

[3] While Plaxis 2D 2018.01 allows for two different element types (i.e. six-noded elements with quadratic shape function and 15-noded elements with shape function of fourth order), Plaxis 3D 2018.01 is restricted to 10-noded tetrahedral elements with quadratic shape function.

- **2D / "2.5D" model**

The mesh consists of approximately 20.000 15-noded elements in the 2D model and 100.000 10-noded elements in the "2.5D" model, respectively. As described in the previous paragraph, 6-noded elements with quadratic shape functions are applied in 2D as well for the purposes of comparison between 2D and "2.5D". The internal forces and displacements of the tunnel lining are the key results of this study; hence, the mesh discretization is locally refined on the circumferential of the tunnel. Further refinement of the mesh discretization resulted in no significant deviations with respect to the key results (e.g. crown displacement, distribution of internal forces); thus, the chosen mesh discretization is considered as sufficient. Fig. 21 documents that the model dimensions are consistent with the recommendations of EANG (2014). It is noted that the model depth is not constant and varies for loading and unloading conditions .

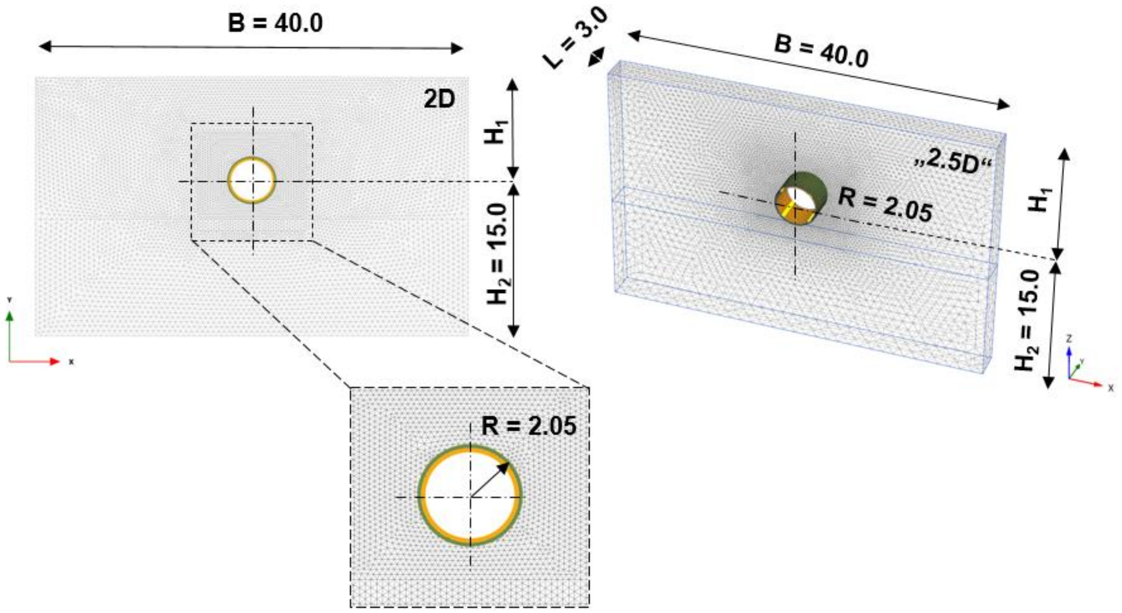

Fig. 21: 2D finite element mesh (left), "2.5D" finite element mesh (right)

To get a better understanding of the structural response to different loading conditions, four cases are examined, namely: Loading 1, Loading 2, Unloading 1, Unloading 2. They differ with respect to overburden (H_1), magnitude of surface load (q) and excavation height (ΔH), respectively. An overview is given in Tab. 4

Tab. 4: Specifications of calculation models (2D / "2.5D")

model	q	unit	H_1	unit	ΔH	unit
Loading 1	60	kN/m/m	10.75	m	-	-
Loading 2	300	kN/m/m	10.75	m	-	-
Unloading 1	-	-	10.75	m	8	m
Unloading 2	-	-	15.1	m	11	m

The 2D and "2.5D" calculations are divided into four phases; see Fig. 22. The initial phase (K_0-procedure) is followed by the load reduction step (β-procedure)[4] in which the tunnel is excavated. Subsequently, both plate and interface elements are activated in the third phase. The last step differs: for loading, the line load q is activated; for unloading, soil volumes are deactivated down to a depth of ΔH.

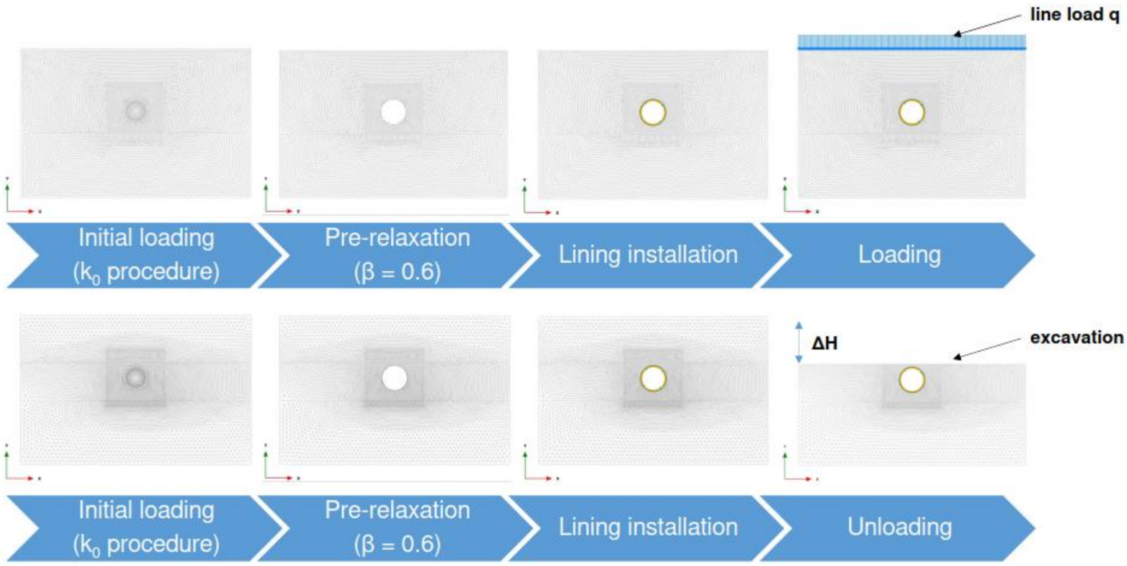
line load q
Initial loading
(k_0 procedure)
Pre-relaxation
(β = 0.6)
Lining installation
Loading
ΔH
excavation
Initial loading
(k_0 procedure)
Pre-relaxation
(β = 0.6)
Lining installation
Unloading

Fig. 22: 2D step simulation sequence (loading: upper path, unloading: lower path)

- **3D model**

For 3D models, the mesh is discretized with approximately 100.000 10-noded elements (quadratic shape function) and further refined on the circumferential of the tunnel. The mesh quality is verified by reference calculations with increased mesh density; further refining the mesh resulted in minor deviations with respect to key results (e.g. crown displacement, distribution of internal forces). Fig. 23 gives the model dimensions.

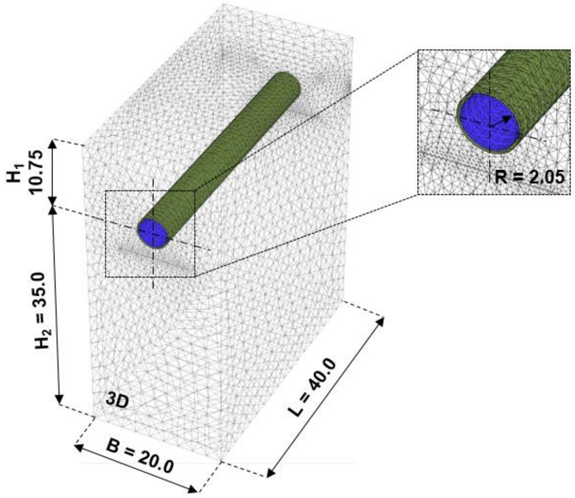
H_1
10.75
H_2 = 35.0
3D
B = 20.0
L = 40.0
R = 2,05

Fig. 23: 3D finite element mesh and model dimensions

---

[4] Wohlfahrt (2010) provided guidance regarding the estimation of the load reduction factor β under equivalent spatial and underground conditions, respectively.

The 3D calculation phase sequence takes loading as well as unloading conditions into considerations: The initial phase (K_0-procedure) is proceeded by the load reduction step (β-procedure) in which the tunnel is excavated; in the third phase, both plate and interface elements are activated. In case of loading, a surface load is applied in the final phase. On the contrary, unloading conditions are generated via deactivating a surcharge load as shown in Fig. 24.

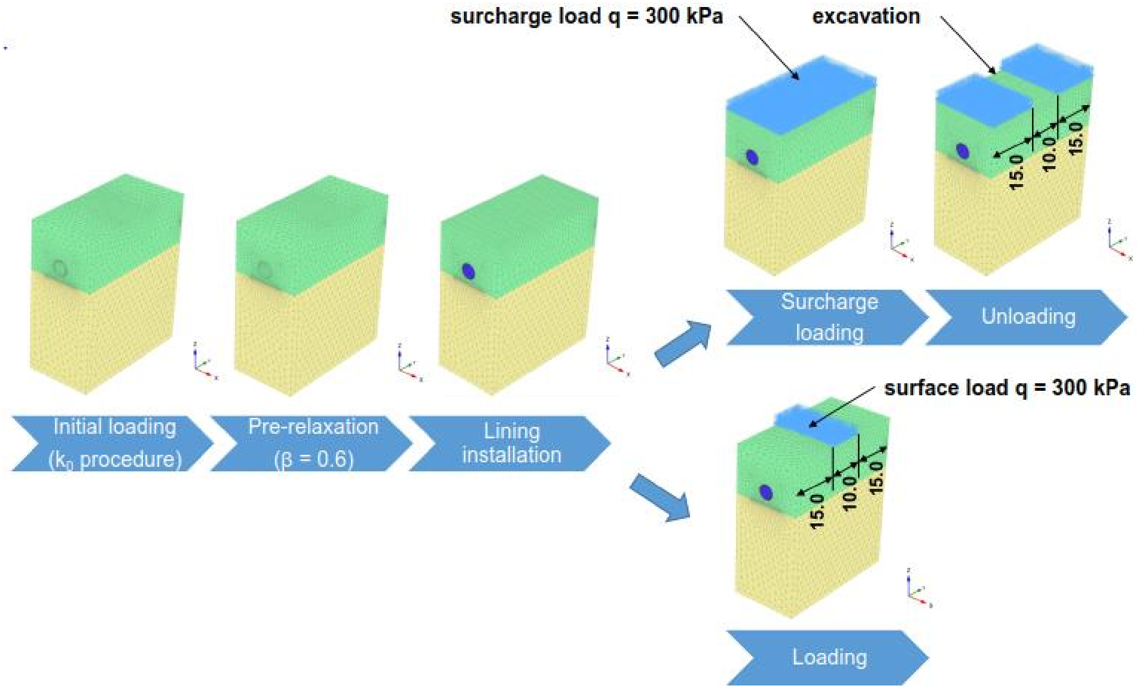
surcharge load q = 300 kPa
excavation
15.0
10.0
15.0
Surcharge loading
Unloading
surface load q = 300 kPa
15.0
10.0
15.0
Initial loading (k0 procedure)
Pre-relaxation (β = 0.6)
Lining installation
Loading

Fig. 24: 3D step simulation sequence (unloading: upper path, loading: lower path)

2.2.4 HWS model

In common 3D *FEA*, tunnel linings are modelled as isotropic circular plate element. In this way, segmental joints are ignored although they determine the structural behaviour of concrete linings significantly. A more realistic approach results when the segmental linings are modelled as anisotropic material (i.e. indirect-joint model); see Zdravkovic et al. (2005). Therefore, the following independent parameters have to be defined (Brinkgreve et al., 2018b):

E_1:	kN/m^2	Young's modulus in first axial direction
E_2:	kN/m^2	Young's modulus in second axial direction
G_{12}:	kN/m^2	In-plane shear modulus
G_{13}:	kN/m^2	Out-of-plane shear modulus (shear deformation over 1st direction)
G_{23}:	kN/m^2	Out-of-plane shear modulus (shear deformation over 2nd direction)
ν_{12}:	-	Poisson's ratio ($\nu_{12} < \sqrt{E_1/E_2}$)

With respect to orthotropic plate elements, the material behaviour is defined by the stress-strain relationship represented in Equation (5):

$$\begin{bmatrix} \sigma_{11} \\ \sigma_{22} \\ \sigma_{12} \\ \sigma_{13} \\ \sigma_{23} \end{bmatrix} = \begin{bmatrix} E_1 & \nu_{12}E_2 & 0 & 0 & 0 \\ \nu_{12}E_2 & E_2 & 0 & 0 & 0 \\ 0 & 0 & G_{12} & 0 & 0 \\ 0 & 0 & 0 & kG_{13} & 0 \\ 0 & 0 & 0 & 0 & kG_{23} \end{bmatrix} \begin{bmatrix} \varepsilon_{11} \\ \varepsilon_{22} \\ \gamma_{12} \\ \gamma_{13} \\ \gamma_{23} \end{bmatrix} \tag{5}$$

Ignoring higher order terms in *ν* and assuming the Poisson's ratio as small, the relationship between structural forces and induced strains can be written as in Equations (6-8):

$$\begin{bmatrix} N_1 \\ N_2 \end{bmatrix} = \begin{bmatrix} E_1 d & \nu_{12}E_2 d \\ \nu_{12}E_2 d & E_2 d \end{bmatrix} \begin{bmatrix} \varepsilon_1 \\ \varepsilon_2 \end{bmatrix} \tag{6}$$

$$\begin{bmatrix} Q_{12} \\ Q_{13} \\ Q_{23} \end{bmatrix} = \begin{bmatrix} G_{12}d & 0 & 0 \\ 0 & kG_{13}d & 0 \\ 0 & 0 & kG_{23}d \end{bmatrix} \begin{bmatrix} \gamma_{12} \\ \gamma_{13}^{*} \\ \gamma_{23}^{*} \end{bmatrix} \tag{7}$$

$$\begin{bmatrix} M_{11} \\ M_{22} \\ M_{12} \end{bmatrix} = \begin{bmatrix} \frac{E_1 d^3}{12} & \frac{\nu_{12}E_2 d^3}{12} & 0 \\ \frac{\nu_{12}E_2 d^3}{12} & \frac{E_2 d^3}{12} & 0 \\ 0 & 0 & \frac{G_{12}d^3}{12} \end{bmatrix} \begin{bmatrix} \kappa_{11} \\ \kappa_{22} \\ \kappa_{12} \end{bmatrix} \tag{8}$$

The indices used in Equations (5-8) correspond to the definitions proposed by Brinkgreve et al. (2018a) in Fig. 25; herein used abbreviations are defined as:

N:	kN/m	Normal force
Q:	kN/m	Shear force
M:	kNm/m	Bending moment
k:	-	Shear correction factor (= 5/6 for plate elements)
d:	m	Thickness of plate element
ε:	-	Normal strain
γ:	-	Shear strain
κ:	-	Bending curvature

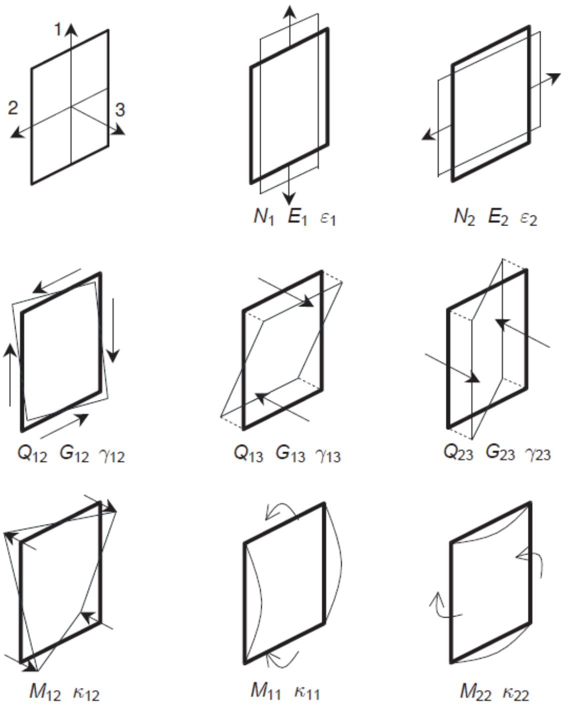
1
2
3
N_1 E_1 ε_1
N_2 E_2 ε_2
Q_{12} G_{12} γ_{12}
Q_{13} G_{13} γ_{13}
Q_{23} G_{23} γ_{23}
M_{12} κ_{12}
M_{11} κ_{11}
M_{22} κ_{22}

Fig. 25: Definition of local system of axes for plate elements with respect to structural forces, strains and stiffness parameters (Brinkgreve et al., 2018b)

- **Reference model**

Diaphragm walls represent a series of concrete sections separated by vertical construction joints. Considering the presence of vertical joints, Zdravkovic et al. (2005) quoted that the resistance against bending in horizontal direction as well as the normal stiffness in horizontal direction are overestimated when diaphragm walls are considered as isotropic. To bring this discussion closer to reality, Voit (2016) approached diaphragm walls as indirect-joint model by using plate elements with anisotropic material behaviour. In this way, the effect of vertical construction joints on the deformation behaviour of diaphragm walls was accounted for; see Fig. 26. In the reference, the following stiffness parameters were reduced to 25 % of the equivalent isotropic ones:

- E_2 affecting the deformation behaviour in ② and ⑤
- G_{12} affecting the deformation behaviour in ④ and ⑥
- G_{23} affecting the deformation behaviour in ③

Vertical construction joints have a minor effect on both, the bending curvature about the horizontal axis (κ_{11}) as well as the strain in the vertical direction (ε_1); see Fig. 25. However, if E_2 is reduced in order to account for the presence of vertical construction joints, κ_{11} and ε_1 are affected as well; see Equations (9-10). This contradiction almost disappears for small values of the Poisson's ratio *v*; thus, this is ignored as it will not be possible to match all anisotropic stiffness parameters exactly for a given plate thickness d (Brinkgreve et al., 2018b).

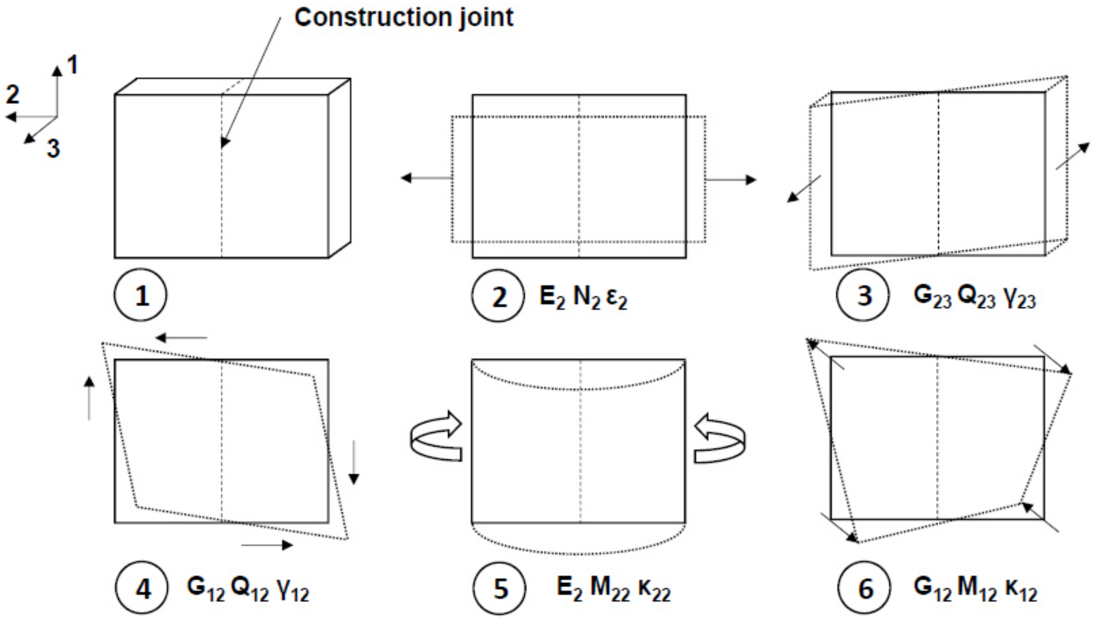

Fig. 26: Joint-induced stiffness reduction of diaphragm walls

$$\epsilon_{11} = \frac{N_2 - \frac{N_1}{\nu_{12}}}{d \cdot \left(\nu_{12} \cdot E_2 - \frac{E_1}{\nu_{12}}\right)} \tag{9}$$

$$\kappa_{11} = \frac{12 \cdot \left(M_{22} - \frac{M_{11}}{\nu_{12}}\right)}{d^3 \cdot \left(\nu_{12} \cdot E_2 - \frac{E_1}{\nu_{12}}\right)} \tag{10}$$

- **Joint-induced stiffness reduction in indirect-joint models**

Segmental lining structures are composed of concrete segments that are separated by longitudinal joints and ring joints; see 2.1.1. In practice, the corresponding stiffness parameters are reduced in order to account for segmental joints in indirect-joint models which is also referred to as joint-induced stiffness reduction; see Fig. 27.

In particular, the bending resistance *EI* is affected by the presence of joints (Voit, 2016). In addition, segmental joints have an impact on the normal stiffness *EA* and the shear stiffness *G*A, respectively. The assumption of lowering the normal stiffness is based on the idea that joints are closing with an increasing compression force such as those occurring in tunnel linings. The reduced normal stiffness represents an equivalent stiffness to consider the total deformations, which result from the compression of the concrete segment itself as well as the joint closure. The reduced shear stiffness accounts for the deformation mode of dislocation; see Fig. 14. The total deformations result from the shearing deformation of the concrete segments as well as the shear-induced offset at the joints. To account for slipping of the segmental joints, the shear stiffness parameters of the overall lining are, thus, modified.

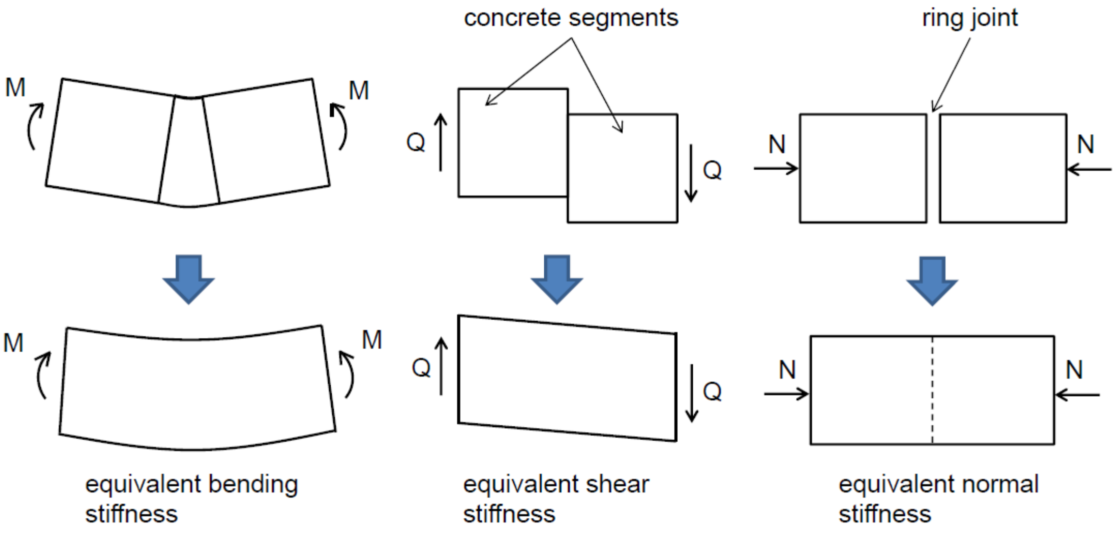
concrete segments
ring joint
M
M
Q
Q
N
N
M
M
Q
Q
N
N
equivalent bending stiffness
equivalent shear stiffness
equivalent normal stiffness

Fig. 27: Basic idea of the joint-induced stiffness reduction

- **Implementation of joint-induced stiffness reduction**

For a given plate thickness d, the effective material cross section areas for both, shear forces and normal forces, represent constants; the same applies for the moment of inertia against bending. Thus, the geometric properties cannot be modified in order to reduce *EI*, *EA* and *GA*, respectively. Hence, implementing the joint-induced stiffness reduction is restricted to lowering the anisotropic stiffness parameters E_1, E_2, G_{12}, G_{13} and G_{23}. In other words, geometric anisotropy is approached as material anisotropy. In this context, Brinkgreve et al. (2018b), Zdravkovic et al. (2005) as well as Voit (2016) provide recommendations with respect to the modelling of T-shaped floor profiles, sheet-pile walls and retaining walls, respectively.

The present study extends the basic idea of the joint-induced stiffness reduction to the modelling of segmental tunnel linings. To this end, the following questions are addressed with respect to the HWS:

- How do longitudinal joints affect the cross-sectional behaviour?
- How can ring joints be accounted for with respect to the longitudinal deformation behaviour?
- Which consequences has the joint-induced shear stiffness reduction on both, the max. cross-section bending moment M_{max} and the ovalization δ_H?

Consequently, six steps are established to answer these questions; see Fig. 28. Having in this way gained in-depth knowledge about the effect of segmental joints on the HWS structure, recommendations are given in chapter 2.4 with respect to the determination of its anisotropic stiffness parameters (i.e. E_1, E_2, G_{12}, G_{13}, G_{23} and ν_{12}).

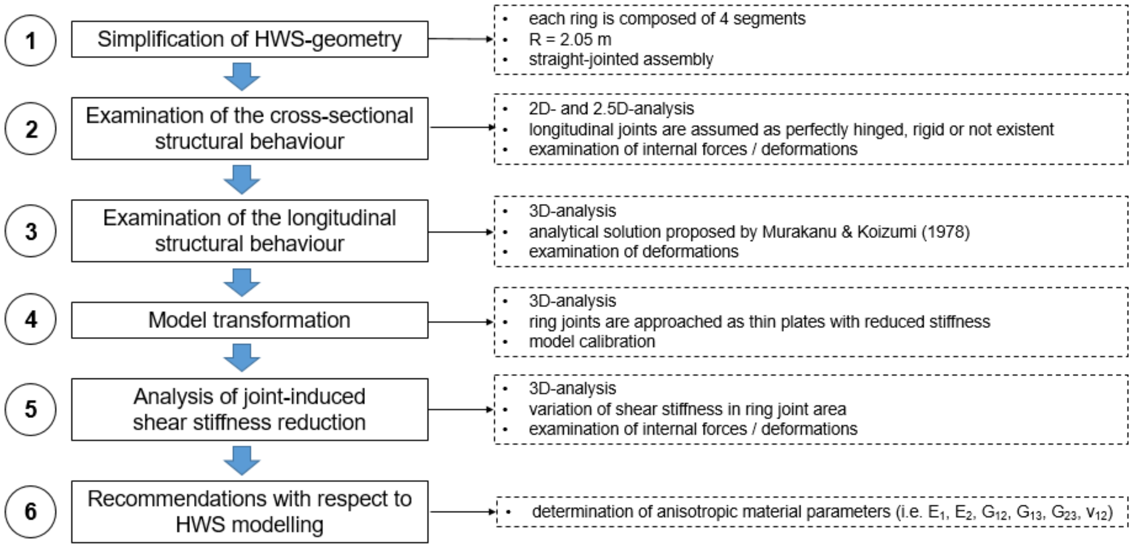
1
Simplification of HWS-geometry
each ring is composed of 4 segments
R = 2.05 m
straight-jointed assembly
2
Examination of the cross-sectional structural behaviour
2D- and 2.5D-analysis
longitudinal joints are assumed as perfectly hinged, rigid or not existent
examination of internal forces / deformations
3
Examination of the longitudinal structural behaviour
3D-analysis
analytical solution proposed by Murakanu & Koizumi (1978)
examination of deformations
4
Model transformation
3D-analysis
ring joints are approached as thin plates with reduced stiffness
model calibration
5
Analysis of joint-induced shear stiffness reduction
3D-analysis
variation of shear stiffness in ring joint area
examination of internal forces / deformations
6
Recommendations with respect to HWS modelling
determination of anisotropic material parameters (i.e. E_1, E_2, G_{12}, G_{13}, G_{23}, ν_{12})

Fig. 28: Derivation procedure based on six steps to determine anisotropic parameters

- **Explanation of parameter derivation procedure**

Step 1: The HWS drainage tunnel represents a stagger-jointed ring assembly formed by hexagonal concrete segments with no plane of symmetry present; see 2.2.1. In this study, the present tunnel geometry is simplified as illustrated in Fig. 29. Since the longitudinal joints proceed continuously and almost parallel to the longitudinal axis, these joints are simplified as flat joints parallel to the tunnel axis. Similarly, ring joints are approximated as flat joints perpendicular to the tunnel axis. In other words, the present stagger-jointed lining assembly is considered as straight-jointed lining assembly. With respect to the longitudinal deformation behaviour of a four-fold segmented tunnel lining, the eligibility of this simplification approach is strengthened by Bao (2015) and Wood (1975); see 2.1.3.

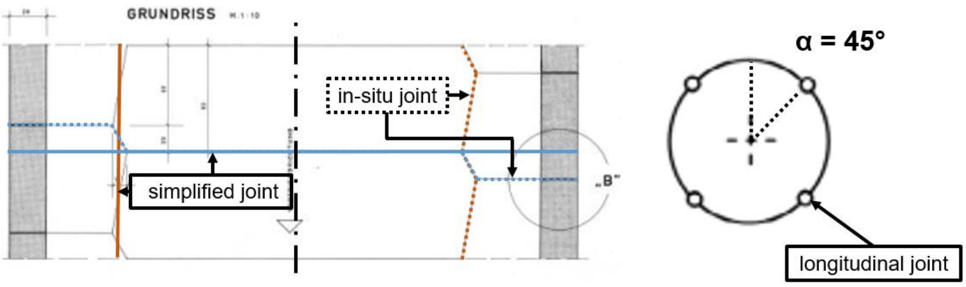
GRUNDRISS
in-situ joint
simplified joint
„B"
α = 45°
longitudinal joint

Fig. 29: Simplified geometry - longitudinal joints (orange), ring joints (blue) and deduced cross-section

Step 2: Based on the simplified cross-section illustrated in Fig. 29, 2D as well as "2.5D" calculations are conducted whereas a differentiation is made between loading and unloading conditions; see 2.2.3. With regard to longitudinal-joint-modelling, the in-situ rotational rigidity K_{RO} lies somewhere between the edge values considered for ideally rigid and ideally hinged joints; see 2.1.3. Hence, a boundary value analysis is conducted in which the rotation degrees of freedom (i.e. representing longitudinal joints) are modelled as rigid and fully hinged, respectively. In an additional analysis, the HWS is modelled as uniform ring as well. However, the translational degree of freedom remain fixed in all calculations.

In this way, deviations resulting from different longitudinal joint modelling approaches are analysed with respect to lining deformations and internal forces. The derived findings are then used to determine the effective transversal bending rigidity ratio η of the HWS structure; see 2.1.3.

Step 3: In this step, the HWS is modelled as continuous circular 3D plate element with anisotropic material. Thereby, the model accounts for longitudinal joints and ring joints, respectively. Considering longitudinal joints, the effective transversal bending rigidity ratio η, which is deduced from step 2, is used to modify both the normal stiffness ($E_2 \cdot A_2$) and the bending stiffness ($E_2 \cdot I_2$) in circumferential direction:

$$E_2\, I_2 = E_{HWS} \cdot \eta \cdot \frac{d^3 \cdot 1m}{12} \qquad (11)$$

$$E_2\, A_2 = E_{HWS} \cdot \eta \cdot d \cdot 1m \qquad (12)$$

where I_2 is the moment of inertia against bending over the longitudinal axis, A_2 is the effective material area for axial forces in the circumferential direction, E_2 is the effective Young's modulus in the circumferential direction (i.e. Plaxis input value) and E_{HWS} is the Young's modulus of the HWS concrete segments; see Tab. 1.

Regarding the presence of ring joints, both the normal stiffness ($E_1 \cdot A_1$) and the bending stiffness ($E_1 \cdot I_1$) in the longitudinal direction are modified. Therefore, the analytical solution presented by Murakanu and Koizumi (1978) is used to quantify the longitudinal bending rigidity ratio $\xi_{Cont.}$; a brief description is given in Appendix A:

$$E_1\, I_1 = E_{HWS} \cdot \xi_{Cont.} \cdot \frac{d^3 \cdot 1m}{12} \qquad (13)$$

$$E_1\, A_1 = E_{HWS} \cdot \xi_{Cont.} \cdot d \cdot 1m \qquad (14)$$

In the Equations (13-14), I_1 is the moment of inertia against bending over the circumferential axis, A_1 is the effective material area for axial forces in the longitudinal direction, E_1 is the effective Young's modulus in the longitudinal direction (i.e. Plaxis input value) and E_{HWS} is the Young's modulus of the HWS concrete segments; see Tab. 1.

Step 4: The previous steps focus on the joint-induced reduction of both, the normal stiffness as well as the bending stiffness. However, segmental joints also affect the shear stiffness (*GA*); see Fig. 27. In this context, Liao et al. (2008) investigated the effect of the joint-induced shear stiffness reduction on the structural behaviour of tubular structures; see 2.1.3. Avgerinos and Potts (2017) adopted the basic idea of the joint-induced shear stiffness reduction on the 3D modelling of tunnel linings whereas the derivation of the herein introduced shear correction factor k was not further explained.

As previously discussed in 2.1.3, indirect-joint models have shortcomings regarding the investigation of complex joint characteristics such as the joint-induced shear stiffness reduction. To overcome this limitation, the indirect-joint model of step 3 is transformed to the direct-joint model as illustrated in Fig. 30. Thereby, two simplifications are made:

- Longitudinal joints have a minor effect on the rigidity of the lining if the number of segments is less or equal four; see 2.1.3. Hence, the segmental lining is approached as a series of uniform isotropic rings ($L_{segment} = 0.52$ m) separated by ring joints ($L_{joint} = 0.28$ m). While L_{joint} corresponds to the HWS lining thickness d, $L_{segment}$ equals the HWS concrete segment height (h = 0.80 m) minus the HWS lining thickness d; the latter geometric approximation was proposed by Janßen (1983). Nevertheless, in this way, the longitudinal joints are ignored.
- Ring joints are modelled as thin plate sections. In this way, both a reduced longitudinal bending stiffness $(E_1 \cdot I_1)_{Joint}$ and a reduced normal stiffness $(E_1 \cdot A_1)_{Joint}$ of the ring joint area compared to the adjoining isotropic rings is accounted for. In contrast to the indirect-joint model, in which both stiffness components are uniformly reduced along the entire tunnel length, the direct-joint model restricts the influence sphere of the ring-joint-induced stiffness reduction to the ring joint area. Thus, the structural consequences of the ring-joint-induced shear stiffness reduction can be studied in more detail.

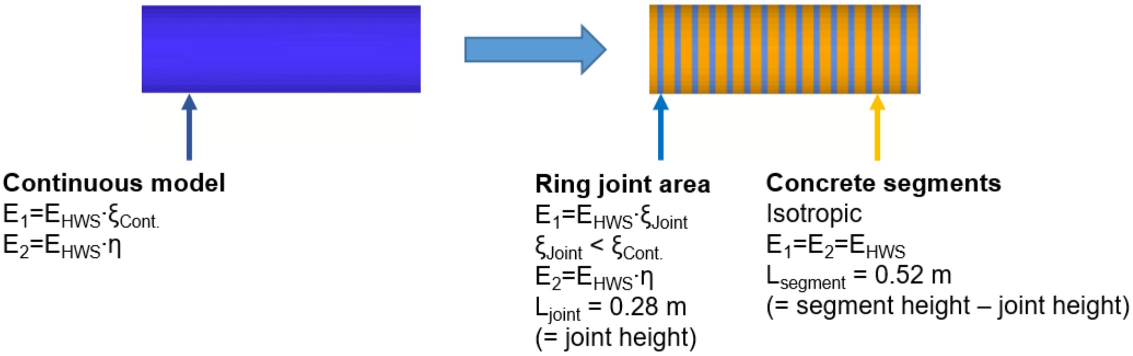
Continuous model
$E_1 = E_{HWS} \cdot \xi_{Cont.}$
$E_2 = E_{HWS} \cdot \eta$
Ring joint area
$E_1 = E_{HWS} \cdot \xi_{Joint}$
$\xi_{Joint} < \xi_{Cont.}$
$E_2 = E_{HWS} \cdot \eta$
$L_{joint} = 0.28$ m
(= joint height)
Concrete segments
Isotropic
$E_1 = E_2 = E_{HWS}$
$L_{segment} = 0.52$ m
(= segment height – joint height)

Fig. 30: Model transformation: indirect-joint model (left); direct-joint model (right)

To provide consistency between both models, comparative 3D calculations are conducted in which the vertical deformations occurring at the crown u_z are chosen as matching parameter. Consequently, the longitudinal bending rigidity ratio of the ring joint area ξ_{Joint} is selected such that the vertical deformations at the crown show good agreement amongst both models.

In contrast to Plaxis 2D 2018.01, ring joint modelling is restricted to the options “fixed” and “free” with respect to the translational and rotational degrees of freedom in Plaxis 3D 2018.01. This limitation precludes the aforementioned iterative calibration process of the direct-joint model. To get around this restriction, the presented workaround (i.e. ring joint modelled as thin plate section) is applied in this analysis.

Step 5: Based on the calibrated direct-joint model, step 5 aims to get a better understanding of the consequences the joint-induced shear stiffness reduction has; in particular, its effects on the HWS concrete segments are investigated. The basic idea of the joint-induced shear stiffness reduction is as follows:

The total shear deformations of the HWS are regarded as the sum of the shearing of the concrete segments themselves and the shear-induced offsets at the joints. In the present case, joint offsets are restricted to the ring joints since the HWS is modelled as a series of uniform rings as explained in step 4. As a result, joint offsets are induced by Q_{12} and Q_{13}, whereas radial offsets at the longitudinal joints induced by Q_{23} are ignored. For the reader’s understanding, Fig. 31 provides a schematic view of the axial orientation of corresponding shear forces, shear moduli and shear deformations.

In order to account for the shear-induced offsets at the ring joints, the additional translational movements at the ring joints are approximated as additional shear deformation of the thin plates representing the ring joints; see Fig. 32. Correspondingly, $(G_{12} \cdot A_{12})_{Joint}$ and $(G_{13} \cdot A_{13})_{Joint}$ are reduced by employing a parameter called shear stiffness reduction ratio ζ_{Joint}:

$$\zeta_{Joint} = \frac{(GA)_{Joint}}{(GA)_{HWS}} \leq 1 \tag{15}$$

where $(GA)_{Joint}$ is the effective shear stiffness of the ring joint area in the direction of the respective axes and $(GA)_{HWS}$ is the shear stiffness of the HWS concrete segments.

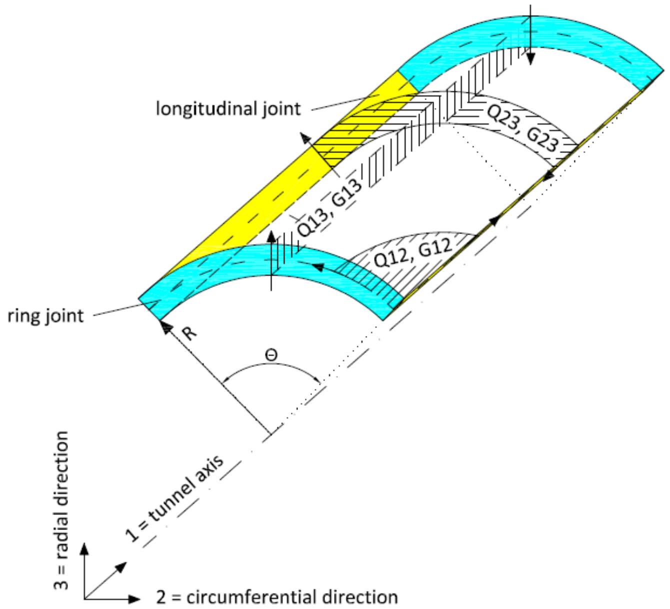
longitudinal joint
Q23, G23
Q13, G13
Q12, G12
ring joint
R
Θ
1 = tunnel axis
3 = radial direction
2 = circumferential direction

Fig. 31: Axial orientation of shear forces, shear moduli and shear deformations

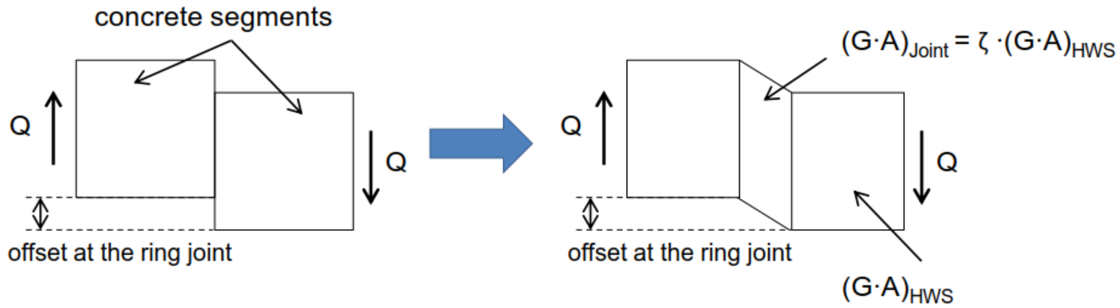
concrete segments
Q
Q
offset at the ring joint
(G·A)Joint = ζ ·(G·A)HWS
Q
Q
offset at the ring joint
(G·A)HWS

Fig. 32: Basic idea to account for the ring-joint-induced shear stiffness reduction

The effective material cross section area for both, the shear force $Q_{12,Joint}$, $A_{12,Joint}$, as well as for the shear force $Q_{13,Joint}$, $A_{13,Joint}$, represent constants for a given plate thickness d. Hence, we account for slipping at the ring joints by reducing the corresponding shear moduli $G_{12,Joint}$ and $G_{13,Joint}$ as follows:

$$G_{12,Joint} = G_{HWS} \cdot \zeta_{Joint} \tag{16}$$
$$G_{13,Joint} = G_{HWS} \cdot \zeta_{Joint} \tag{17}$$

To analyse the effect of the ring-joint-induced shear stiffness reduction on the HWS concrete segments, six sets of coefficients ($\zeta_{Joint} = 0.01, 0.05, 0.1, 0.3, 0.5, 1.0$) are adopted in this analysis. The following quantities are then evaluated:

- Longitudinal vertical displacement at the tunnel crown u_z
- Max. cross-sectional bending moment M_{max}
- Ovalization δ_H

The latter two quantities (i.e. M_{max} and δ_H) are evaluated at the position of both, the middle cross section as well as the approximated inflection point (i.e. where the longitudinal bending curvature is zero); see Fig. 33. Further, δ_H is evaluated based on the 3D model “Loading” as follows:

$$\delta_H = \frac{u_{x,phase}}{R_{initial}} \tag{18}$$

In Equation (14), $u_{x,phase}$ is the horizontal phase displacement adopted from the final loading step at the side wall; $R_{initial}$ is the mean radius of the HWS lining.

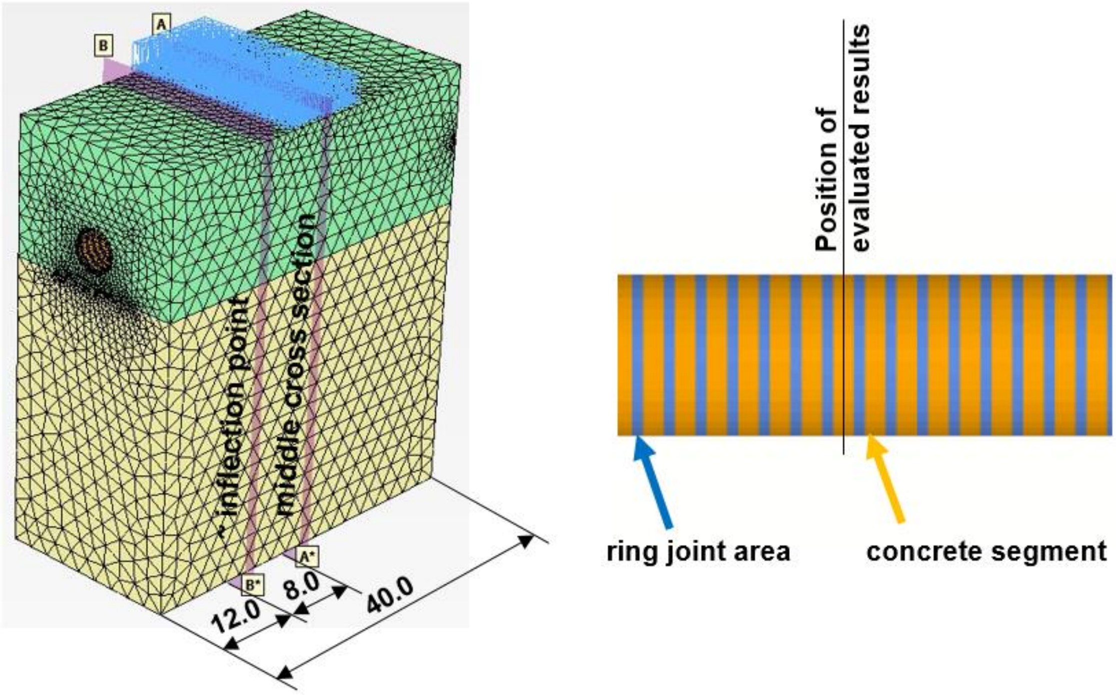
B
A
inflection point
middle cross section
B*
A*
12.0
8.0
40.0
Position of evaluated results
ring joint area
concrete segment

Fig. 33: Position of examined cross-sections

Step 6: In this step, final recommendations are given in order to account for segmental joints in the HWS structure. To this end, the anisotropic stiffness parameters E_1, E_2, G_{12}, G_{13},G_{23} and ν_{12} are determined based on the findings derived from the previous steps and subsequently presented in chapter 2.3. The latter are then applied for the large-scale model presented in chapter 3.

2.3 Results and discussion

All presented results refer to the final calculation phase. Both, loading as well as unloading conditions, are considered in the FEA. Hence, the results of this study have wide application to tasks that require in-depth analysis of the structural response of existing segmental tunnel linings to different construction activities such as excavations or embankment constructions. All calculation models are symmetrical with regard to the tunnel axis whereas a principal distinction is made between the model type, the ring joint modelling approach and the model dimensions, respectively; an overview is given in Tab. 5.

Tab. 5: Overview of performed analyses

Nr.	**Aim of analysis**		**Model type**			**Joint modelling**		**Model depth**	
			2D	2.5D	3D	direct	indirect	varied	constant
1	Cross-sectional structural behaviour (i.e. η)	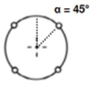	x	x		x	x	x	
2	Longitudinal structural behaviour (i.e. ξ)	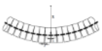			x		x		x
3	Model transformation (i.e. direct > indirect)				x	x	x		x
4	Joint-induced shear stiffness reduction (i.e. ζ)	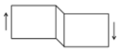			x	x			x

The basic idea of the abbreviations used in the legends of the diagrams is documented in Tab. 6. Presented internal forces occurring in the lining structure are defined according to Fig. 34.

Tab. 6: Abbreviations used in outputs

Variable	**Options**	**Reference**
Constitutive model	HSS I elastic	2.2.2.
Model type	2D I 2.5D I 3D	2.2.3.
Loading type	2-2.5D: Loading 1+2 I Unloading 1+2 3D: loading I unloading	2.2.3.
Rotational rigidity of longitudinal joint	fully hinged I rigid I uniform ring	2.2.4. (step 2)
Material type of circular plate elements	anisotropic I isotropic	2.2.4.
Longitudinal bending rigidity ratio	ξ_{Joint} I $\xi_{Cont.}$	2.2.4. (step 3+4)
Equivalent shear stiffness coefficient	ζ_{Joint}	2.2.4. (step 5)
Position of cross-section	middle cross section I inflection point	2.2.4. (step 5)

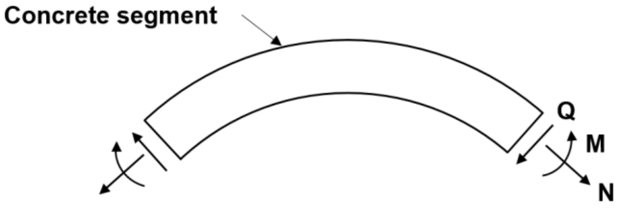

Fig. 34: Internal forces acting in the direction shown are considered as positive

2.3.1 Cross-sectional structural behaviour

- **Longitudinal joint modelling – Rotational rigidity K_{RO}**

The development of internal forces around the circumference of the lining structure obtained from 2D calculations is shown in Fig. 35, Fig. 36 and Fig. 37, respectively. In addition, Tab. 7 presents the absolute plate displacements occurring at different positions of the lining. The results represent upper and lower boundary values with respect to the possible output range since they constitute extreme K_{RO}-values (i.e. rigid, fully hinged, uniform ring). The used loading type definitions (i.e. Loading 1, Loading 2) are defined in Tab. 4. It is noted that the same conclusions can be drawn from the results in case of unloading conditions; hence, those results are not further described and only added in Appendix B.

The results clearly demonstrate that the rotational rigidity, defined at the position of longitudinal joints, does not affect the distribution of internal forces around the circumference of the tunnel at all; the same applies for the absolute lining displacements. In other words, the results indicate that the jointed cross section can be approached as uniform ring which corresponds to a η-value of 1.0. The obtained results are in accordance with the findings of Wood (1975) as briefly described in chapter 2.1.3. In the following, the HWS structure is therefore considered as a series of concrete segments separated by ring joints providing that the longitudinal joints have a minor effect on the structural behaviour. However, the following assumptions are made:

- Symmetrical (un)loading conditions
- Straight-jointed lining assembly
- Ring geometry composed of four segments
- No joint slipping of adjoining concrete segments[5]

Tab. 7: Absolute lining displacements (loading conditions)

absolute tunnel displacements [cm]				
loading type	rotational rigidity of longitudinal joint	crown, u_Y	invert, u_Y	side wall, u_X
Loading 1	rigid	-5.2	-1.1	±1.3
	fully hinged	-5.2	-1.1	±1.3
	uniform ring	-5.2	-1.1	±1.3
Loading 2	rigid	-16.0	-10.9	±1.1
	fully hinged	-16.0	-10.9	±1.1
	uniform ring	-16.0	-10.9	±1.1

---

[5] In Plaxis 2D 2018.01, the translational degrees of freedom between plate elements are fixed allowing for no translational movement in the joint area. Thus, this analysis does not consider deformations resulting from joint slipping.

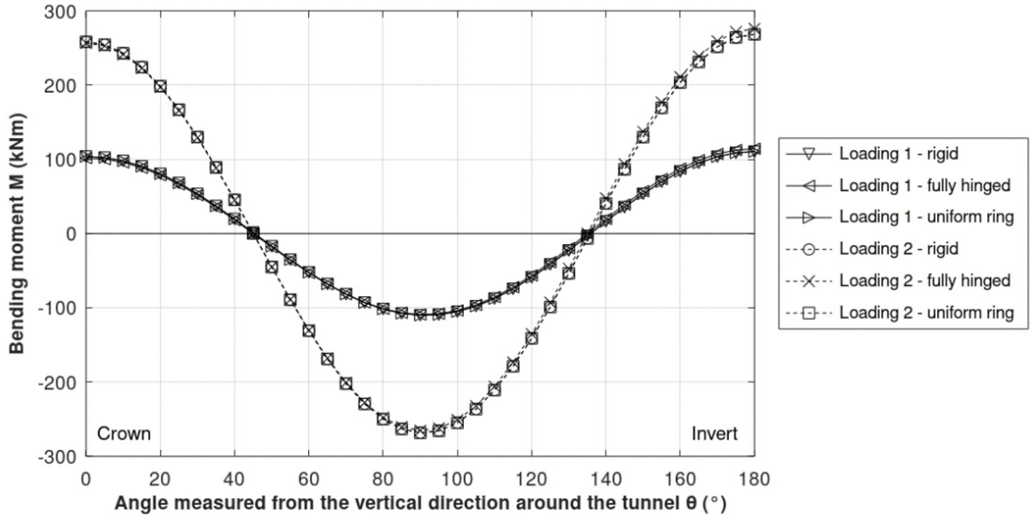

Fig. 35: Bending moment diagram considering different longitudinal joint configurations (loading conditions)

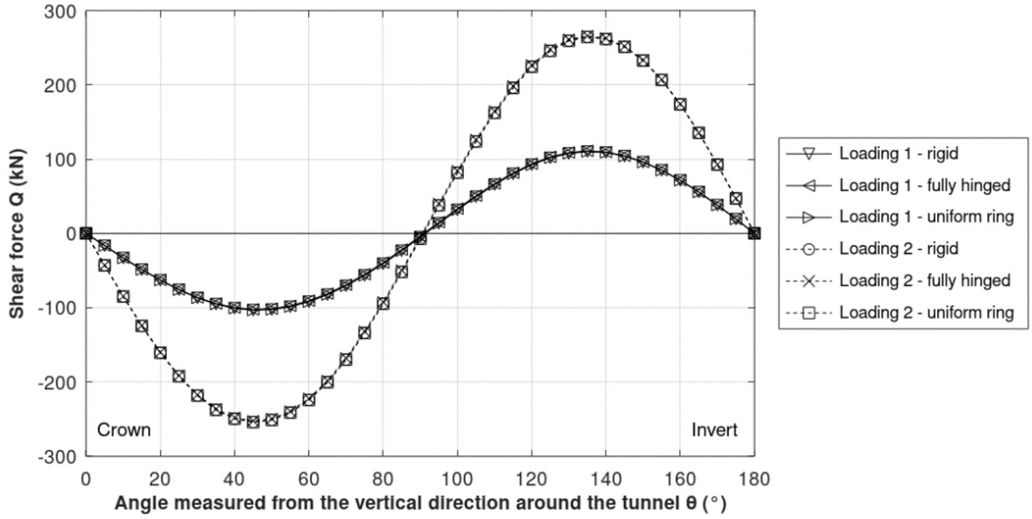

Fig. 36: Shear force diagram considering different longitudinal joint configurations (loading conditions)

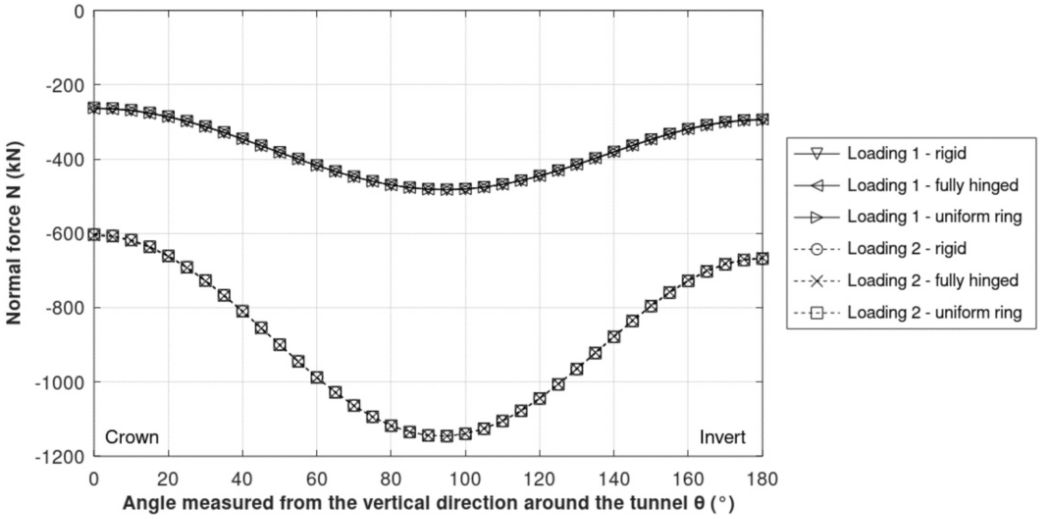

Fig. 37: Normal force diagram considering different longitudinal joint configurations (loading conditions)

- **2D versus "2.5D" modelling**

Considering the same model boundary conditions (i.e. excavation height, lining parameters, interface parameters, soil parameters, calculation phase sequence, shape function, model boundary conditions), this analysis aims to compare 2D results with those obtained from equivalent "2.5D" models; see section 2.2.3. Therefore, the obtained distribution of internal forces around the circumference of the tunnel induced by unloading is illustrated in Fig. 38, Fig. 39 and Fig. 40, whereas Tab. 8 documents absolute tunnel lining displacements.

The 2D results show good agreement with those obtained from the corresponding "2.5D" model with respect to both, the bending moment and shear force diagram whereas the max. difference is less than 5 %. The same holds true for the tunnel displacements whereby identical results are obtained at the investigated lining positions.

On the contrary, normal forces developing at both, the side wall as well as at the crown, are considerably affected by the model type; see Fig. 40. The "2.5D" model yields higher normal compressive forces at the crown (~15 %), while the normal forces at the side wall almost disappear. The latter is particularly critical to the lining design since the calculations predict max. bending moments at the side wall as well. In this case, the "2.5D" model would lead to a more conservative design of the lining. However, since both model geometries are expected to yield almost the same results, the obtained deviations may be attributed to the considered refinement of the mesh; hence, a mesh study might resolve that issue.

Tab. 8: Absolute lining displacements (unloading conditions)

absolute tunnel displacements [cm]				
loading type	model geometry	crown, u_Y	invert, u_Y	side wall, u_X
Unloading 1 (rigid)	2D	1.9	5.2	±1.6
	2.5D	1.9	5.2	±1.6
Unloading 1 (fully hinged)	2D	1.9	5.2	±1.6
	2.5D	1.9	5.2	±1.6

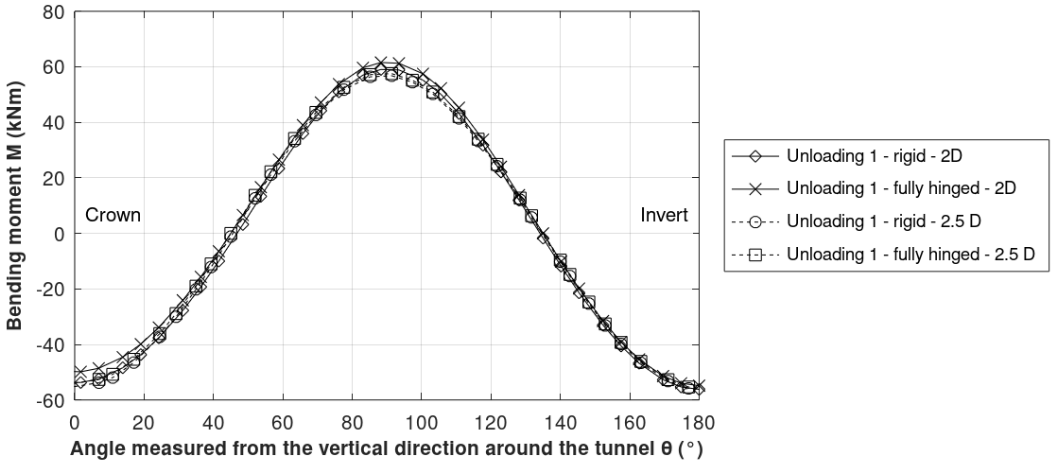

Fig. 38: Bending moment diagram comparing different model types (unloading conditions)

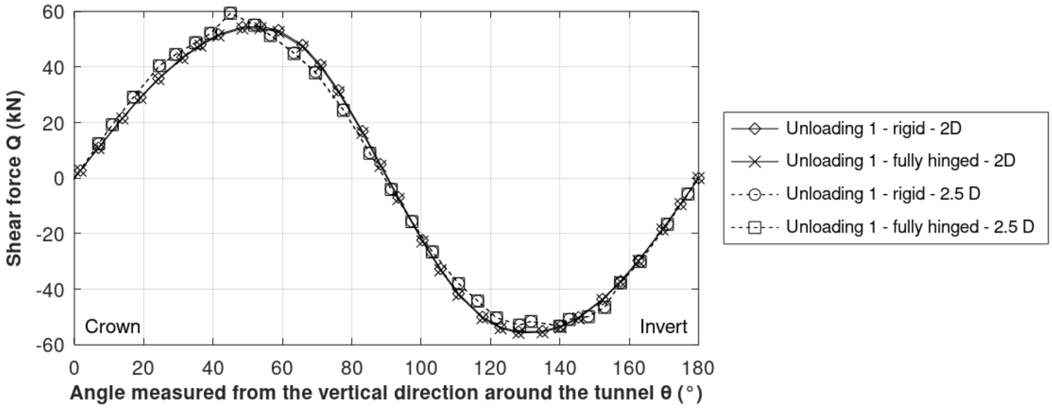

Fig. 39: Shear force diagram comparing different model types (unloading conditions)

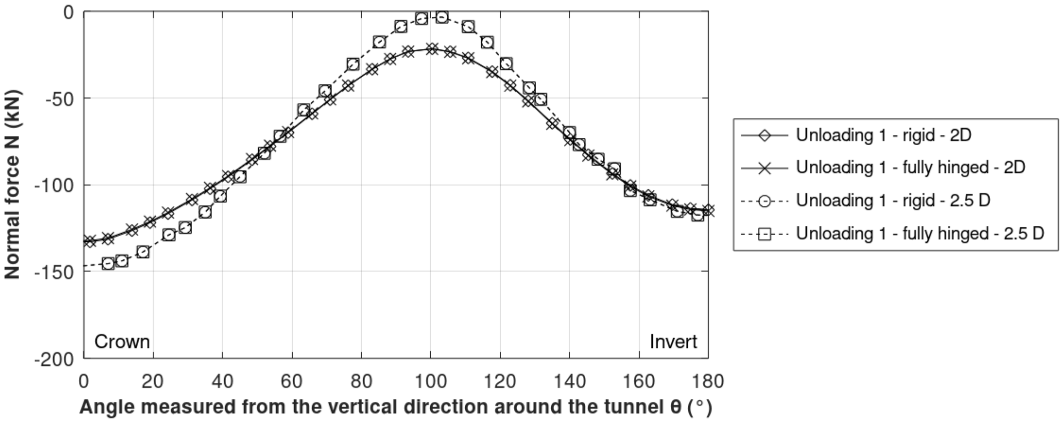

Fig. 40: Normal force diagram comparing different model types (unloading conditions)

- **Validation of model depth**

The used model dimensions for both, 2D as well as “2.5D” models, are consistent with the suggestions by EANG (2014); see Fig. 41. However, if additional boundary conditions (such as excavation activities above the tunnel axis) have to be considered, it is further recommended to validate the model size in order to assure that the model boundaries have an insignificant influence on the calculation results. To this end, additional 2D-calucations are performed in which the lower model boundary is shifted downwards by 20 m (this model is referred to as “deep” in Tab. 9). The “relative difference” gives an idea of the influence the model depth has on the obtained displacements; the calculated values are related to the shallow model depth option and further defined as follows:

$$rel.\ difference\ [\%] = 100\% \cdot \left(\frac{u_{y,deep}}{u_{y,shallow}} - 1 \right) \qquad (19)$$

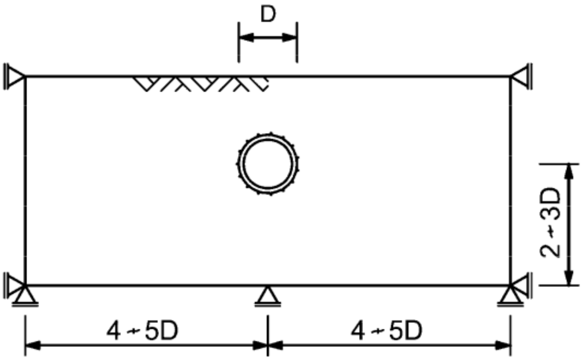

Fig. 41: Model size recommendations (EANG, 2014)

It becomes quite clear from Tab. 9 that the lining displacements are considerably affected by the model depth: The max. crown displacements are most affected if the lining is subjected to unloading conditions whereby the relative difference increases up to 168 % in case of Unloading 1. Lining displacements obtained at the invert are particularly influenced by the model depth if the lining is subjected to loading conditions; for Loading 1, the max. relative difference is 127 %. The horizontal displacements at the side wall are least affected; the max. relative difference is around 18 % for Loading 2. The results clearly emphasize the importance of validating the model dimensions.

Tab. 9: Relative differences of deformations (different model depths – joint configuration: rigid)

absolute tunnel displacements [cm]							
loading type	model depth	crown, u_Y	relative difference [%]	invert, u_Y	relative difference [%]	side wall, u_X	relative difference [%]
Loading 1	shallow	-5.2	29%	-1.1	127%	-1.3	0%
	deep	-6.7		-2.5		-1.3	
Loading 2	shallow	-16.0	66%	-10.9	97%	-1.1	-18%
	deep	-26.5		-21.5		-0.9	
Unloading 1	shallow	1.9	168%	5.2	60%	-1.6	0%
	deep	5.1		8.3		-1.6	
Unloading 2	shallow	2.8	161%	6.4	69%	-2.0	0%
	deep	7.3		10.8		-2.0	

2.3.2 Longitudinal structural behaviour

- **Determination of longitudinal bending rigidity ratio $\xi_{Cont.}$**

Tab. 10 summarizes the HWS-related input data required to determine the longitudinal bending rigidity ratio $\xi_{Cont.}$ as explained in Appendix A. Due to the fact that there is no reliable information about the influence length of the present ring joint L_f, a sensitivity study is first conducted to get a better understanding of its effect on $\xi_{Cont.}$.

Tab. 10: HWS-related input data required to determine $\xi_{Cont.}$

parameter		**value**	**unit**
Segmental length	L_S	0.8	m
Young's modulus	E_S	34	GPa
Number of longitudinal bolts	n	8	-
Translational bolt stiffness	K_b	105	MN/m
Cross section area	A_S	3.5	m^2
Influence length of ring joint	L_f	not defined	m
Note: Due to the nomenclature used in the analytical solution by Murakanu and Koizumi (1978), the segment height h is herein referred to as segment length L_S.			

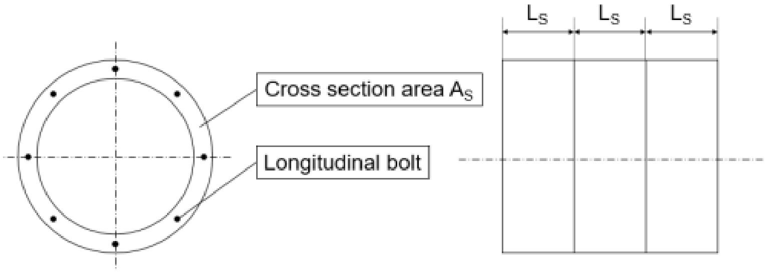

The longitudinal bending rigidity ratio decreases with increasing L_f-values, whereas $\xi_{Cont.}$ remains almost constant for L_f-values greater than 0.05 m; see Fig. 42. Since the flexural rigidity of jointed ring structures is lower compared to equivalent continuous ring structures, the observed tendency is reasonable; accordingly, $\xi_{Cont.}$ reaches its maximum if the ring joints disappear ($L_f = 0$ m). In Fig. 42, Liao et al. (2008) as well as Bao (2015) serve as guideline to mark a typical range of $\xi_{Cont.}$-values considered for segmental tunnel linings (i.e. 0.14-0.40). In the present case, two analytically obtained $\xi_{Cont.}$-values lie within the proposed range and therefore mark the basis for further considerations:

- 0.24 ($L_F = 3$ mm)
- 0.16 ($L_F = 5$ mm)

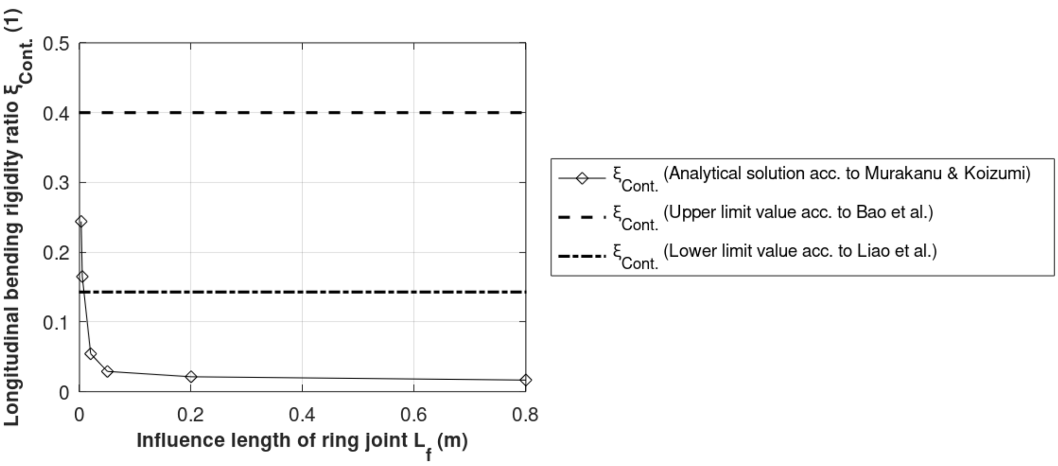

Fig. 42: Relationship between the influence length of the ring joint L_f and the longitudinal bending rigidity ratio $\xi_{Cont.}$

Additional 3D calculations are performed in order to study the effect of the ring-joint-induced longitudinal stiffness reduction on the deformation behaviour. As described in step 3 of the parameter derivation procedure in section 2.2.4, the HWS is modelled as continuous circular 3D plate element with anisotropic material in order to account for the presence of ring joints (i.e. indirect-joint model). To this end, both the bending stiffness and the normal stiffness in longitudinal direction are reduced whereas $\xi_{Cont.}$ is set to 0.16 and 0.24, respectively; see Equations (13-14). On the contrary, the circumferential stiffness remains unchanged in order to account for the findings of section 2.3.1 (i.e. $\eta = 1.0$). The lining parameters considered in the calculations are summarized in Tab. 11.

Tab. 11: Lining parameters considered in the 3D FEA of section 2.3.2

parameter		**value**			**unit**
Young's modulus in axial direction	E_1	5.6	8.3	34.0	GPa
Young's modulus in circumferential direction	E_2	34	34	34	GPa
In-plane shear modulus	G_{12}	14.2	14.2	14.2	GPa
Out-of-plane shear modulus	G_{23}	14.2	14.2	14.2	GPa
Out-of-plane shear modulus	G_{13}	14.2	14.2	14.2	GPa
Poisson's ratio	ν	0.2	0.2	0.2	-
Unit weight	γ	25	25	25	kN/m^3
		$\xi_{Cont.}$ = 0.16	**$\xi_{Cont.}$ = 0.24**	**isotropic**	
		segment + joint			

The structural consequence of reducing the longitudinal stiffness becomes quite clear from the vertical crown displacements plotted in Fig. 43 and Fig. 44: The differential displacements in longitudinal direction increase with decreasing $\xi_{Cont.}$-values. This tendency applies for both loading as well as unloading conditions. The latter is particularly relevant when assessing the leakage potential of segmental tunnel linings based on design criteria such as critical bending curvatures or differential displacements related threshold values.

The figures also indicate that the inflection points (i.e. points where bending curvature is 0) are about 1-1.2 x excavation width (i.e. 10 m) away from the excavation axis (y = 20 m); this roughly corresponds to what has been presented by Huang et al. (2013).

In the following, the influence length of the ring joint is defined as L_f = 3 mm which corresponds to the present ring joint thickness; see Fig. 17. Based on the analytical solution presented by Murakanu and Koizumi (1978), this gives a $\xi_{Cont.}$-value of 0.24 which in turn complies with the limit boundary values as described before[6]. In addition, the position of the inflection point is determined as 1.2 x excavation width away from the excavation axis; see Fig. 33.

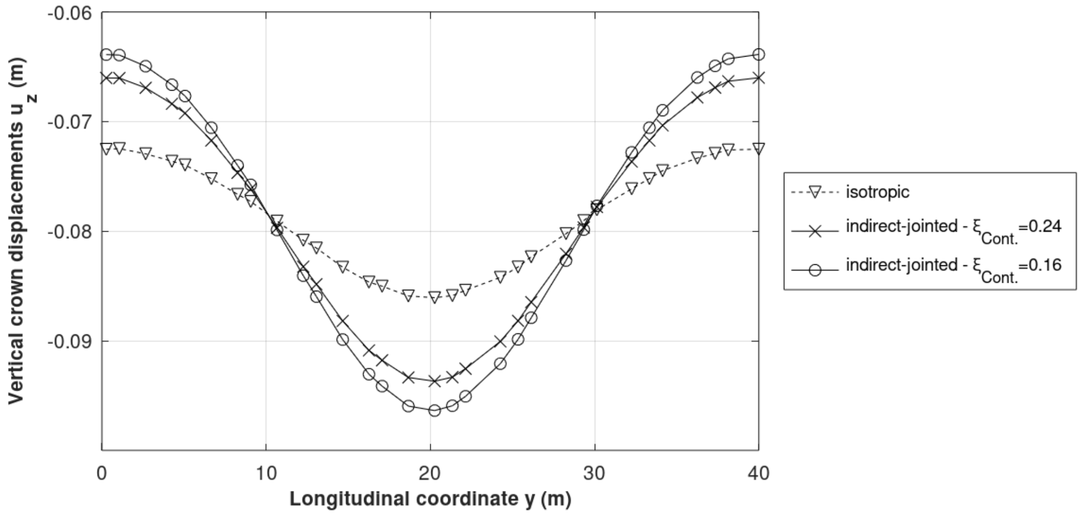

Fig. 43: Longitudinal distribution of vertical crown displacements (3D, loading)

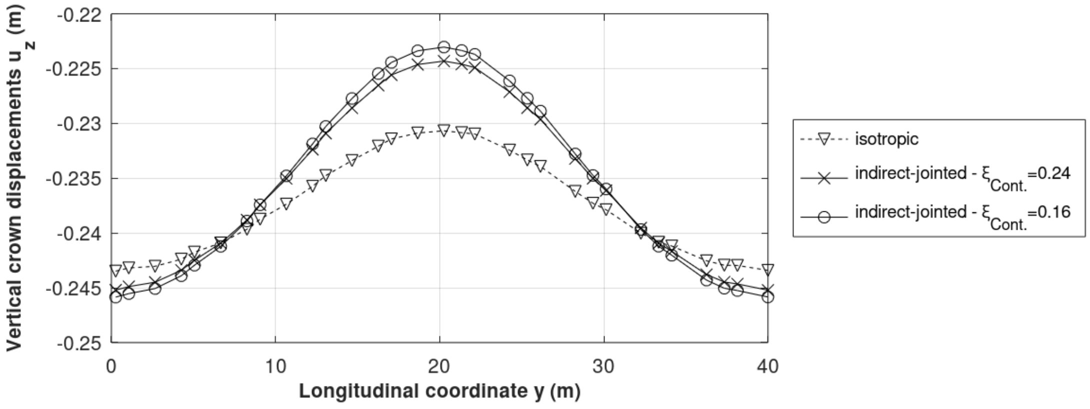

Fig. 44: Longitudinal distribution of vertical crown displacements (3D, unloading)

---

[6] Since there is no reliable information regarding the present L_f-value, L_f is defined such that the analytically derived longitudinal bending rigidity ratio $\xi_{Cont.}$ lies within a typical range proposed by Liao et al. (2008) and Bao (2015).

2.3.3 Indirect-joint vs. direct-joint modelling

- **Model calibration**

The indirect-joint model is transformed into a direct-joint model in order to study the consequences of a joint-induced shear stiffness reduction in more detail (as described in section 2.2.4). To provide consistency between both models, the vertical crown displacements developing in longitudinal direction are used as matching parameter for calibration purposes; see chapter 2.2.4. Therefore, the crown displacement curve derived from the indirect-joint model ($\xi_{Cont.}$=0.24) is used as reference for the calibration of the direct-joint model. In contrast to the indirect-joint model, in which the longitudinal stiffness is uniformly reduced along the entire tunnel length (see $\xi_{Cont.} = 0.24$ in Tab. 11), the corresponding stiffness reduction of the direct-joint model is restricted to the ring joint area (ξ_{Joint}) as described in Fig. 30. Hence, ξ_{Joint}-values have to be chosen lower than $\xi_{Cont.}$ to derive comparable crown displacement curves between both models. In this context, three sets of longitudinal rigidity ratios are adopted in the analysis: $\xi_{Joint} = 0.05$, 0.10, 0.16. The lining parameters considered in the calculations are summarized in Tab. 12.

Tab. 12: Lining parameters considered in the 3D FEA of section 2.3.3

parameter		value				unit
Young's modulus in axial direction	E_1	34.0	5.6	3.4	1.7	GPa
Young's modulus in circumferential direction	E_2	34	34	34	34	GPa
In-plane shear modulus	G_{12}	14.2	14.2	14.2	14.2	GPa
Out-of-plane shear modulus	G_{23}	14.2	14.2	14.2	14.2	GPa
Out-of-plane shear modulus	G_{13}	14.2	14.2	14.2	14.2	GPa
Poisson's ratio	ν	0.2	0.2	0.2	0.2	-
Unit weight	γ	25	25	25	25	kN/m^3
		isotropic	**ξ_{Joint}= 0.16**	**ξ_{Joint}= 0.10**	**ξ_{Joint}= 0.05**	
		segment	**joint**			

Similar to the observations made in section 2.2.2 for $\xi_{Cont.}$-values, the lining structure acts less stiff for decreasing ξ_{Joint}-values resulting in an increase of differential displacements in longitudinal direction; see Fig. 45 and Fig. 46. Considering the case of loading, the crown displacements of the indirect-joint model are best fit if ξ_{Joint} is less or equal 0.10. Fig. 47 indicates the tendency towards higher max. bending moments for increasing ξ_{Joint}-values. In this context, a significant drop of the max. bending moment can be observed if ξ_{Joint} is smaller than 0.10. In case of unloading, the crown displacement curve of the indirect-joint model shows good agreement with the direct-joint model when ξ_{Joint} is set 0.10. This further strengthens the assumption that the structural behaviour of the indirect-joint model can be best approximated by the direct-joint model if ξ_{Joint} equals 0.10 when compared to the other ξ_{Joint}–values considered in this study. Consequently, ξ_{Joint} is set 0.10 for further analysis in section 2.3.4.

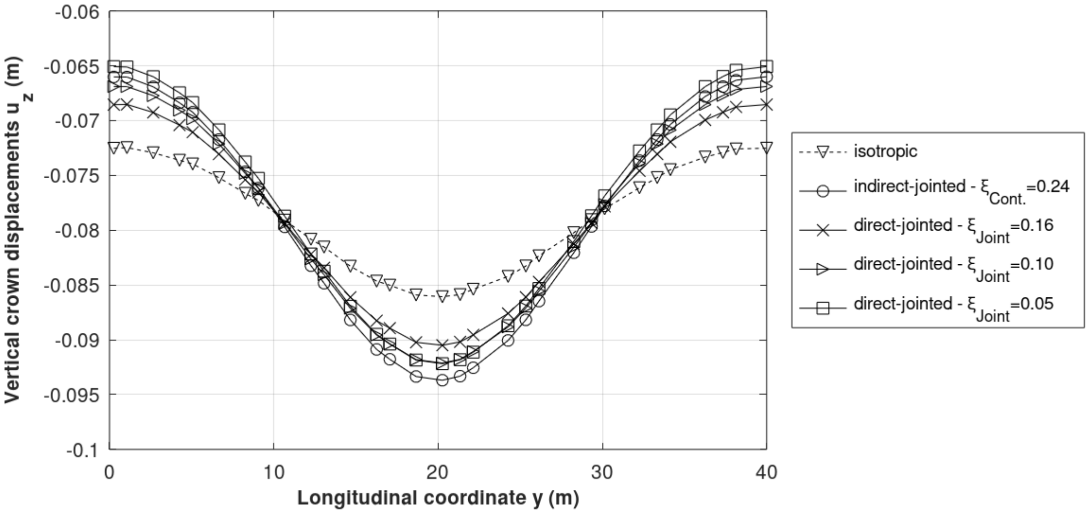

Fig. 45: Model calibration based on the longitudinal distribution of vertical crown displacements (3D, loading)

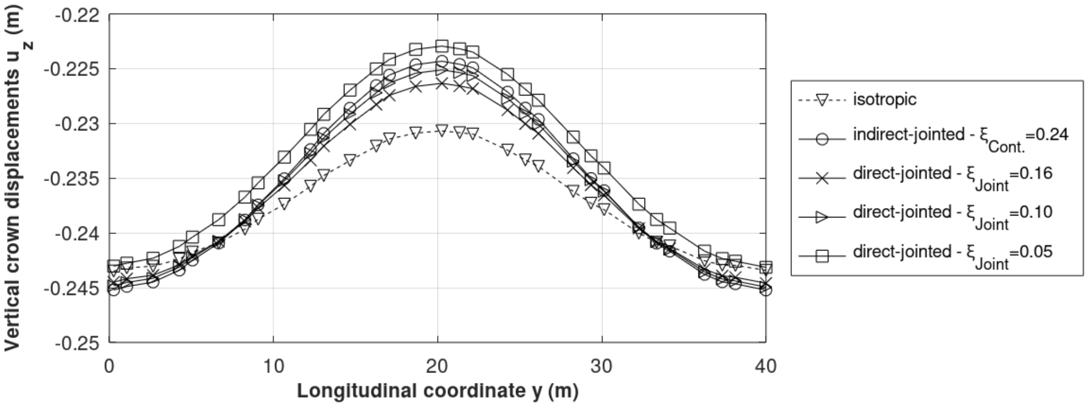

Fig. 46: Model calibration based on the longitudinal distribution of vertical crown displacements (3D, unloading)

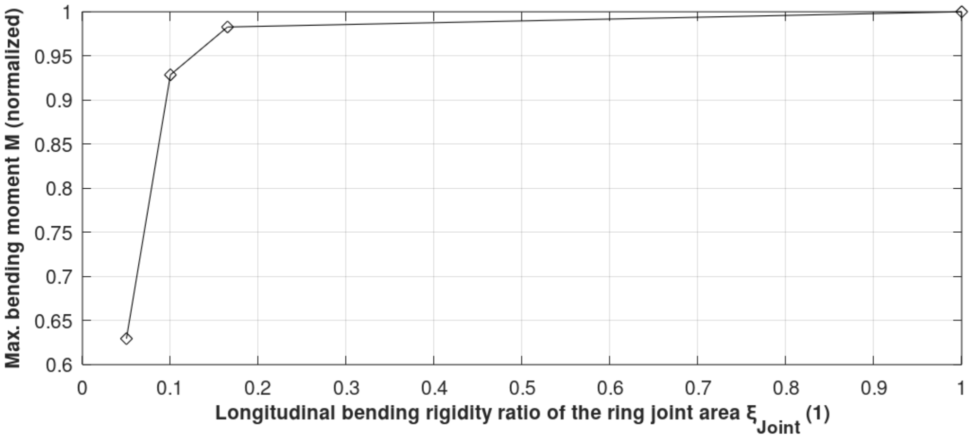

Fig. 47: Relationship between the longitudinal bending rigidity ratio in the ring joint area ξ_{Joint} and the max. bending moment M (3D, loading, middle cross section)

- **Effect on internal forces**

As shown in Fig. 47, the max. bending moment of the direct-joint model is significantly affected by the longitudinal bending rigidity ratios of the ring joint area ξ_{Joint}. This chapter further investigates the influence of the different modelling approaches on the internal forces. To this end, additional calculations are performed in which the lining is either modelled as indirect-jointed ($\xi_{Cont.}$=0.24), direct-jointed (ξ_{Joint}=0.10) or isotropic. The latter serves as reference in order to validate the results which are obtained at the position of both the middle cross-section and the inflection point; see Fig. 33.

Fig. 48 and Fig. 49 show the bending moments and shear forces developing around the circumference of the lining. The maximum values occur in the middle cross section whereas the corresponding peak values obtained in the inflection point are around 50 % lower. It can be further inferred from the results that the indirect-joint model gives slightly higher shear forces as well as bending moments when compared to the isotropic model. The latter tendency appears to be a consequence of the longitudinal stiffness reduction along the entire tunnel length resulting in an increased load transfer in the circumferential direction. However, from a practical point of view, all modelling approaches yield practically similar results with respect to both, shear forces and bending moments around the circumference of the lining.

A significant difference can be observed from the normal force diagram plotted in Fig. 50: While the normal force diagram shows good agreement between the isotropic and the indirect-joint model, the results of the direct-joint model differ substantially. Most significantly, the latter predicts tension normal forces at the tunnel crown which is regarded as unrealistic when the lining is subjected to loading. Consequently, further studies would be required to resolve this contradiction.

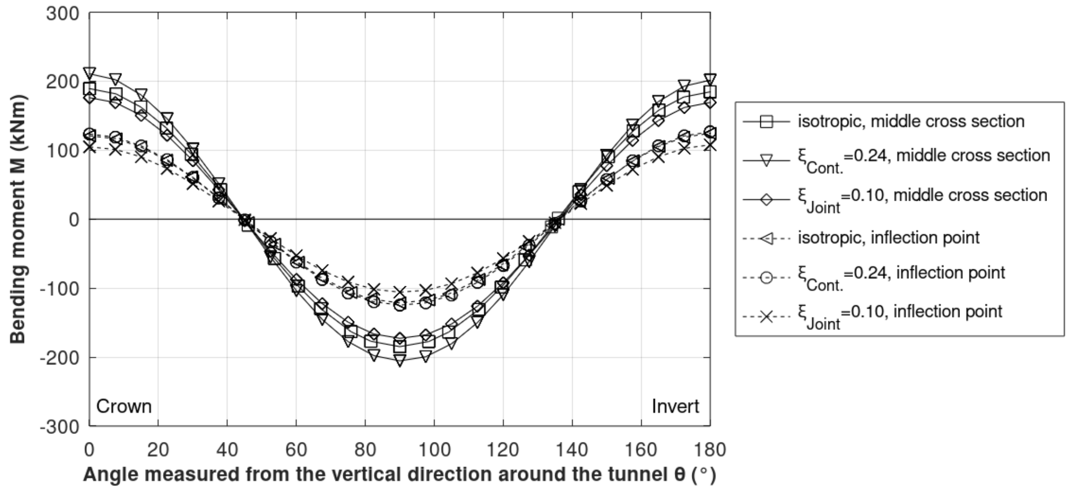

Fig. 48: Bending moment diagram (3D, loading)

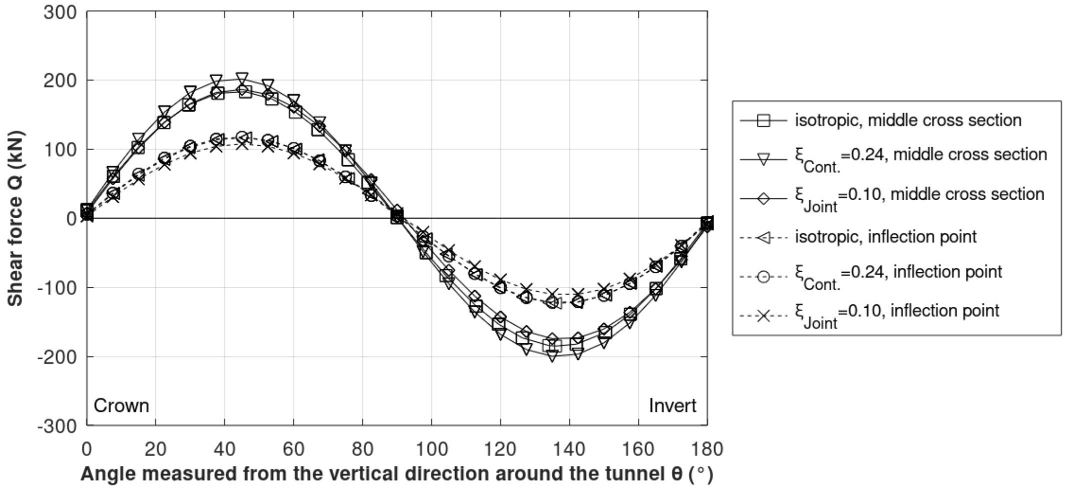

Fig. 49: Shear force diagram (3D, loading)

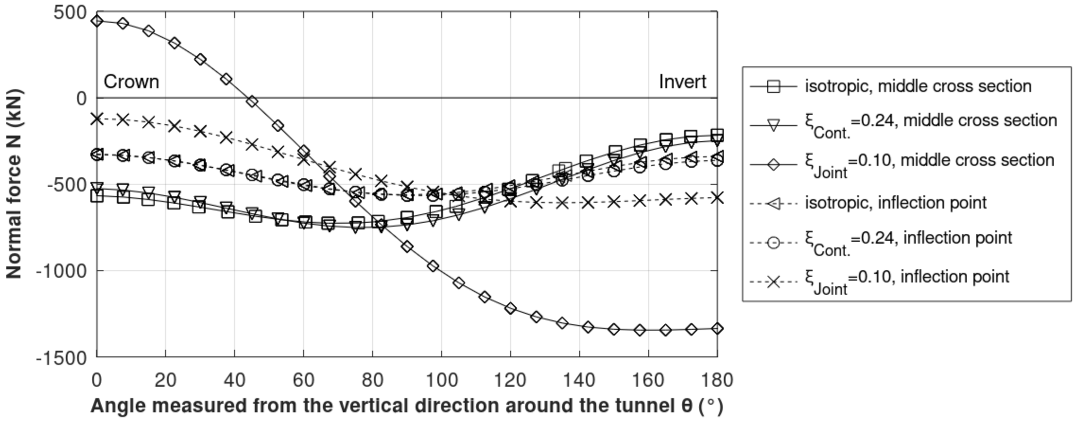

Fig. 50: Normal force diagram (3D, loading)

2.3.4 Joint-induced shear stiffness reduction

This chapter aims to analyse the effect of the joint-induced shear stiffness reduction on the structural lining behaviour using the calibrated direct-joint model parameters (see $\xi_{Joint} = 0.10$ in Tab. 12). As previously described in section 2.2.4, the total shear deformations of the HWS are regarded as the sum of the shearing of the concrete segments themselves and the shear-induced offsets at the joints; in this context, the latter is accounted for by introducing the shear stiffness reduction ratio of the ring joint area ζ_{Joint}. The lining parameters adopted in the analysis are summarized in Tab. 13.

Tab. 13: Lining parameters considered in the 3D FEA of section 2.3.4

parameter		value							unit
Young's modulus in axial direction	E_1	34.0	3.4	3.4	3.4	3.4	3.4	3.4	GPa
Young's modulus in circumferential direction	E_2	34	34	34	34	34	34	34	GPa
In-plane shear modulus	G_{12}	14.2	14.2	7.1	4.3	1.4	0.7	0.1	GPa
Out-of-plane shear modulus	G_{23}	14.2	14.2	14.2	14.2	14.2	14.2	14.2	GPa
Out-of-plane shear modulus	G_{13}	14.2	14.2	7.1	4.3	1.4	0.7	0.1	GPa
Poisson's ratio	ν	0.2	0.2	0.2	0.2	0.2	0.2	0.2	-
Unit weight	γ	25	25	25	25	25	25	25	kN/m^3
Joint-induced shear stiffness ratio	ζ_{Joint}	1.0	1.0	0.50	0.30	0.10	0.05	0.01	-
		isotropic	**$\xi_{Joint} = 0.10$**						
		segment	**joint**						

- **Effect on longitudinal crown displacement curve**

As expected, reducing the shear stiffness (i.e. $\zeta_{Joint} < 1$) results in an increase of the differential displacements for both loading as well as unloading conditions; see Fig. 51 and Fig. 52. The tendency towards increased differential displacements can be explained by additional translational movements at the ring joints (i.e. joint slipping) which is herein accounted for by reducing the shear stiffness; see chapter 2.2.4. It can be further inferred from the results that the crown displacements are almost not affected for ζ_{Joint}-values greater than or equal to 0.30. On the contrary, crown displacements are significantly influenced when the equivalent shear stiffness ζ_{Joint} is smaller than 0.10 indicating a much softer longitudinal deformation behaviour. Since bending is considered the most important type of deformation with respect to tunnel linings (Yu et al., 2019), ζ_{Joint}-values smaller than 0.10 may overestimate the crown displacements.

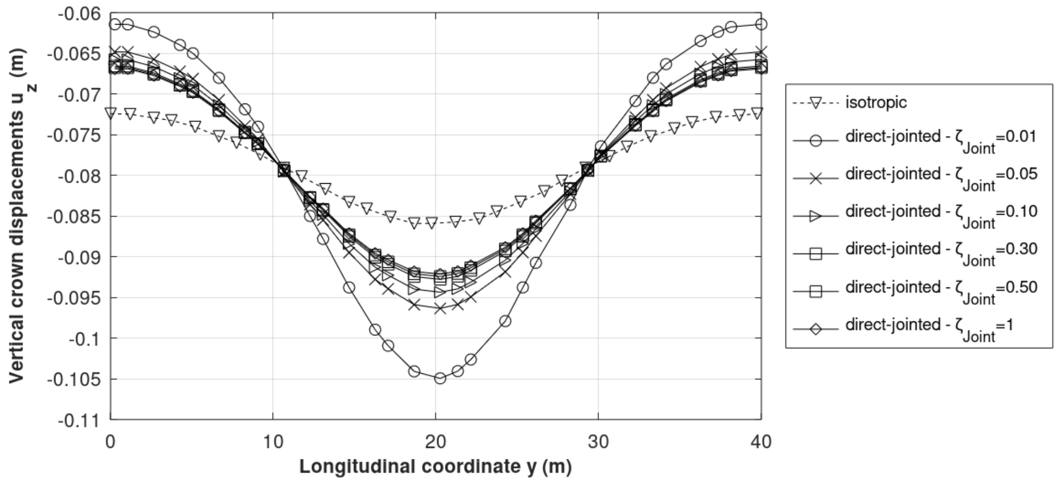

Fig. 51: Effect of the shear stiffness reduction on the longitudinal distribution of vertical crown displacements (3D, loading)

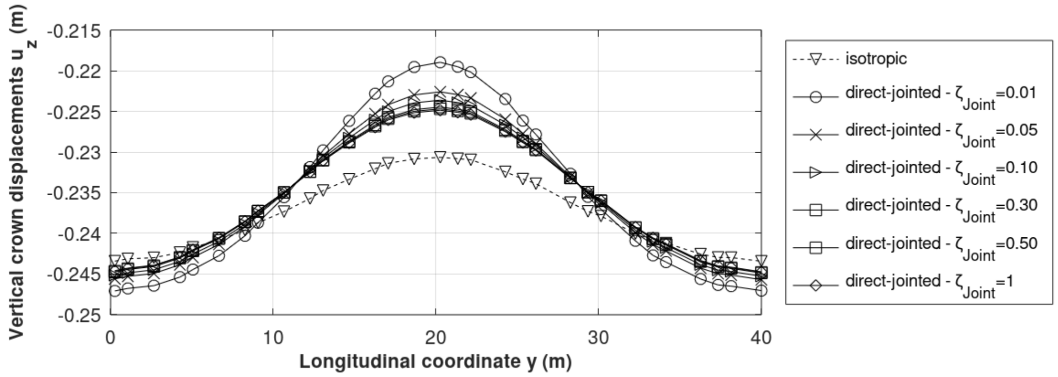

Fig. 52: Effect of the shear stiffness reduction on the longitudinal distribution of vertical crown displacements (3D, unloading)

- **Effect on max. bending moment**

When the lining is subjected to loading conditions, strengthening the shear stiffness leads to decreasing max. bending moments in the cross section as shown in Fig. 53; further results are given in Appendix B. This shear stiffness dependence is observed for both the *HSS* as well as the elastic ($E = 5$ MPa, $\nu = 0.2$, $\gamma = 20$ kN/m^3) constitutive model for the soil whereas the latter predicts lower variations of the max. bending moment. The obtained results agree with the observations made in Liao et al. (2008).

However, an interesting behaviour is that the opposite tendency is observed when unloading conditions are considered; in other words, an increase in shear stiffness leads to higher max. bending moments. This again applies for the *HSS* as well as for the elastic constitutive model. Thus, it is concluded that the recommendations regarding structural measures for segmental tunnel linings presented by Liao et al. (2008)are restricted to loading conditions (i.e. the shear resistance ability between rings should be strengthened in order to reduce the additional internal forces induced by ground displacement). However, similar to what has been observed for the crown displacements, the max. bending moments are almost constant if ζ_{Joint}-values are set greater than or equal 0.30.

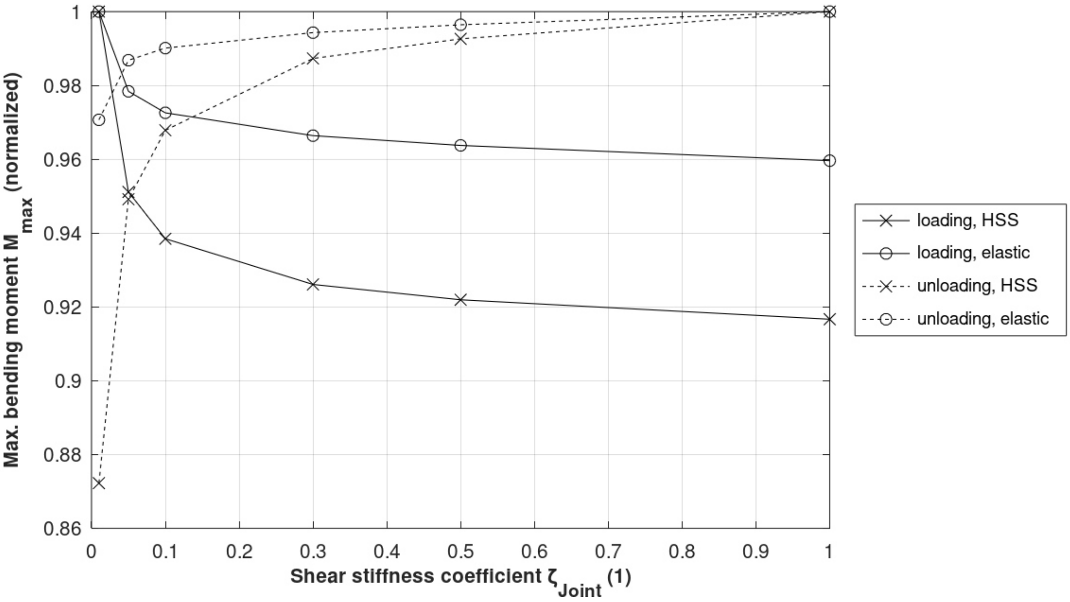

Fig. 53: Relationship between shear stiffness coefficient ζ_{Joint} and max. bending moment M_{max}

- **Effect on ovalization**

Huang et al. (2012) found that tunnel flattening can inter alia be attributed to differential displacements occurring in the longitudinal direction. As shown in the previous paragraphs, the latter are particularly affected by ζ_{Joint}-values smaller than 0.30. Accordingly, the shear-stiffness reduction may also induce additional ovalization of the cross section leading to additional internal forces; see chapter 2.1.2. This section therefore investigates the ovalization dependence on the shear stiffness. Fig. 54 indicates an increase in tunnel flattening for decreasing ζ_{Joint}-values at the position of the middle cross section. It is further shown that tunnel flattening is hardly affected for ζ_{Joint}-values greater than 0.10 which is also the case for the crown displacements in longitudinal direction and the max. bending moment in the cross section. At the position of the inflection point, the shear stiffness dependence of the lining ovalization seems insignificant.

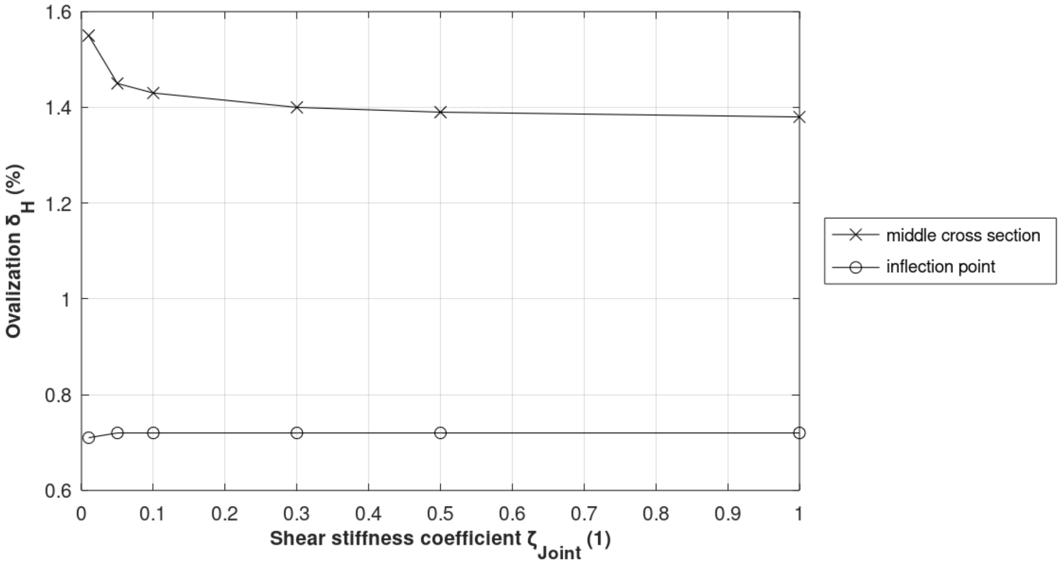

Fig. 54: Relationship between shear stiffness coefficient ζ_{Joint} and ovalization δ_H

2.4 Implications for large-scale model

The subsequent conclusions are drawn from the results presented in section 2.3. Based on the deduced information, recommendations are given for modelling the HWS structure which are then further used to analyse the structural response of the HWS drainage tunnel to the excavation activities of construction lot “Wolframstraße” in chapter 3.

- **2D vs. “2.5D”**

In many cases, 2D calculations presume plane-strain conditions for the analysis of linear structures (i.e. the associated strain in longitudinal direction is zero). Thereby, 2D models are useful to approximate 3D problems such as tunnel structures or dams mainly subjected to evenly distributed loads along the axial coordinate. In this way, both calculation effort and time can be significantly reduced, allowing for a cost-efficient design.

As expected, the results presented in section 2.3.1 confirm that 3D geometries representing plane-strain conditions (i.e. 2D geometries uniformly stretched in axial direction which is herein referred to as “2.5D”) yield almost identical results when compared with equivalent 2D models with respect to lining displacements, bending moments and shear forces, respectively. However, deviations are observed when comparing the normal force distribution around the circumference which can be either attributed to the mesh or the shape function. In this context, further investigations might resolve this contradiction.

- **Model depth**

The results are significantly affected by the model depth. In particular, the vertical displacements obtained at both the tunnel crown and invert are falsified if the model depth lacks thorough validation. This is particularly crucial to the large-scale model presented in section 3 since the lining displacements are one of the key issues of the 3D *FEA*. To this end, it is recommended to use the distribution of state parameter 8 of the *HSS* model (i.e. G/G_{ur}) as validation tool in order to consider a reasonable model depth as subsequently shown in the large-scale model in section 3.3.1.

- **Longitudinal joint modelling**

Assuming a stagger-jointed lining assembly and symmetrical loading conditions, the cross sectional behaviour of the HWS is hardly affected by its longitudinal joints when the latter are considered as rotational springs; see 2.3.1. The obtained results are further confirmed by the statements issued by Wood (1975). In other words, in the present case, the jointed cross section can be modelled as uniform ring which corresponds to an effective transversal bending rigidity ratio η of 1. As a consequence, the tunnel structure is further on approached as a series of uniform rings separated by ring joints.

- **Joint-induced shear stiffness reduction**

The HWS lining is modelled as indirect-joint model as well as direct-joint model; see Fig. 30. The material parameters of the indirect-joint model are defined based on the analytical solution proposed by Murakanu and Koizumi (1978). The indirect-joint model is further chosen as reference to determine the material parameters of the direct-joint model; in this context, the obtained crown displacement curve of the indirect-joint model is used as matching parameter to provide consistency between both models. The calibrated direct-joint model is then employed to study the consequences of the joint-induced shear stiffness reduction in more detail.

The results clearly demonstrate that the structural behaviour of the tunnel is particularly sensitive to ζ_{Joint}-values smaller than 0.3 which represents a quite low shear stiffness in the ring joint area. It can be further inferred from the results that the max. cross sectional bending moments decrease with an increase in shear stiffness ($\zeta_{Joint}\uparrow$) when the structure is subjected to loading conditions; this tendency is well in agreement with what has been presented by Liao et al. (2008). However, an opposing tendency is observed when unloading conditions are considered. Hence, recommendations regarding the conceptual design of segmental tunnel linings presented by Liao et al. (2008) are restricted to loading conditions.

- **Inflection point vs. middle cross section**

As expected, the distribution of internal forces at the middle cross section yields higher values compared to the ones at the inflection point; however, one exception is observed at the tunnel invert where the compressive normal forces give higher values at the inflection point. The analyses also indicate that the ovalization effect in the middle cross section is more pronounced.

- **Direct-joint vs. indirect-joint model**

In the analyses, the HWS structure is either modelled as direct-jointed or indirect-jointed whereas the results are also compared to the isotropic modelling option. While the direct-joint model allows for a more detailed investigation of the structural effects of the joint-induced shear stiffness reduction, it requires higher modelling effort compared to the indirect-joint model; in addition, significant deviations with respect to the predicted normal force distribution around the circumference of the tunnel lining are observed which require further investigations.

- **HWS modelling recommendations**

In the present case, the application of the direct-joint model is restricted to the analysis of the shear stiffness reduction and not further extended to the large-scale model. The tunnel lining is therefore modelled as circular plate element with anisotropic material behaviour (i.e. indirect-joint model). In this context, both the bending as well as the normal stiffness in longitudinal direction are reduced by applying the longitudinal bending rigidity ratio ($\xi_{Cont.}$= 0.24).

On the contrary, the equivalent stiffness components in circumferential direction are not modified as the tunnel cross section behaves as uniform ring (η = 1). Since the determination of the shear stiffness reduction would be left to pure conjecture, the shear stiffness is not modified as well (ζ_{Joint} = 1). The recommended material parameters of the HWS for the large-scale model presented in the following chapter are summarized in Tab. 14.

Tab. 14: Recommended lining parameters for the large-scale model

parameter		value	unit
Young's modulus in axial direction	E_1	8.3	GPa
Young's modulus in circumferential direction	E_2	34	GPa
In-plane shear modulus	G_{12}	14.2	GPa
Out-of-plane shear modulus	G_{23}	14.2	GPa
Out-of-plane shear modulus	G_{13}	14.2	GPa
Poisson's ratio	ν	0.2	-
Unit weight	γ	25	kN/m^3

3 Construction lot “Wolframstraße”: 3D-FEA

The main objective of chapter 3 is to summarize results from three-dimensional finite element analyses performed in order to assess the structural response of the existing drainage tunnel (HWS) as a consequence of the construction process of building lot “Wolframstraße”; see Fig. 55. The 3D *FEA* of the this construction project, which was successfully finished in the first half of 2019, are conducted using the FE software Plaxis 3D 2018.01 (Brinkgreve et al., 2018a). Based on the recommendations given in chapter 2, the drainage tunnel is modelled as indirect-joint model with anisotropic material behaviour to account for the presence of segmental joints; see Tab. 14. The following aspects are discussed in more detail:

- Identification of modelling parameters affecting the lining displacements
- Analysis of the structural lining behaviour during the construction process
- Position of the max. lining displacements at different cross-section
- Deviations resulting from different HWS modelling approaches
- Structural consequences of hydraulic inner pressure due to extensive rainfalls
- Qualitative assessment regarding the reinforcement design of selected piles

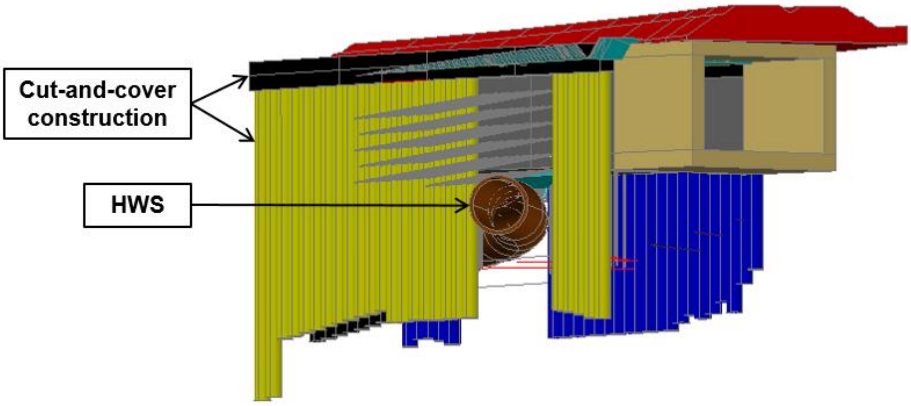

Fig. 55: 3D model illustrating the newly-built cut-and-cover construction and the existing subjacent HWS drainage tunnel

Modelling parameters and planning documents used in this chapter are taken from the respective static report provided by ILF Consulting Engineers Austria GmbH (Summerer and Hosp, 2018). The results of this chapter will be compared to the existing 2D *FEA* which were performed prior to this thesis by the project partner. In addition, the results of in-situ measurements will be used to validate the results of the present 3D *FEA*. However, both tasks are beyond the scope of this thesis and will therefore be addressed in an additional paper.

3.1 Project description and construction process

As integral part of the large-scale project Stuttgart 21, the existing central station “Kopfbahnhof” is converted from an existing terminal configuration to an underground through station. Thereby, the construction lot “Wolframstraße” establishes the underground railway passage approaching the “Kopfbahnhof” from northeast; see Fig. 56. Main challenges that had to be concerned during the design phase of this project are described in section 2.2.1.

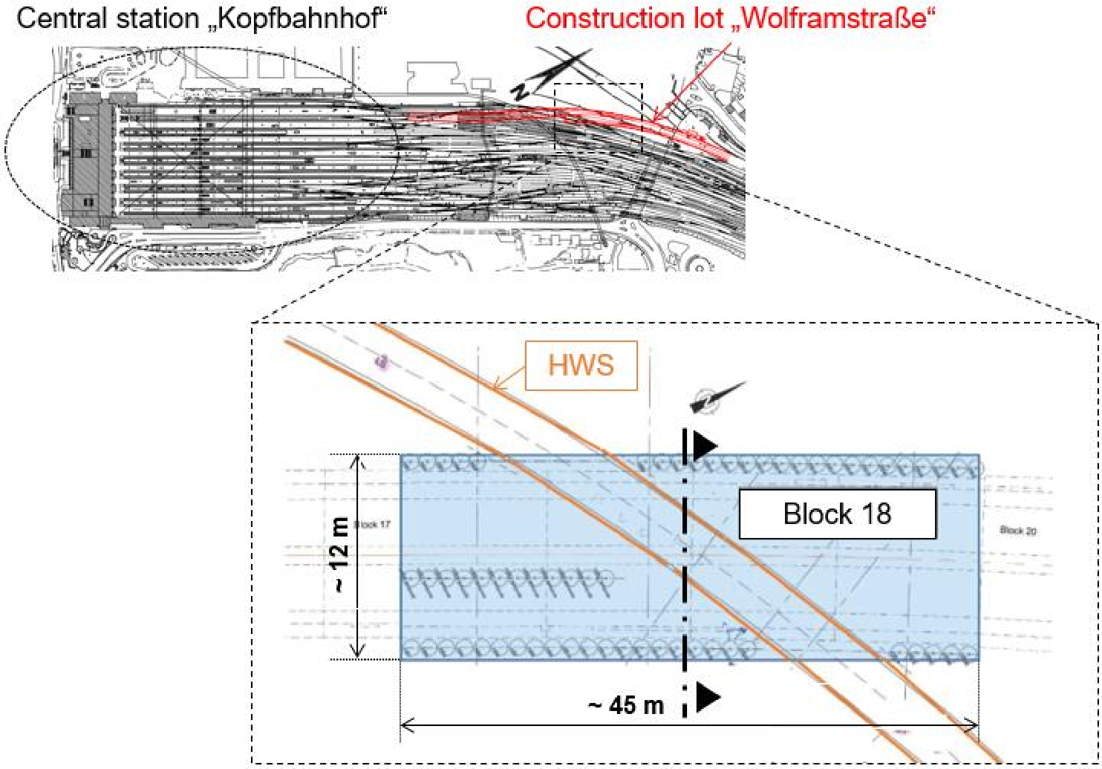
Central station „Kopfbahnhof“
Construction lot „Wolframstraße“
HWS
Block 17
Block 18
Block 20
~ 12 m
~ 45 m

Fig. 56: General project overview (left); Plan view of Block 18 and HWS (right)

The construction of Block 18 requires extensive constructional measures in order to ensure that the excavation-induced HWS-deformations stay below proposed alarm values: After finishing the working plane, both the roof slab and the pile walls are constructed using the cut-and-cover method; see Fig. 57 and Fig. 58. In the vicinity of the HWS, the construction of pile walls is not possible. Hence, in this area both, soil nails and shotcrete walls provide the lateral support of Block 18; consequently, they have to be installed simultaneously with the excavation progress to provide the stability of the excavation area. Following the first excavation step down to z = -6.5 m, vertical micropiles are installed around 10 m apart on both sides of the HWS axis whereas the micropile heads are placed at excavation level 3 (z = -10.6 m). The micropiles, which are then subjected to tension as a consequence of the excavation process, reinforce the soil and therefore reduce ground heave. In the second excavation phase, the soil is excavated down to z = -8.0 m. The final excavation phase (z = -10.6 m) is divided into three sub steps (i.e. 3.1, 3.2, 3.3) whereby each sequence covers an excavation width of ~ 4.0 m.

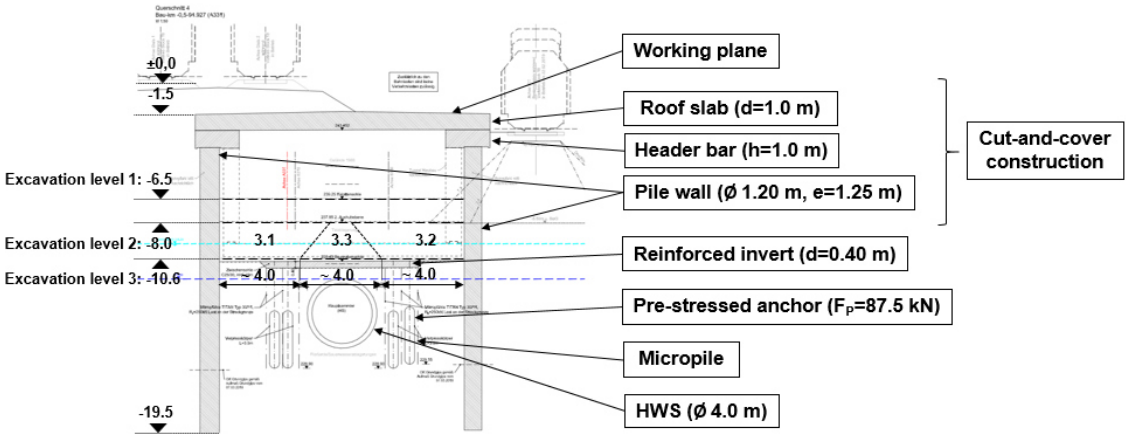
±0,0
-1.5
Excavation level 1: -6.5
Excavation level 2: -8.0
Excavation level 3: -10.6
-19.5
3.1
3.3
3.2
~4.0
~4.0
~4.0
Working plane
Roof slab (d=1.0 m)
Header bar (h=1.0 m)
Pile wall (Ø 1.20 m, e=1.25 m)
Cut-and-cover construction
Reinforced invert (d=0.40 m)
Pre-stressed anchor (F_P=87.5 kN)
Micropile
HWS (Ø 4.0 m)

Fig. 57: Cross section of Block 18

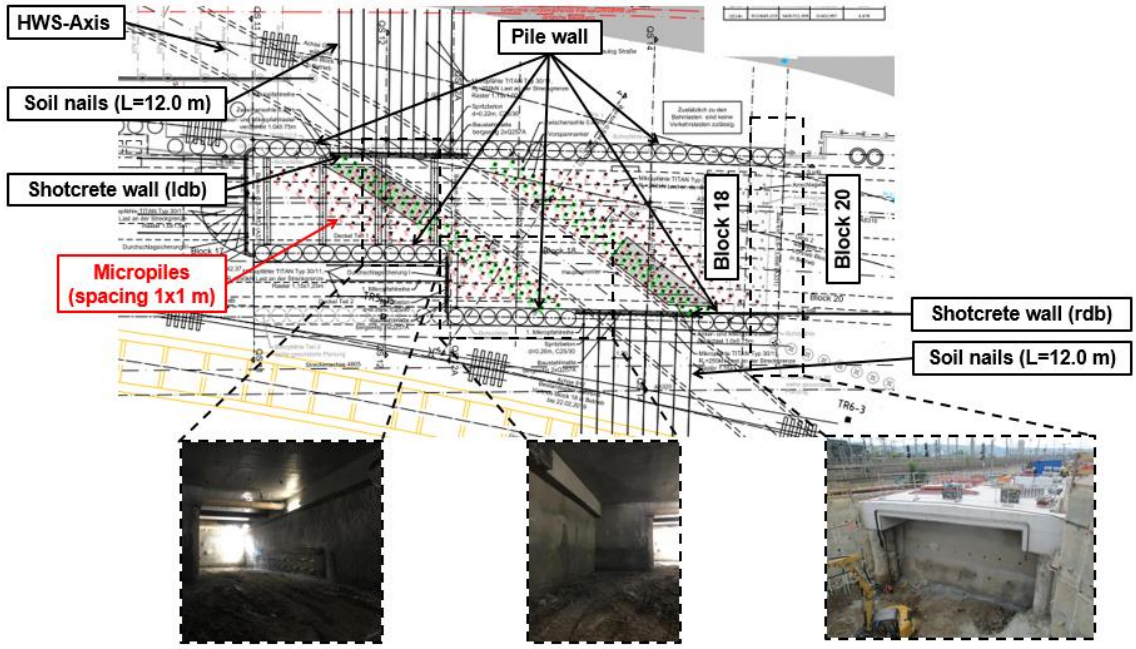
HWS-Axis
Soil nails (L=12.0 m)
Shotcrete wall (ldb)
Micropiles (spacing 1x1 m)
Pile wall
Block 18
Block 20
Shotcrete wall (rdb)
Soil nails (L=12.0 m)

Fig. 58: Plan view of Block 18 covering structural elements and on-site photos

Each sub excavation step is succeeded by two construction processes: the construction of a reinforced invert and the installation of pre-stressed ground anchors; see Fig. 59. Those measures counteract hydraulic radial forces resulting from extensive rainfalls that might flaw the integrity of the lining as described in section 2.2.1.

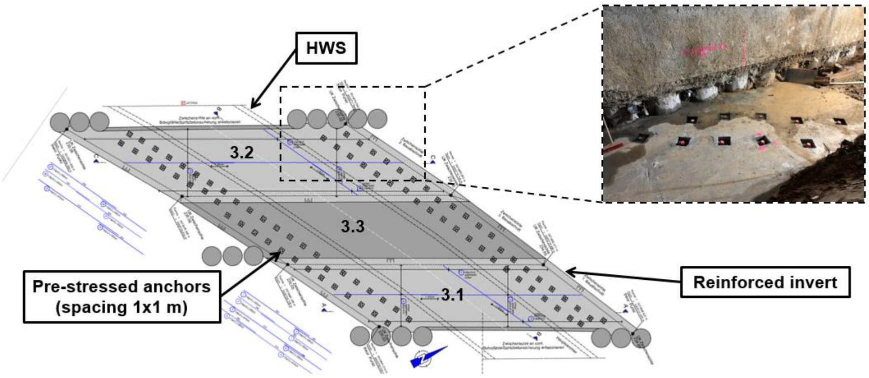
HWS
3.2
3.3
3.1
Pre-stressed anchors (spacing 1x1 m)
Reinforced invert

Fig. 59: Plan view of reinforced invert and corresponding on-site photo

Fig. 60 shows the present soil profile which consists of four different soil layers. Groundwater is present from -10.6 m below surface which corresponds to the final excavation level. The position of the soil layers is defined as follows:

- z = 0 to -6 m: Anthropogenic backfill material
- z = -6 to -11 m: Stillwater sediments
- z = -11 to -17 m: Fließerde
- z < -17 : Keuper marl

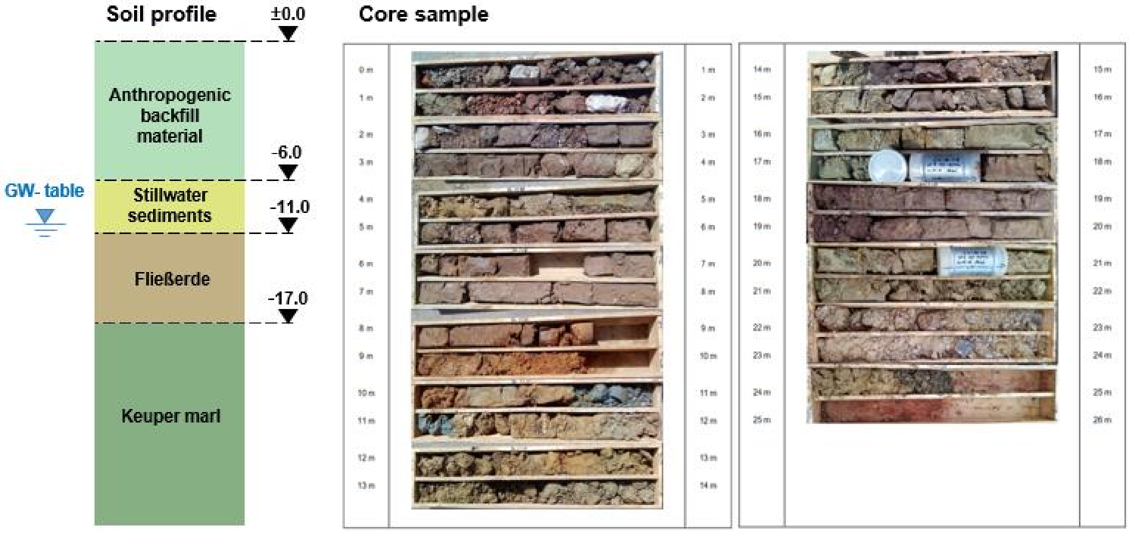
Soil profile
±0.0
Anthropogenic backfill material
-6.0
GW- table
Stillwater sediments
-11.0
Fließerde
-17.0
Keuper marl
Core sample

Fig. 60: Soil profile as well as respective core sample

3.2 Modelling Approach

So far this chapter recalled both the conceptual framework of the project as well as the arising subjects of investigation. Within the subsequent section the 3D FE modelling approach is documented in more detail. Therefore, general information is given about the geometry, input parameters describing both, the soil behaviour and the used structural elements, the calculation phase sequence and considerations regarding the simplification of complex structures. Specific project data with respect to structural elements, soil conditions and the construction process are adopted in accordance with the detailed planning design documents which were provided by the project partner; see Summerer and Hosp (2018).

3.2.1 Geometry and mesh configuration

The overall model dimensions x/y/z are 120/90/55 m which ensure a negligible influence of the boundary conditions as demonstrated in section 3.3.1. The FE mesh consists of approximately 1.150.000 10-noded elements (quadratic shape function) corresponding to a second-order interpolation of displacements. The mesh is locally refined in the construction area of Block 18 in order to consider the stress distribution (and redistribution during the different construction phases) in the region of the HWS reasonably; see Fig. 61.

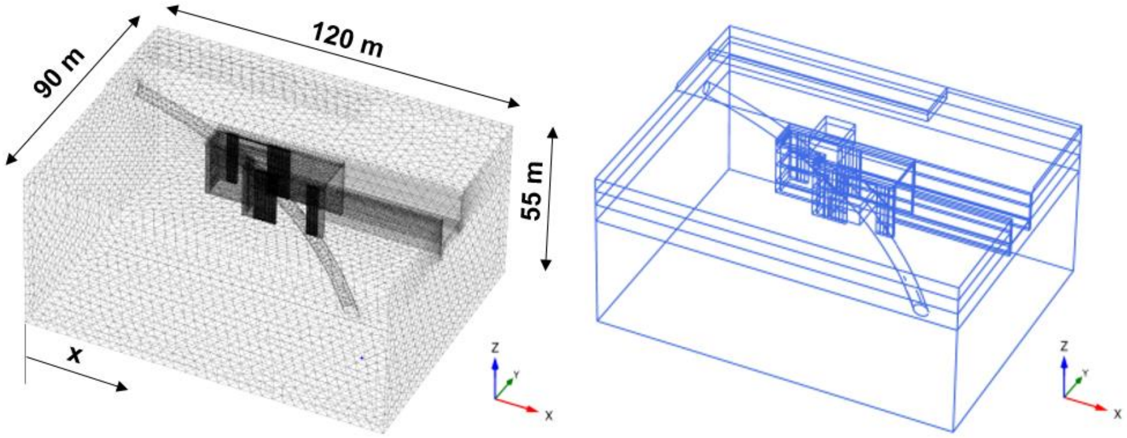

Fig. 61: FE mesh and geometric model

3.2.2 Soil conditions and constitutive model

The soil parameters adopted in the analyses stem from both pressiometer tests as well as triaxial compressions tests (*DC*) as indicated in Fig. 62. The considered ground conditions reflect a typical soil profile in central Stuttgart which is characterized by weak weathered Keuper marl at the bottom; see Fig. 60. The three upper soil layers represent sandy-silty soil layers whereas the consistency classes are ranging from weak to stiff.

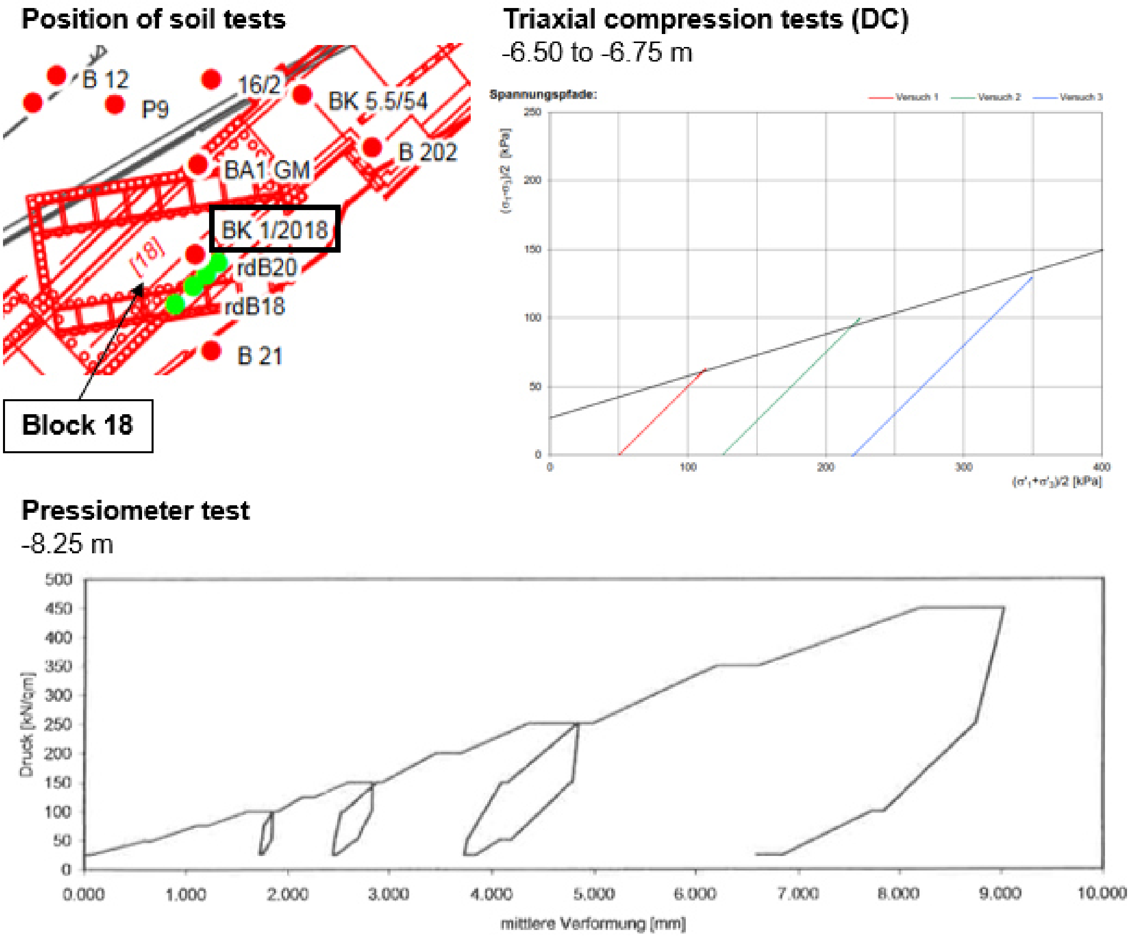

Fig. 62: Extract of the respective geotechnical report concerning conducted soil tests

Based on the respective geotechnical report of building lot “Wolframstraße”, the *HSS* model (Benz, 2007) is used to model all soil units, apart from the Backfill material, which is modelled with the linear elastic-perfectly plastic Mohr-Coulomb model (*MC*). In the present case, *HSS*-parameters describing the Small Strain Stiffness (i.e. $\gamma_{0.7}$, G_0) were not available at the time of analysis. Hence, $\gamma_{0.7}$ is determined based on the recommendations given by Vucetic and Dobry (1991); see Fig. 63. Moreover, a conservative approach is used to determine G_0; see Equ. 20. The soil parameters adopted in the 3D *FEA* are summarized in Tab. 15

$$G_0 = \frac{3 \cdot E_{ur,ref}}{2 \cdot (1 + \nu'_{ur})} \tag{20}$$

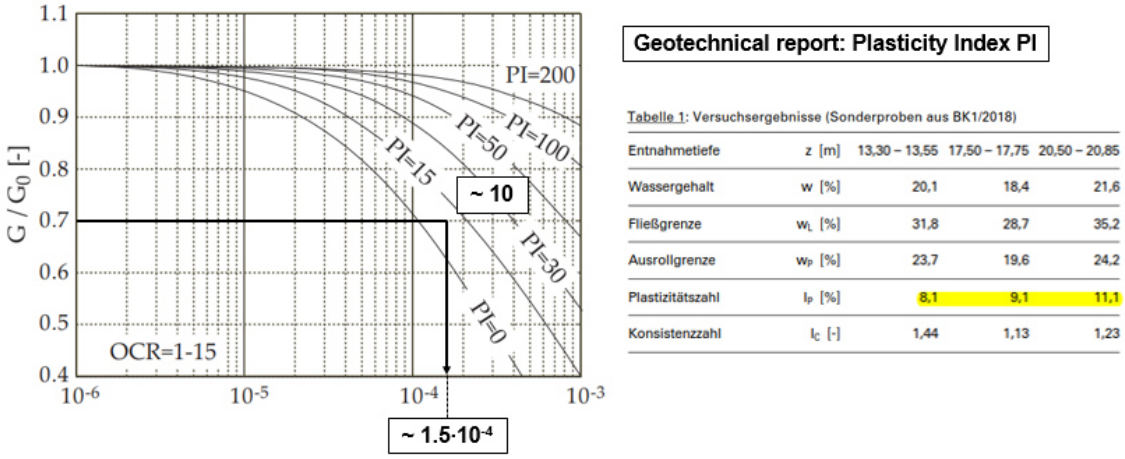

Geotechnical report: Plasticity Index PI

Tabelle 1: Versuchsergebnisse (Sonderproben aus BK1/2018)

Entnahmetiefe	z [m]	13,30 – 13,55	17,50 – 17,75	20,50 – 20,85
Wassergehalt	w [%]	20,1	18,4	21,6
Fließgrenze	w_L [%]	31,8	28,7	35,2
Ausrollgrenze	w_P [%]	23,7	19,6	24,2
Plastizitätszahl	I_P [%]	8,1	9,1	11,1
Konsistenzzahl	I_C [-]	1,44	1,13	1,23

Fig. 63: Influence of plasticity index on stiffness reduction (Vucetic and Dobry, 1991)

Tab. 15: Construction lot “Wolframstraße” - soil parameters

Symbol	Backfill material 1	Backfill material 2	Stillwater sediments	Fließerde	Keuper marl	Unit
z	0 – (-1.5)	(-1.5) – (-6)	(-6) – (-11)	(-11) – (-17)	< -17	m
Model	MC	MC	HSS	HSS	HSS	-
Type	D	D	D	D	D	-
γ	19	19	19	20	21	kN/m³
γ_{sat}	19	19	19	20	21	kN/m³
E	4000	4000	-	-	-	kPa
$E_{50,ref}$	-	-	8000	8500	21000	kPa
$E_{ur,ref}$	-	-	8000	8500	21000	kPa
$E_{oed,ref}$			16000	17000	42000	kPa
φ'	25	25	17.5	25	25	°
ψ	-	-	0	0	0	°
c'	25	5	10	15	20	kPa
ν'	0.35	0.35	-	-	-	-
ν'_{ur}	-	-	0.2	0.2	0.2	-
p_{ref}	-	-	100	100	100	kPa
m	-	-	0.6	0.6	0.55	-
$\gamma_{0.7}$	-	-	1.50E-04	1.50E-04	1.50E-04	-
G_0	-	-	20000	21250	52500	kPa

3.2.3 Structural elements

Both continuum as well as structural elements are used to model the construction object. The solid elements are represented by 10-noded tetrahedral elements whereas plates, (embedded) beams and anchors are defined as structural elements; an overview regarding the definition of the latter is given in Brinkgreve et al. (2018a). In the following, the application of those elements to the present large-scale model is documented. To this end, the model generation of four spatial zones is described in more detail, namely: Block 18, Block 20, adjacent surface load and HWS; see Fig. 64. The respective modelling parameters are listed in Appendix C.

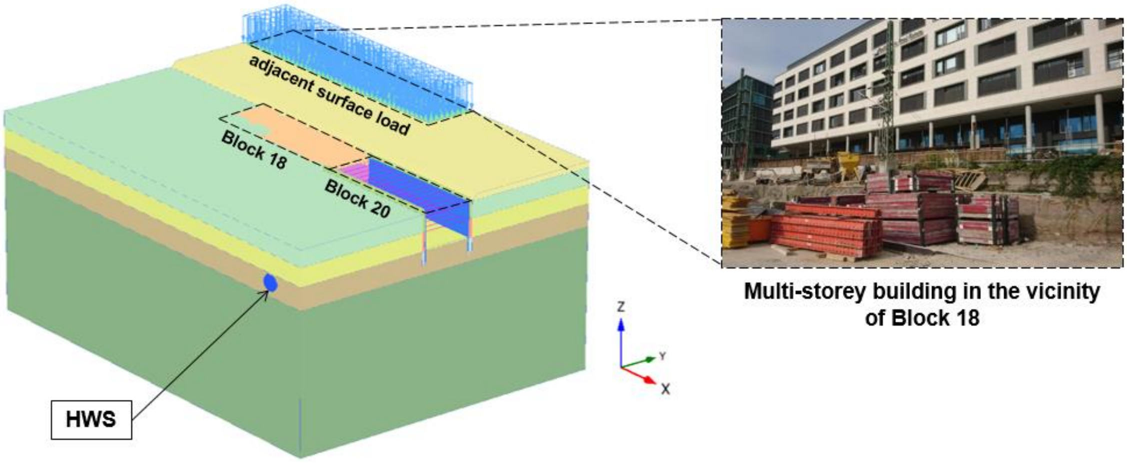

Fig. 64: Overview of entire 3D model and photo of the considered multi-storey building

- **Adjacent surface load**

During preliminary studies, it was found that the multi-storey building, which is situated north of Block 18, has an effect on the stress distribution in the vicinity of the HWS; see Fig. 64. This is taken into consideration by modelling the raft foundation explicitly and subjecting the foundation with the corresponding loads from above; see Fig. 65. Approaching the adjacent building as five-storeyed, the surface load is determined in accordance with the recommendations given in FSV (2013):

$$p_{surface} = 5\,[storey] \cdot 15\,\left[\frac{kPa}{storey}\right] = 75\,kPa \qquad (21)$$

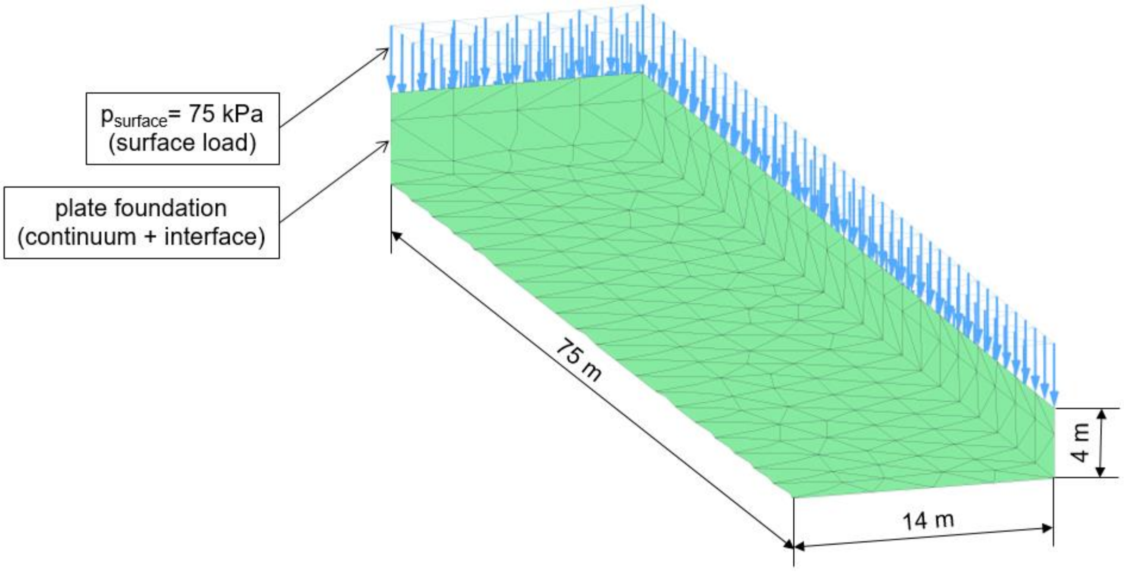
$p_{surface}$= 75 kPa (surface load)
plate foundation (continuum + interface)
75 m
4 m
14 m

Fig. 65: FE model taking into account the surface load of the adjacent building

- **Drainage tunnel modelling (HWS)**

Chapter 2 presents a comprehensive preliminary study which provides a better understanding of the structural behaviour of the considered drainage tunnel. Consequently, the derived modelling recommendations are applied to the large-scale model. To this end, the HWS is modelled as circular plate element with anisotropic material behaviour taking into account the joint-induced anisotropy of the lining structure; see Tab. 14. Fig. 66 provides details regarding the HWS geometry in the 3D model.

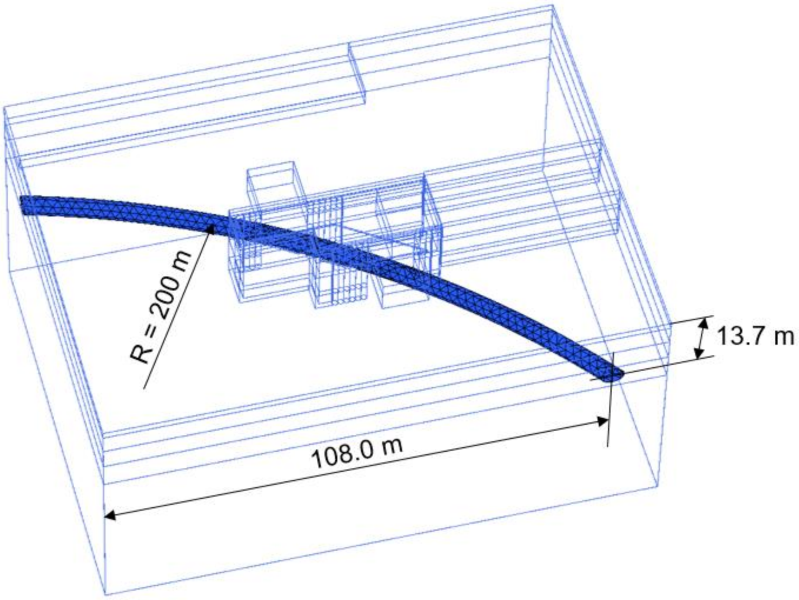
R = 200 m
13.7 m
108.0 m

Fig. 66: Specifications regarding the HWS geometry

- **Block 20 modelling**

The excavation work performed below the roof slab of Block 18 is proceeded by the construction of Block 20; see Fig. 67. In order to assess its contribution to the overall structural behaviour of the existing drainage tunnel, the construction process of Block 20 is considered in additional calculation phases.

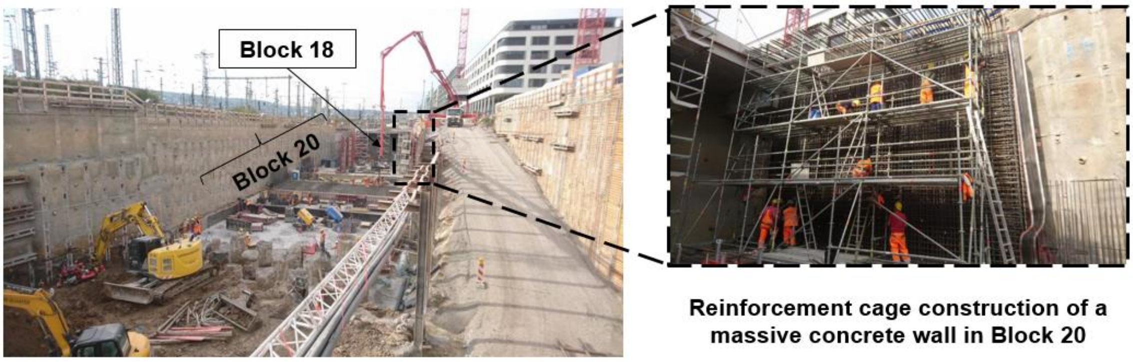
Block 18
Block 20
Reinforcement cage construction of a massive concrete wall in Block 20

Fig. 67: On-site photos replicating the construction process of Block 20

The excavation of Block 20 is supported by a combination of structural elements as explained in Fig. 68. Plate elements representing both massive concrete walls as well as the tunnel stop wall provide the lateral support of Block 20. In addition, struts and walings are modelled as one dimensional beam elements in order to ensure the stability of the side walls. On the contrary, the embedded pile formulation presented by Tschuchnigg (2013) is used to provide the support of the tunnel stop wall which poses the boundary surface between Block 18 and Block 20.

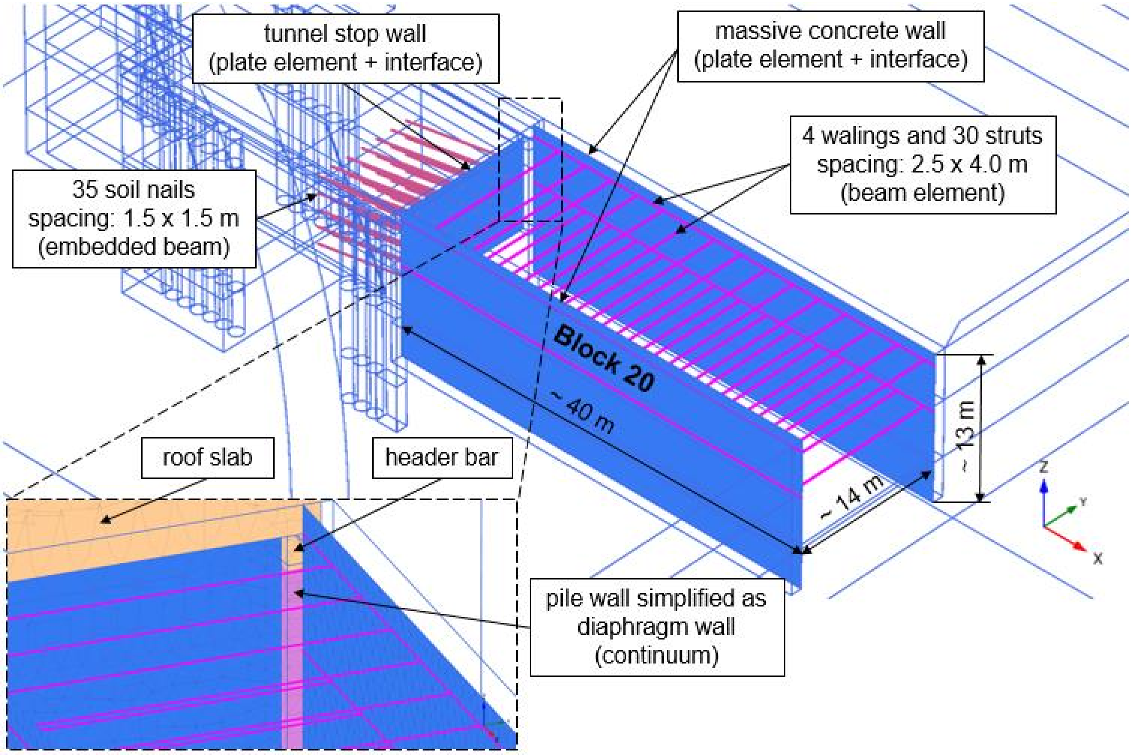
tunnel stop wall
(plate element + interface)
massive concrete wall
(plate element + interface)
4 walings and 30 struts
spacing: 2.5 x 4.0 m
(beam element)
35 soil nails
spacing: 1.5 x 1.5 m
(embedded beam)
Block 20
~ 40 m
~ 13 m
~ 14 m
z
y
x
roof slab
header bar
pile wall simplified as
diaphragm wall
(continuum)

Fig. 68: FE model considering the construction of Block 20

- **Block 18 modelling**

The cut-and-cover construction (i.e. pile wall, header bar, roof slab) is modelled by means of continuum elements. In the vicinity of the drainage tunnel, the piles forming the pile wall are explicitly modelled which allows for a detailed analysis of the stress (re)distribution in this area; see Fig. 69. However, the residual pile wall length is considered as continuous diaphragm wall with smeared stiffness properties in order to simplify the 3D model. In areas where the drainage tunnel crosses the pile wall axis, the pile wall is replaced by lateral shotcrete walls which are supported by soil nails. Vertical micropiles are modelled as embedded beam elements; in this way, the results of respective pull-out tests can be taken into consideration. During the final excavation step, plate elements as well as ground anchors (i.e. embedded beam + node-to-node anchor) are used to replicate both the construction of the reinforced invert as well as the installation of pre-stressed anchors. The modelling approach is summarized in Fig. 69 and Fig. 70.

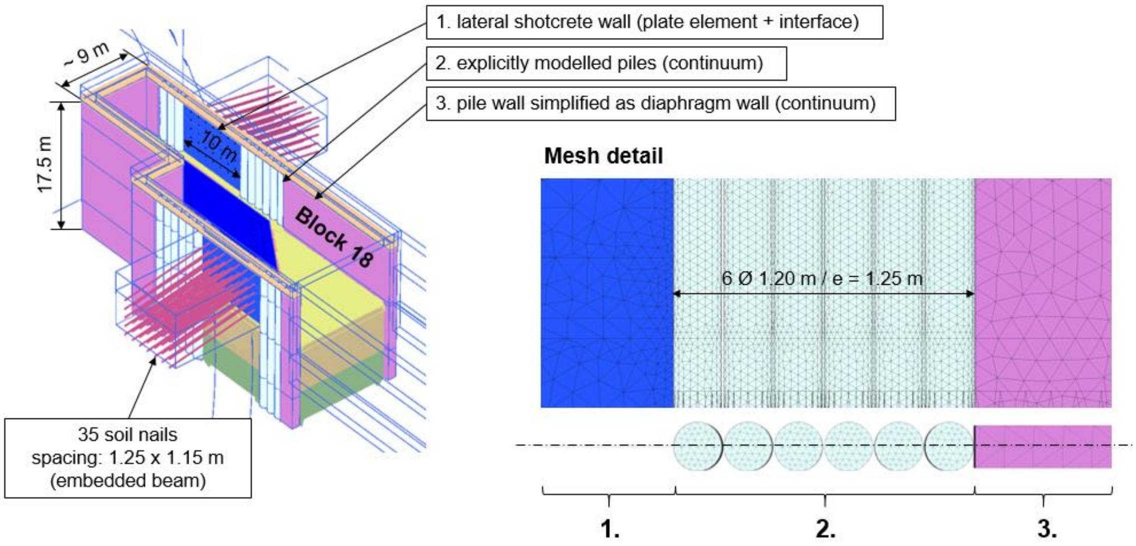
1. lateral shotcrete wall (plate element + interface)
2. explicitly modelled piles (continuum)
3. pile wall simplified as diaphragm wall (continuum)
~ 9 m
17.5 m
10 m
Block 18
35 soil nails
spacing: 1.25 x 1.15 m
(embedded beam)
Mesh detail
6 Ø 1.20 m / e = 1.25 m
1.
2.
3.

Fig. 69: FE model considering the construction of Block 18 (top-view)

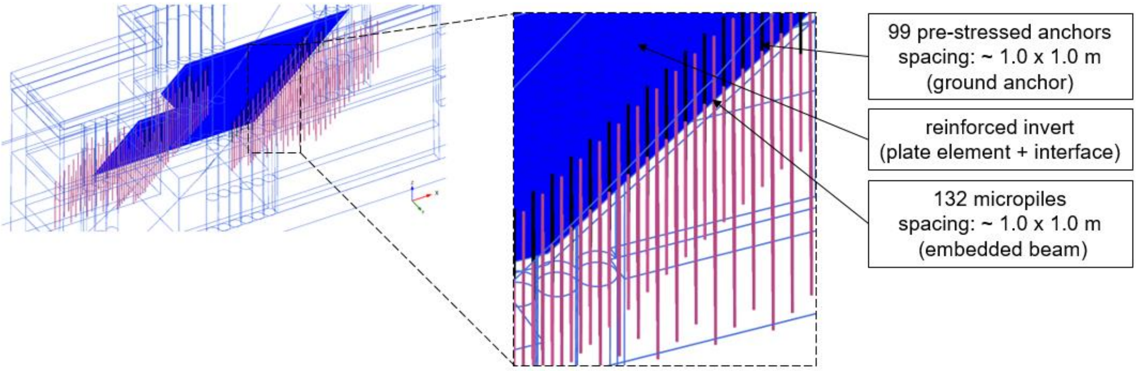
99 pre-stressed anchors
spacing: ~ 1.0 x 1.0 m
(ground anchor)
reinforced invert
(plate element + interface)
132 micropiles
spacing: ~ 1.0 x 1.0 m
(embedded beam)

Fig. 70: FE model considering the construction of Block 18 (bottom-view)

3.2.4 Calculation phase sequence

The calculation phase sequence is set in accordance with the respective schedule of construction lot “Wolframstraße” as shown in Fig. 73. The on-site excavation work was mainly performed under dry conditions without the use of additional drainage measures; hence, GW lowering is not considered. All presented results refer to drained conditions. The pre-relaxation prior to the lining installation of the existing drainage tunnel is modelled with the so called load reduction method (*β*-method) (EANG, 2014). In a first order approximation, the load reduction factor *β* is therefore determined following a calibration procedure as briefly explained in Fig. 71 (Fillibeck, 2012).

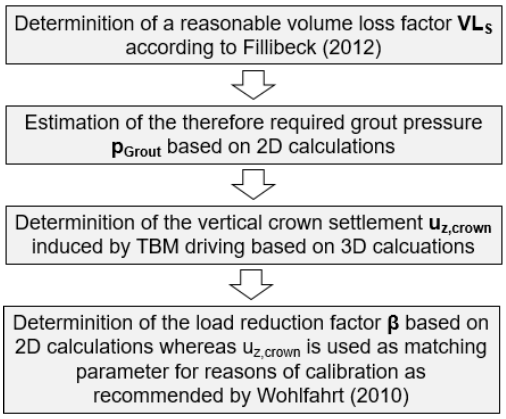

Determinition of a reasonable volume loss factor $\mathbf{VL_S}$ according to Fillibeck (2012)

Estimation of the therefore required grout pressure $\mathbf{p_{Grout}}$ based on 2D calculations

Determinition of the vertical crown settlement $\mathbf{u_{z,crown}}$ induced by TBM driving based on 3D calcuations

Determinition of the load reduction factor **β** based on 2D calculations whereas $u_{z,crown}$ is used as matching parameter for reasons of calibration as recommended by Wohlfahrt (2010)

Fig. 71: Calibration process performed in order to determine the load reduction factor

In the course of the construction site set-up, the ground level is adapted as explained in Fig. 72. Consequently, this construction phase is taken into consideration by means of a slope excavation in order to account for the resulting stress redistribution. Since the preparation of the working plane marks the beginning of the most recent construction work in the vicinity of Block 18, both displacements and small strains are reset at the beginning of this phase. The latter assumes that the soil units have regained the Small Strain Stiffness behaviour at the time the present construction starts.

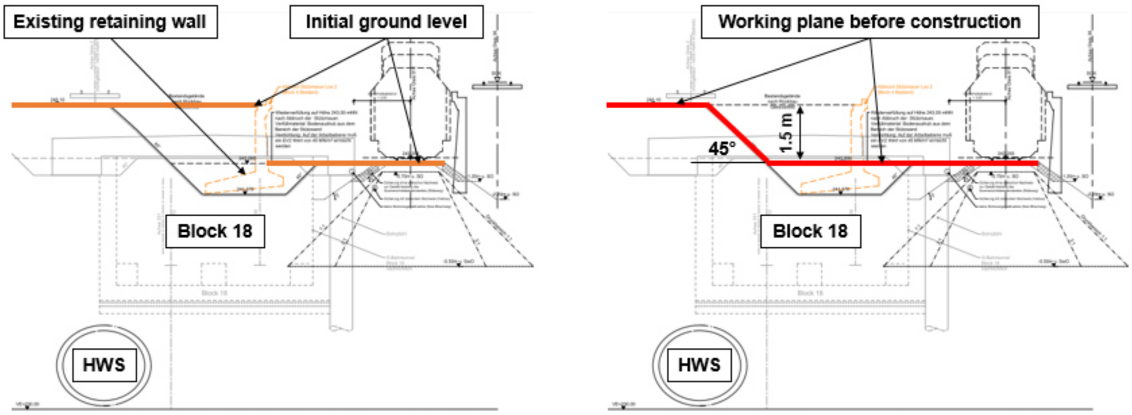

Fig. 72: Preparation of the working plane

Excessive rainfalls occurring during the construction process have to be considered since they might flaw the integrity of the tunnel leading to the flooding of the construction site. In the final phase, the HWS is therefore loaded by hydraulic radial surface pressure developing around its circumference whereas the radial pressure is 50 kPa at the top of the tunnel and increases with 10 kPa/m depth. In this way, the structural consequences of this load case is analysed in more detail.

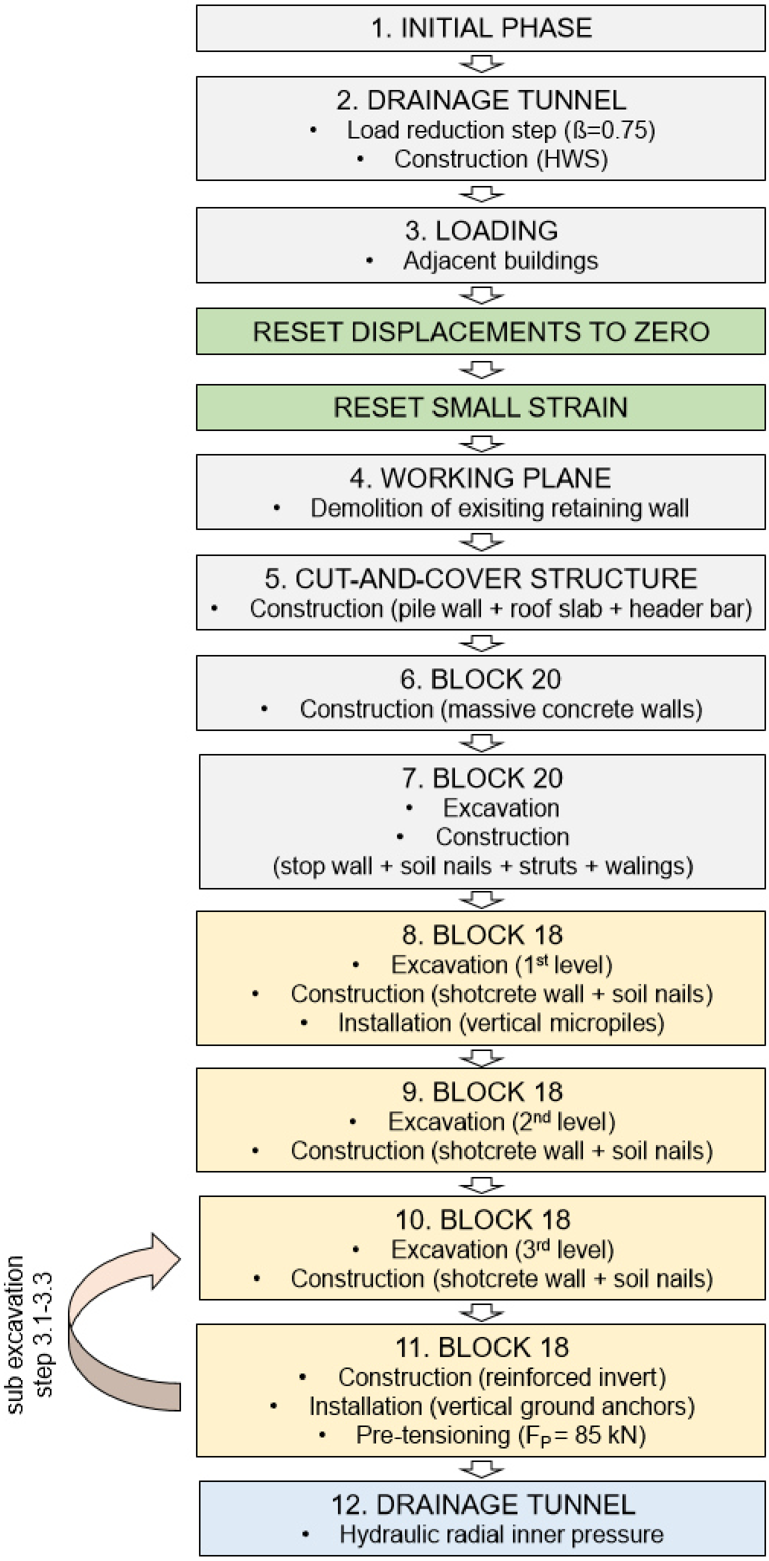
1. INITIAL PHASE
2. DRAINAGE TUNNEL
• Load reduction step (ß=0.75)
• Construction (HWS)
3. LOADING
• Adjacent buildings
RESET DISPLACEMENTS TO ZERO
RESET SMALL STRAIN
4. WORKING PLANE
• Demolition of exisiting retaining wall
5. CUT-AND-COVER STRUCTURE
• Construction (pile wall + roof slab + header bar)
6. BLOCK 20
• Construction (massive concrete walls)
7. BLOCK 20
• Excavation
• Construction
(stop wall + soil nails + struts + walings)
8. BLOCK 18
• Excavation (1st level)
• Construction (shotcrete wall + soil nails)
• Installation (vertical micropiles)
9. BLOCK 18
• Excavation (2nd level)
• Construction (shotcrete wall + soil nails)
10. BLOCK 18
• Excavation (3rd level)
• Construction (shotcrete wall + soil nails)
sub excavation step 3.1-3.3
11. BLOCK 18
• Construction (reinforced invert)
• Installation (vertical ground anchors)
• Pre-tensioning (FP = 85 kN)
12. DRAINAGE TUNNEL
• Hydraulic radial inner pressure

Fig. 73: Calculation phase sequence

3.2.5 Simplification of complex structures

Due to both, the complexity of the FE model as well as software-related limitations regarding input options, several assumptions are made as subsequently described:

- **Drainage tunnel**

The drainage tunnel axis is considered as horizontal in the FE model while the longitudinal gradient of the respective HWS section is approximately 0.9 %. In addition, the position of the tunnel axis is approximated as circular segment as shown in Fig. 66. The pre-relaxation of the soil is modelled by means of a load reduction step (β-method). However, since there was no reliable information regarding the construction of the tunnel (e.g. grout pressure, advance rate), the load reduction factor β is determined following a simplified calibration procedure.

- **Cut-and-cover construction**

Explicit modelling of the pile wall is restricted to the area next to the drainage tunnel as shown in Fig. 69. The residual length is approximated as diaphragm wall with smeared properties of the pile wall (i.e. bending stiffness EI and normal stiffness EA). The actual length of the respective piles varies from 15.5 m to 22.8 m as indicated in Fig. 55. However, the length of both pile wall sections is considered as constant with an overall length of 17.5 m which corresponds to the actual length of the piles next to the drainage tunnel.

- **Inclination of soil layers**

Since there is no reliable information about the spatial conditions with respect to the soil profile, the gradient of surfaces representing boundary soil layers is assumed as horizontal.

- **Block 20**

At the construction site, ground anchors (i.e. subjected to tension) were used to provide support to the massive concrete walls of Block 20. Since there was no reliable information about the structural properties of the installed ground anchors at the time of analysis, a combination of struts and walings was used in the 3D model to ensure stability; the respective structural properties are listed in Appendix C and comply with common standards. It is noted that those construction objects are not of high relevance in the present 3D *FEA*.

- **Construction process of retaining structures**

In the present *FEA*, both the cut-and-cover construction as well as the massive concrete walls of Block 20 are modelled based on the assumption that the structures are “wished-in-place”. The latter implies that the construction process itself does not cause any movements or changes in lateral earth or water pressures.

3.3 Results and discussion

This chapter presents the results of the conducted 3D *FEA*. Unless otherwise specified, the results refer to phase 11 after completion of the entire construction work (no hydraulic radial inner pressure active). Firstly, the sensitivity of the model to several input parameters such as the model depth and the subdivision of the final excavation phase is analysed; see section 3.3.1. Secondly, the cross-sectional response of the tunnel lining to different calculation phases is studied in more detail; see section 3.3.2. Thirdly, deviations regarding the longitudinal structural behaviour of the HWS as a consequence of different modelling approaches are investigated; see section 3.3.3. The final section of this chapter briefly concerns the stress state of the pile wall as well as structural consequences of heavy rainfalls leading to hydraulic radial inner pressure on the intrados (i.e. the interior curve of the tunnel lining) of the HWS; see section 3.3.4.

Several calculations varying in model depth, load reduction factor *β*, calculation phase sequence and drainage tunnel modelling were performed; unless otherwise stated, all presented results correspond to the colour-coded cells in Tab. 16. The results are mainly obtained from the cross-sections as shown in Fig. 74. Both, used abbreviations in the diagrams and sign conventions with respect to internal forces, are consistent with the explanations of section 3.3.

Tab. 16: Modelling options considered in large-scale model

Variable	**Options**		**Reference**
Model depth z	55	30	3.2.1.
Load reduction factor β	0.75	0.25	3.2.4.
Calculation phase sequence of final excavation step (3rd level)	sequential excavation	all-in-once excavation	3.1.
HWS modelling approach	anisotropic	isotropic	Appendix D

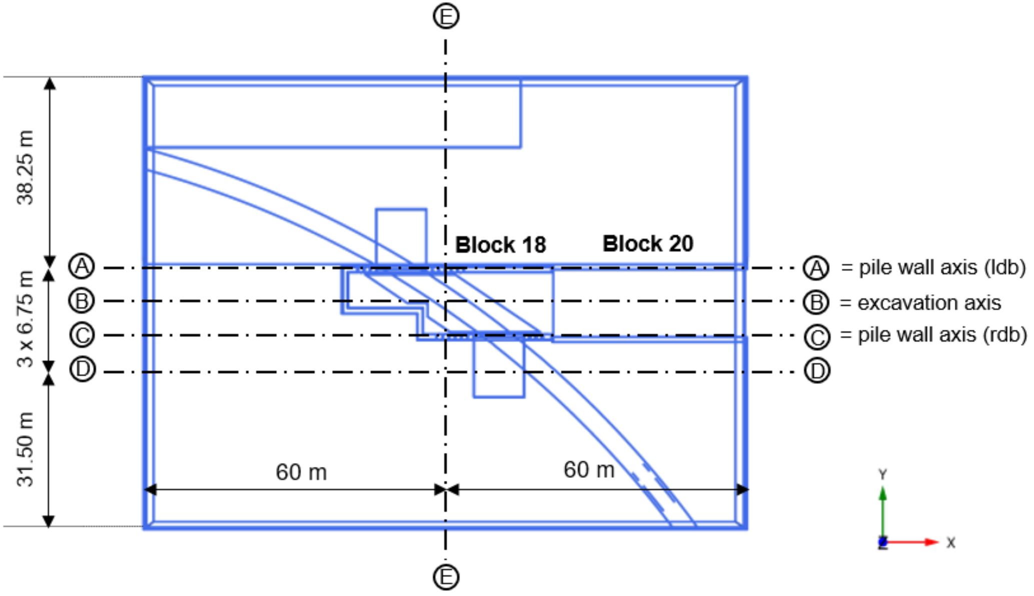

Fig. 74: Results are evaluated in the defined sections

3.3.1 Sensitivity study

- **Model depth**

Based on the recommendations given in section 2.4, great importance is attached to the selection of a reasonable model depth. In this context, it is proved that the model boundaries have an insignificant effect on the calculation output for given a given model depth. In other words, the model depth is chosen such that the output is almost not affected by increasing values. With respect to the required computation time, optimized boundary conditions are an important aspect.

Fig. 75 gives the vertical crown displacement curve of the entire HWS obtained with two different model depths (i.e. z_{Model} = 30 or 55 m). In the present case, the results clearly demonstrate that an increase in model depth leads to significant deviations regarding the calculation output: The max. vertical crown displacement occurring in the vicinity of the excavation axis is around 14 % higher when z equals 55 m. It is therefore recommended to analyse the distribution of the Small Strain Stiffness ratio (state parameter 8: G/G_{ur}) to get a better understanding of the effect of the model depth on the calculation output.

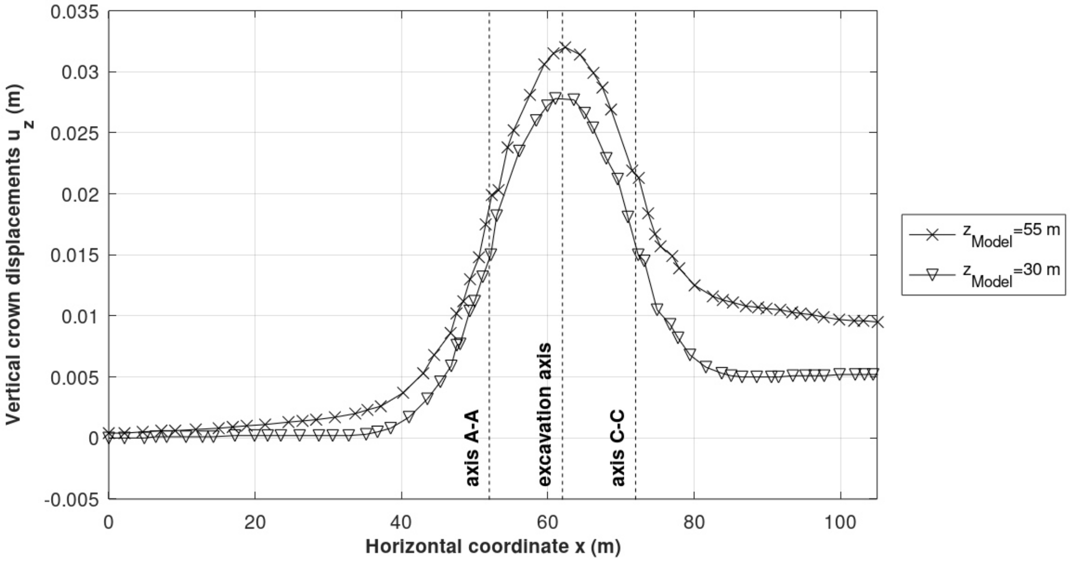

Fig. 75: Vertical crown displacement curve of the tunnel lining obtained with different model depths z_{Model}

Fig. 76 compares the results obtained with two different model depths (i.e. z_{Model} = 30 or 55 m) at three cross sections. Regions of large strains (G/G_{ur} ~ 1) stretching down to the bottom model boundary deduce that the model depth has to be increased. If the model depth is set to 30 m, regions of “large” strains adjoin the bottom model boundary indicating an inadequate model depth. On the contrary, if the model depth is increased to z_{Model} = 55 m, regions of large strains are restricted to the areas above the bottom model boundary. Hence, it is concluded that the FE model yields reliable results if z_{Model} = 55 m; the latter value is therefore applied in the large-scale model for further analyses which complies with an acceptable calculation time frame as well.

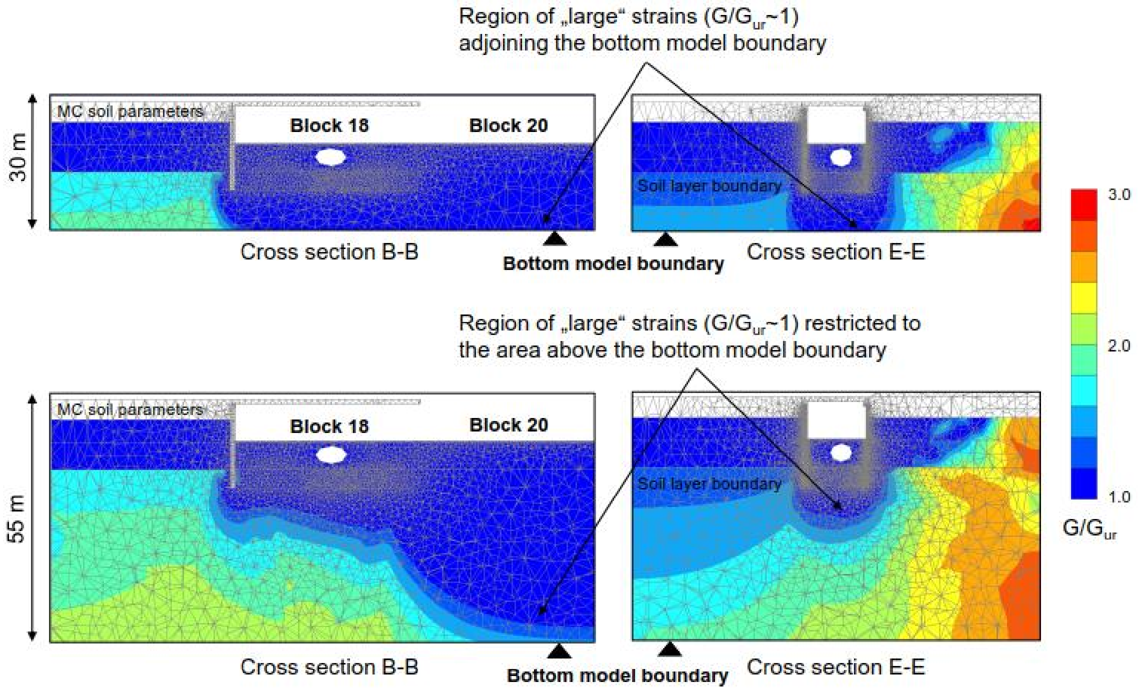

Fig. 76: Distribution of Small Strain Stiffness ratio as a function of model depth (vertical cross-sections)

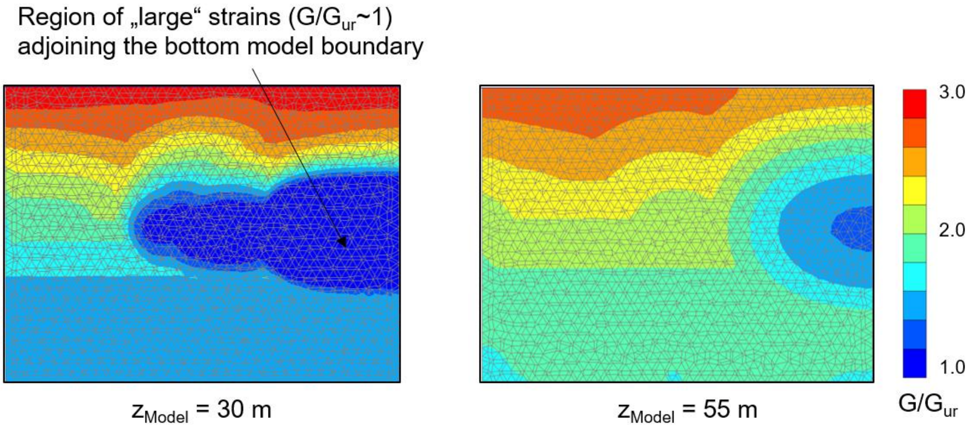

Fig. 77: Distribution of Small Strain Stiffness ratio as a function of model depth (horizontal cross-sections 1 m above bottom model boundary)

- **Load reduction factor β**

In the present case, the pre-relaxation prior to the lining installation is taken into consideration by means of a load reduction step (β-method). However, no reliable information regarding the construction process of the tunnel was available at the time of analysis; hence, the determination of the β-value is more or less left to conjecture. To highlight the range of uncertainty arising from the lack of relevant information, a limit boundary value analysis is performed in which β is either set to 0.25 or 0.75. Fig. 78 indicates a strong dependency of the vertical crown displacements on the load reduction factor β in the area of Block 18; the max. vertical crown displacements occurring in the vicinity of the excavation axis are around 33 % higher for $\beta = 0.75$. In a first order approximation, a simplified calibration procedure was established to determine the load reduction factor; see Fig. 71. As a result, the load reduction factor was set to 0.75 for further analysis.

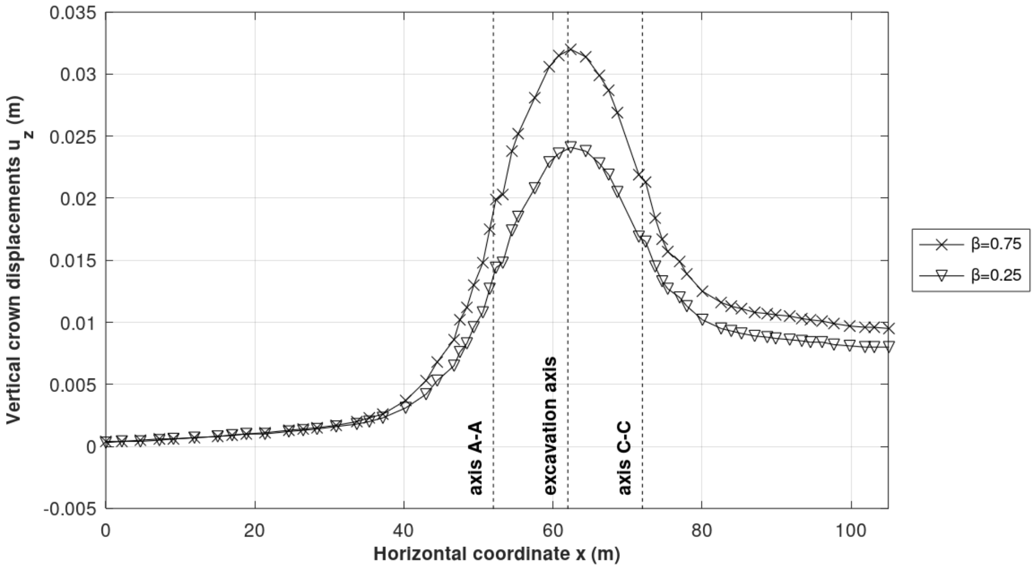

Fig. 78: Vertical crown displacement curve of the tunnel lining obtained with different load reduction factors *β*

- **Simulation of final excavation sequence**

During the set-up phase of the FE model, questions arose concerning the necessity of the subdivision of the final excavation step 3 as shown in Fig. 79 and Fig. 80 (i.e. 3.1, 3.2, 3.3). This section therefore examines deviations resulting from two calculation phase sequence modelling approaches:

- All-in-once excavation: The entire construction effort (i.e. excavation, installation of lateral shotcrete walls as well as soil nail support, installation of reinforced invert, pre-tensioning of ground anchors) is summarized in one calculation phase.
- Sequential excavation: The finale excavation step is subdivided in six calculation phases which allows for a more detailed analysis of the stress (re)distribution occurring within Block 18; see Fig. 80.

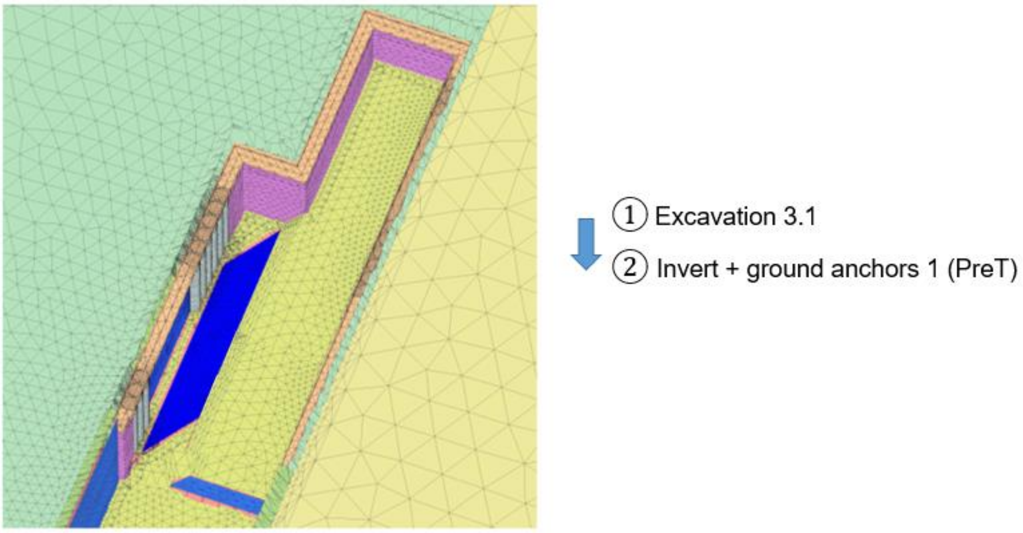

Fig. 79: The final excavation step is subdivided in six phases (Part A)

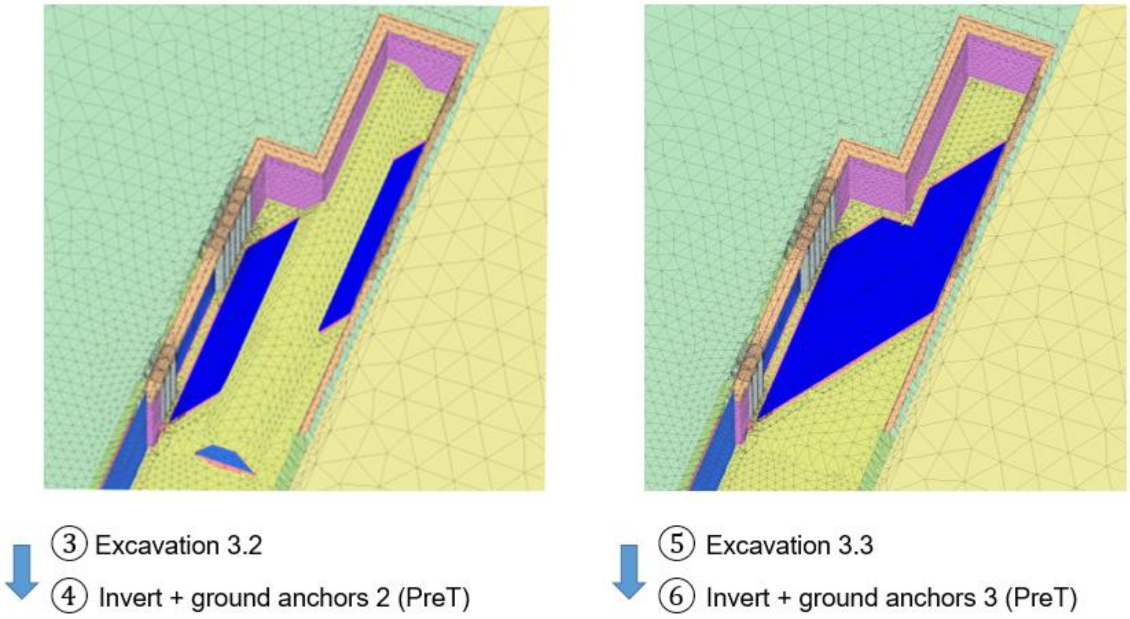
③ Excavation 3.2
④ Invert + ground anchors 2 (PreT)
⑤ Excavation 3.3
⑥ Invert + ground anchors 3 (PreT)

Fig. 80: The final excavation step is subdivided in six phases (Part B)[7]

Fig. 81 presents the contours of vertical soil displacements at the position of the final excavation base (z = -10.6 m). While the sequential excavation option predicts higher max. vertical displacements (~ 3 mm) in the area of Block 18, the all-in-once excavation option yields slightly higher values in the vicinity of the HWS axis which is attributed to different stress paths developing in the soil. Considering max. vertical crown displacements occurring in the vicinity of the excavation axis, the sequential excavation option gives a marginally higher value (~ 3 %); see Fig. 82. Nevertheless, the observed deviations appear negligible for practical applications; since the subdivision of the final excavation phase leads to a significant increase in both, modelling effort and calculation time, it seems therefore reasonable to accelerate the *FEA* using the all-in-once concept. However, in the present *FEA* the “all-in-once” approach is used.

---

[7] In order to give the reader a better overview, the roof slab as well as soil volumes / structural objects outside Block 18 are partially hided.

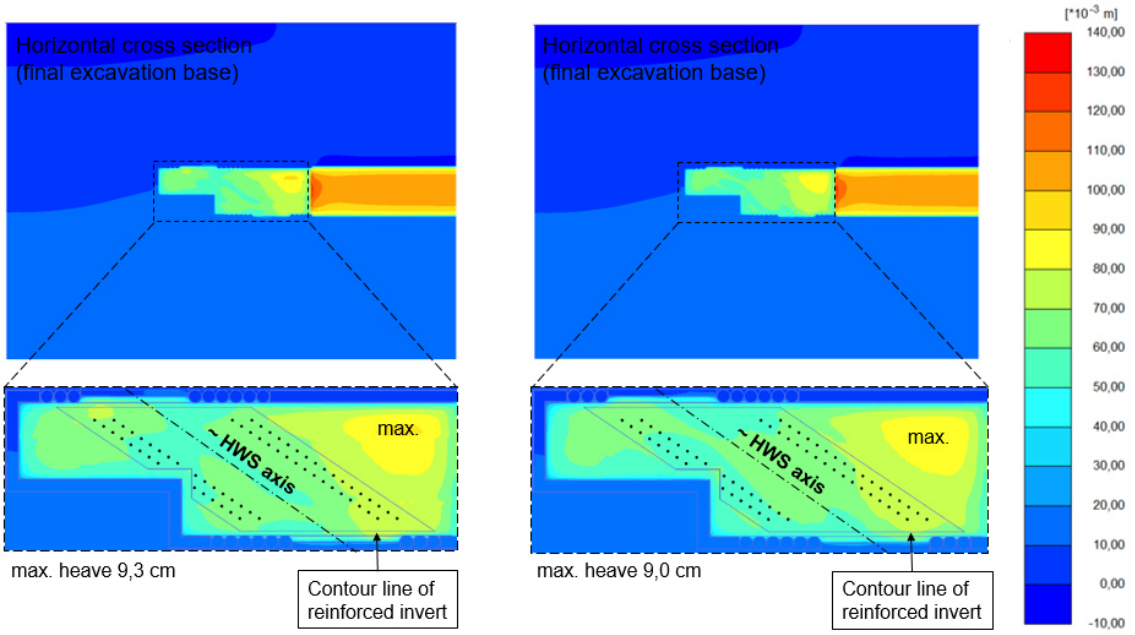
Horizontal cross section
(final excavation base)
Horizontal cross section
(final excavation base)
max.
~ HWS axis
max.
~ HWS axis
max. heave 9,3 cm
Contour line of reinforced invert
max. heave 9,0 cm
Contour line of reinforced invert
[*10⁻³ m]
140,00
130,00
120,00
110,00
100,00
90,00
80,00
70,00
60,00
50,00
40,00
30,00
20,00
10,00
0,00
-10,00

Fig. 81: Contours of vertical displacements u_z (left: sequential excavation; right: all-in-once excavation)

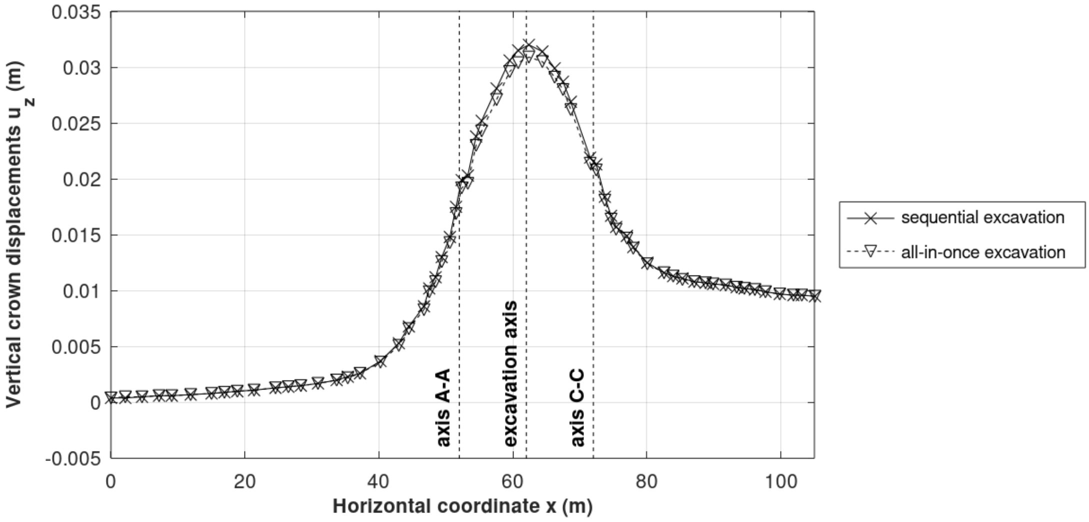

Fig. 82: Vertical crown displacement curve of the tunnel lining obtained with different calculation phase sequences during excavation step 3

3.3.2 Cross-sectional structural behaviour (HWS)

- **Crown displacements**

This paragraph provides a comparison of the heave of the tunnel crown occurring throughout the construction process simulation at different cross-sections. To this end, Fig. 83 shows both, the vertical phase displacements Pu_z as well as the total deformations u_z, related to the considered calculation phases. A closer inspection of the plotted data leads to the following findings:

- The max. total displacements ($u_{z,B\text{-}B}$: 36 mm, $u_{z,C\text{-}C}$: 24 mm) are observed after the final excavation sequence (i.e. Exc 3.3). The soil heave is more pronounced at the position of the excavation axis in cross-section B-B.

- The excavation of the working plane, which is referred to as "Dem" in the diagram, significantly affects the vertical crown displacements ($Pu_{z,B\text{-}B}$: 4 mm, $Pu_{z,C\text{-}C}$: 7 mm). This has to be taken into consideration when comparing the obtained results of the present 3D *FEA* with the results of on-site measurements. In other words, the recording begin of the on-site measurements has to comply with the time where displacements are reset to zero in order to provide consistency between the results.
- In both cross-sections, the max. phase displacements (heave) are induced by the first excavation phase below the roof slab of Block 18 ($Pu_{z,B\text{-}B}$: 15 mm, $Pu_{z,C\text{-}C}$: 9 mm). However, it has to be noted that the excavation height of the subsequent excavation steps is lower (Exc 1: 5.0 m > Exc 3.1-3: 4.1 m > Exc 2: 1.5 m).
- The pre-tension phases (PreT: construction of the reinforced invert, pre-tensioning of the respective ground anchors) minor affect the crown displacements (Pu_z < 0.8 mm). However, they solely aim to prevent the tunnel lining from being subjected to tension during the final calculation phase.

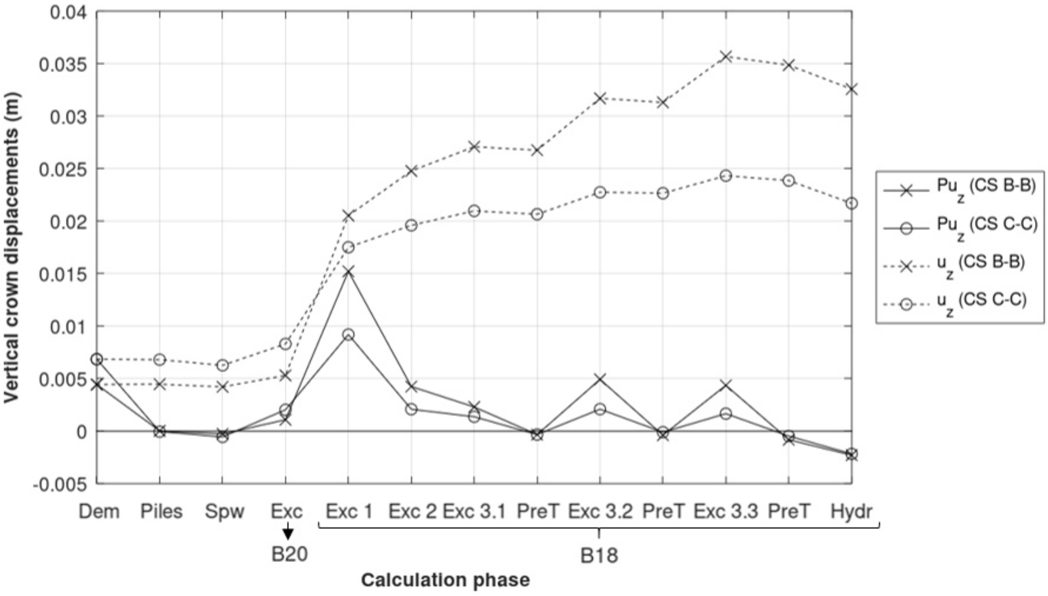

Fig. 83: Development of vertical crown displacements at different cross-sections

- **Bending moments**

Fig. 84 compares the bending moments obtained at different positions in different phases of the *FEA*. The plot clearly demonstrates that the bending moments obtained at different positions of the lining significantly vary during the construction phase. At each lining position, the final excavation phase (i.e. Exc 3.3) gives the max. absolute value of the bending moment. However, a change in sign of the bending moment is observed after the first excavation sequence (i.e. Exc 1) in Block 18 which is attributed to arising unloading conditions in Block 18.

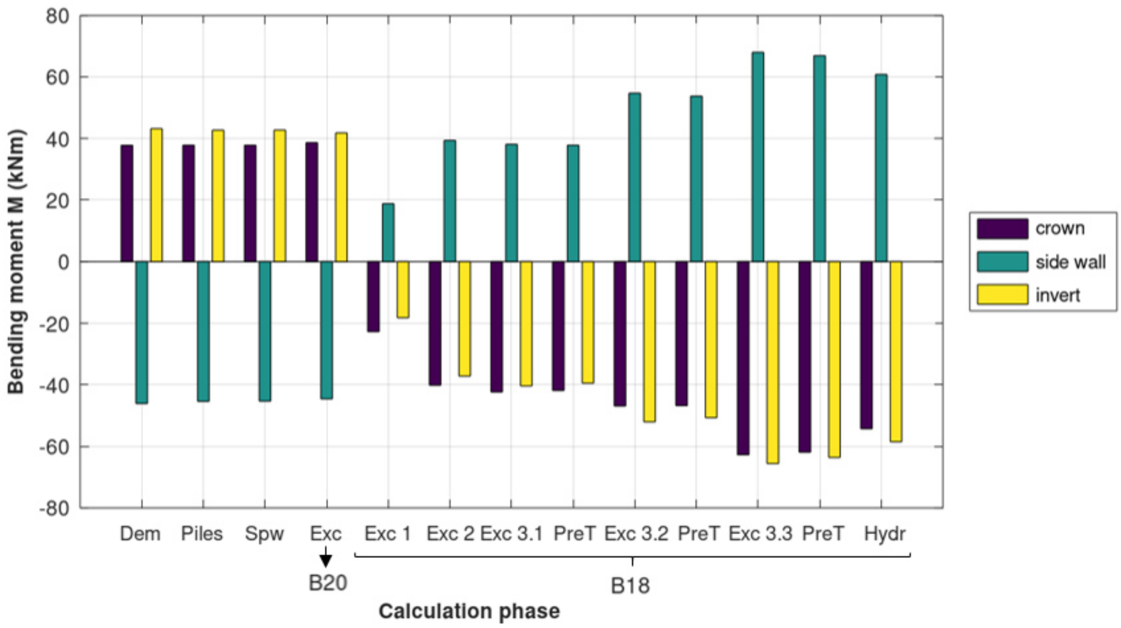

Fig. 84: Development of cross-sectional bending moment at different positions of the lining (Cross-section B-B)

- **Position of max. lining displacements**

Fig. 85 shows the position (θ) and the value of the max. absolute lining displacements after completion of the entire construction work (no hydraulic radial inner pressure active). The position of the reference points is measured clockwise by an angle θ. An angle θ=0° represents a reference point being positioned at the tunnel crown, while an angle θ=180° represents a reference point being positioned at the tunnel invert. The results refer to the viewing direction as defined in Fig. 86.

The max. lining displacements are observed in the vicinity of the excavation axis at the position of the tunnel crown (B-B: 3.2 mm, E-E: 3.1 mm). On the contrary, the max. lining displacements at the position of both pile wall axis (A-A: 2.2 mm, C-C: 2.6 mm) are observed at a closer distance to the side wall. As indicated in Fig. 6, cross-section E-E, which is located outside the excavation area, gives the max. lining displacement at a position close to the side wall (E-E: 1.4 mm). In the present case, the results confirm that the connection line of max. lining displacement points is spiral-shaped.

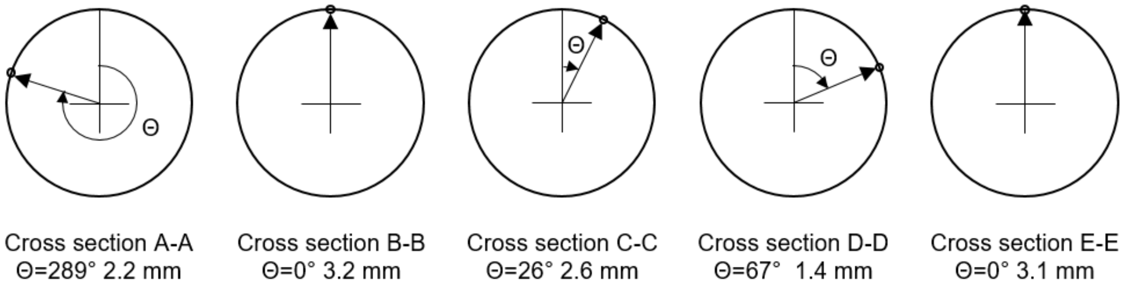

Fig. 85: Location and magnitude of max. lining displacement[8]

---

[8] The evaluated lining cross-sections have an elliptical shape. However, for reasons of simplicity, the elliptical shape is herein illustrated as circle.

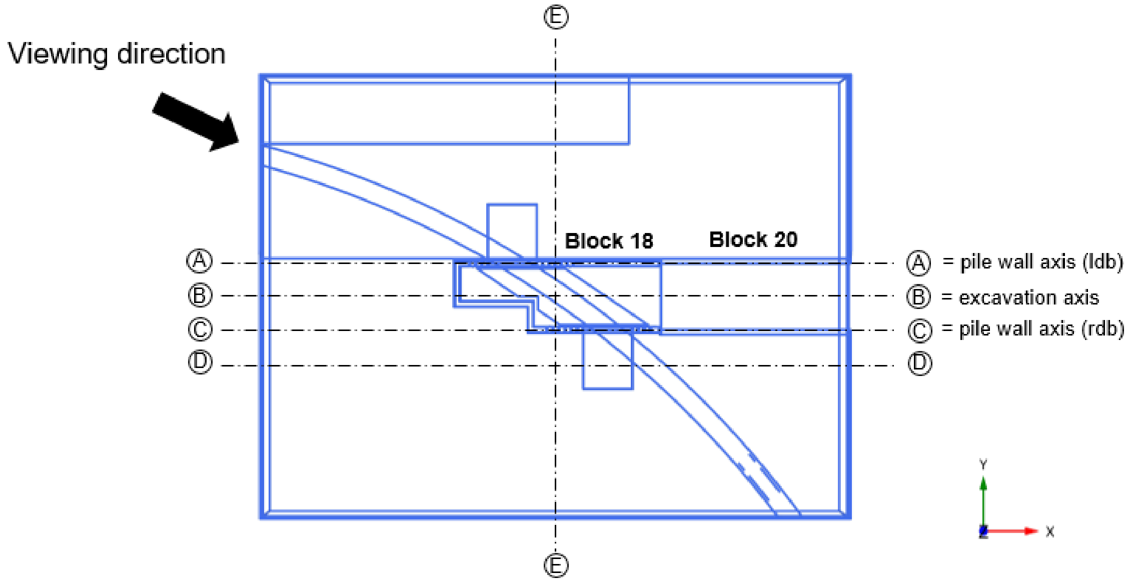

Fig. 86: The results are obtained considering the marked viewing direction.

3.3.3 Longitudinal structural behaviour (HWS)

Based on the recommendations given in chapter 2, the joint-induced anisotropy of the lining structure is considered by means of an indirect-joint model with anisotropic material behaviour. As a consequence, both the axial bending stiffness as well as the axial normal stiffness are reduced compared to the isotropic option; see section 2.4. However, the drainage tunnel was considered as isotropic in an additional analysis in order to examine to which extent the observed tendencies of section 2.3.2 apply for the large-scale model.

Fig. 87 shows the vertical crown displacement curve of the HWS which is either modelled as anisotropic or isotropic. As expected, the heave of the tunnel crown decreases as the distance between the excavation axis and the tunnel increases. The anisotropic model develops slightly higher max. crown displacements at the position of the excavation axis compared to the isotropic model (~ 0.5 mm) which generally corresponds to the observed tendency in section 2.3.2; however, the deviation appears negligible (~ 2 %). On the contrary, significant differences between both models are observed in the areas adjacent to the pile wall axes (i.e. A-A, C-C).

It can be further concluded from the results that both crown displacement curves yield almost the same displacements at the model boundaries; while the position of the tunnel crown remains almost the same at the model boundary where x = 0, significant heave is observed at the other end of the lining. The latter is mainly attributed to the preparation of the working plane which is considered as ground excavation; see Fig. 72.

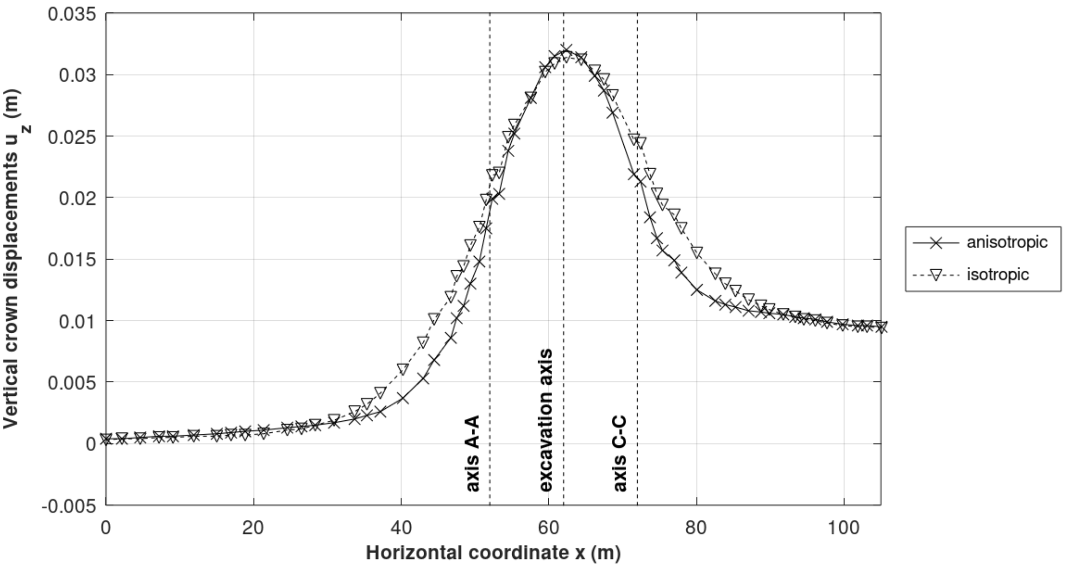

Fig. 87: Vertical crown displacement curve obtained with different material properties of the tunnel lining

Fig. 88 gives the deflection angle *δ* at different positions along the tunnel crown which is herein defined as follows:

$$tan\,\delta = \frac{\Delta u_{z,crown}}{d} \tag{22}$$

In the equation, Δu_z marks the difference of vertical displacements obtained between adjacent nodes at the tunnel crown whereas d is the initial horizontal distance between the respective nodes.

In both cases, the max. deflection angles are observed near the pile wall axes (i.e. A-A, C-C) which roughly represent the position of the inflection points (i.e. points where *δ* shows peak values and the bending curvature becomes 0). In addition, $\delta = 0$ ° in the vicinity of the excavation axis which indicates the position of the critical (min.) bending curvature. As a consequence, joint opening might become critical in cross-section B-B; see section 2.1.2.

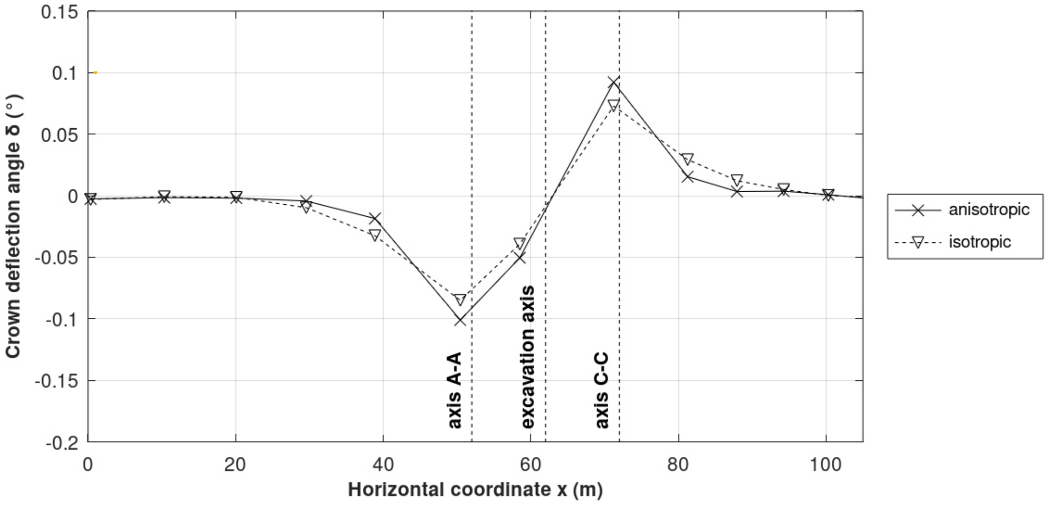

Fig. 88: Crown deflection angle *δ* obtained with different material properties of the tunnel lining

3.3.4 Overall structural behaviour

- **Ground heave**

The previous sections clearly show that the effect on the lining structure due to above-ground excavation is longitudinal heave. This section extends the observation area to the entire 3D model. Fig. 89 therefore presents the contours of vertical soil displacements in three cross-section.

Ground heave is particularly pronounced at the excavation base of Block 20 whereas the max. vertical soil displacement is observed at the lower edge of the tunnel stop wall. As previously discussed in the previous section 3.3.3, ground heave outside the side wall (*rdb*) is mainly attributed to the excavation performed in phase 4 (i.e. working plane set-up). Although displacements are set to zero after phase 3 (i.e. foundation loading), the presented contour lines show vertical settlements in the foundation area; the latter indicates that the present construction work contributes to settlements in the region of the adjacent building illustrated in Fig. 64. While the excavation marginally influences the soil near the pile wall (*ldb,* Block 18), settlements are obtained in the soil behind the massive concrete wall (*ldb*, Block 20). The latter is expected due to the fact that the pile wall is extended to a greater depth (z = -19.5 m) compared to the massive concrete wall (z = -14.5 m); as a consequence, the pile wall restricts vertical excavation-orientated displacements more effectively.

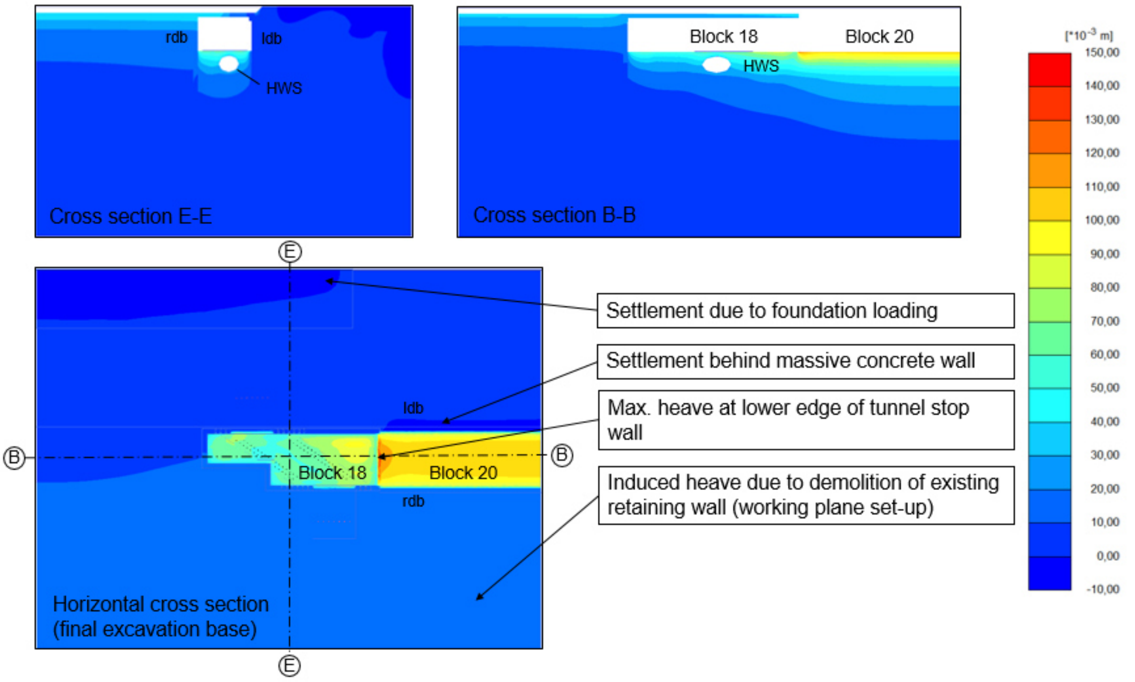

Fig. 89: Contours of vertical displacements u_z (overall behaviour)

In this context, Fig. 90 replicates vertical displacements of both the soil and the lining occurring at different phases in Block 18. It becomes quite clear from the plot that the final lining displacements are mainly governed by the first excavation phase below the roof slab in Block 18; the latter corresponds to the findings of section 3.3.2.

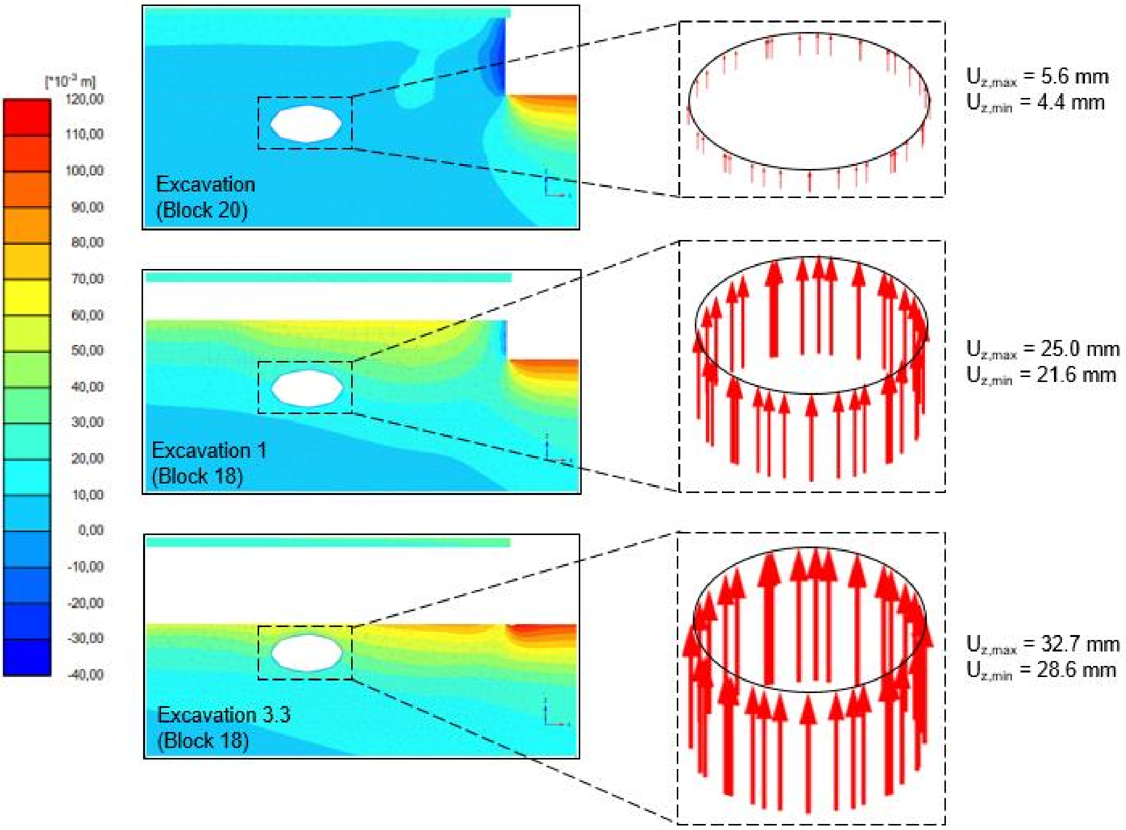

Fig. 90: Vertical displacements u_z at different stages in Block 18 (cross-section B-B)

- **Radial lining pressure due to excessive rainfalls**

An additional calculation phase is defined in order to analyse the structural consequences of hydraulic radial inner pressure caused by excessive rainfalls; see section 2.2.1. The main response of the tunnel crown due to hydraulic pressure is longitudinal settlement as shown in Fig. 91 whereas the obtained vertical crown phase displacements distribute almost equally along the tunnel axis (~ 2.3 mm). Differences arising between both models are assumed as negligible.

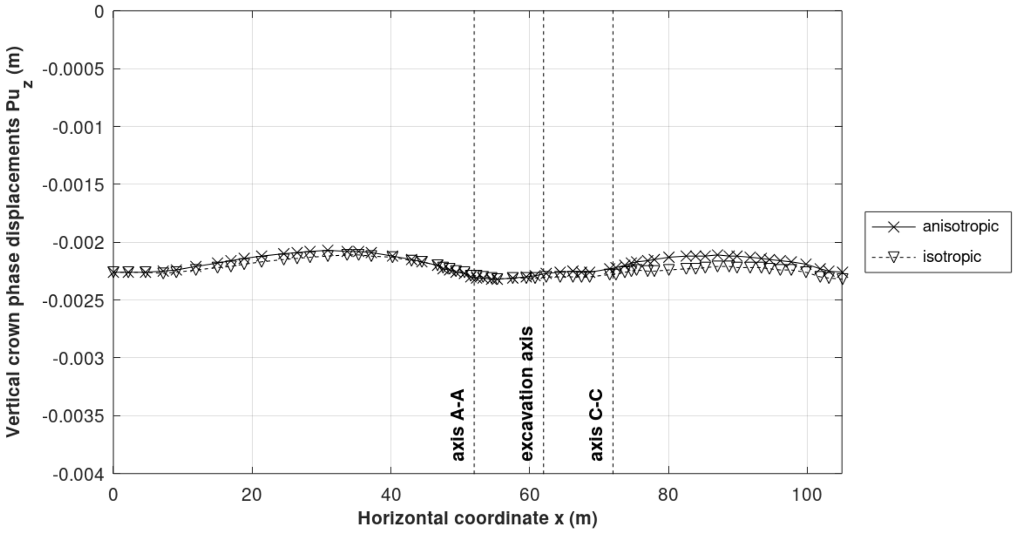

Fig. 91: Vertical crown phase displacements (Phase 12) obtained with different material properties of the tunnel lining

Fig. 92 gives the vertical phase displacements obtained at the position of cross-section E-E. The plot clearly shows that the settlements are not restricted to the tunnel crown as the entire lining cross-section and the adjacent structures are shifted downwards as a consequence of unequal hydraulic radial pressures. In contrast, the soil mass located at a certain distance to the tunnel moves upwards.

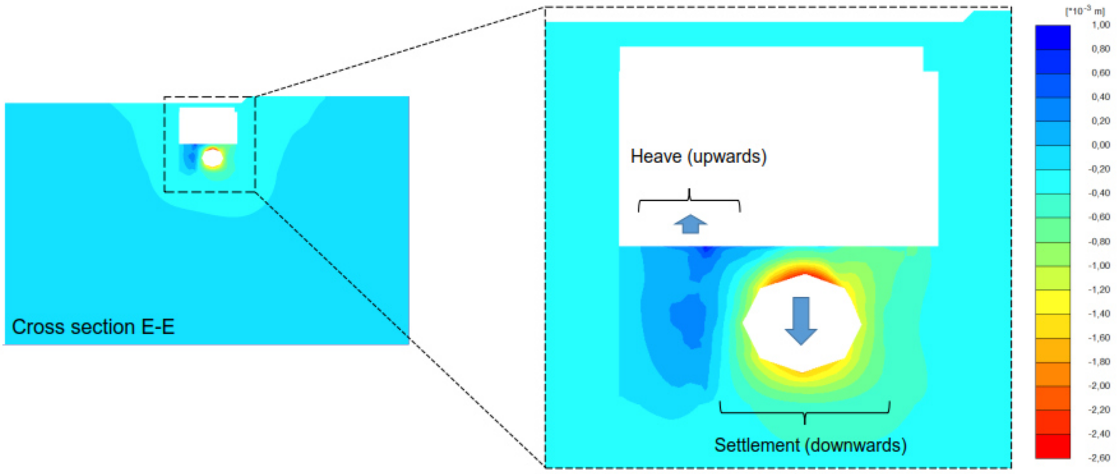

Fig. 92: Contours of vertical phase displacements Pu_z (hydraulic pressure)

- **Structural forces**

The "structural forces in volume feature" (Brinkgreve et al., 2018a) is used to obtain structural forces of selected piles (C 30/37) forming the pile wall; the input parameters of the explicitly modelled piles are listed in Tab. 30. This feature allows for a first order approximation of structural forces developing in structures that are composed of continuum elements. Considering the cross-sectional properties of the piles (i.e. cross-sectional area *A*, second moment of area *I*), the obtained structural forces are then used to calculate the max. normal stresses of selected piles. It is mentioned that the presented max. normal stresses are well in agreement with the corresponding principal stress σ_1 output observed at the respective positions. However, since the examined piles are modelled as linear-elastic, the calculated stress values only represent a conservative approximation of the present stress state.

Fig. 93 lists the max. bending moment M_{max}, the axial force *N* at the position of M_{max} (z) as well as the calculated max. compressive / tensile stress of Piles 1-4. In the present case, both the max. absolute value of the compressive stress $\sigma_{c,max}$ as well as the max. tensile stress $\sigma_{ct,max}$ are obtained in pile 3. It is also inferred from the results that the position of the max. bending moment varies significantly amongst both excavation axes (*ldb, rdb*). Since $\sigma_{ct,max}$ = 8.1 MPa is substantially higher than the actual mean tensile strength f_{ctm} = 2.9 MPa, it is assumed that the present bending moment M_{max} exceeds the cracking moment M_{cr}. The latter indicates that the critical cross-section is in the cracked state as explained in Fig. 94.

structural forces in piles (Ø 1.20m, A=1.13m², I=0.10m⁴)

Pile Nr.	M_{max} [kNm]	N [kN]	$\lvert\sigma_{c,max}\rvert$ [MPa]	$\sigma_{ct,max}$ [MPa]	z [m]
1	1430	-730	9.1	7.8	-3.5
2	1340	-630	8.5	7.3	-3.5
3	1460	-600	9.1	8.1	-9.3
4	1280	-800	8.3	6.8	-9.1

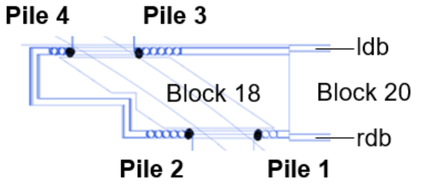

Fig. 93: Structural analysis of selected piles

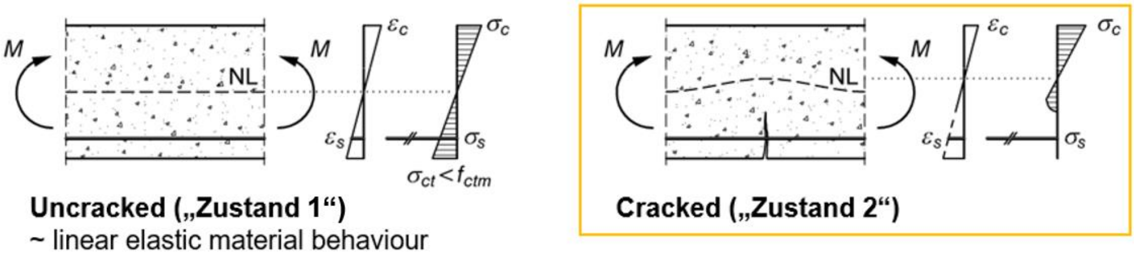

Uncracked („Zustand 1")
~ linear elastic material behaviour

Cracked („Zustand 2")

Fig. 94: Stress-strain relationship at different stress states (reinforced concrete beam) (Nguyen, 2018)

3.4 Conclusions and further perspective

3D finite element analyses were performed in order to analyse the effect of the construction of building lot “Wolframstraße” on the existing drainage tunnel HWS. The performance of the latter was of main concern since the damage of the lining was considered to result in the flooding of the construction site. Based on the preliminary study presented in chapter 2, the present thesis focused on the identification of modelling aspects that determine the structural response of the HWS. Moreover, the development of both crown displacements and bending moments during the different construction phases was studied in more detail. The 3D model was further used to reflect on the structural forces occurring in the pile wall as well as on the lining deformations induced by hydraulic radial inner pressure.

- **Sensitivity analysis**

The first set of analysis is concerned with varying the model depth, the load reduction factor β and the calculation sequence of the final excavation step. In this context, the vertical crown displacements $u_{z,crown}$ of the HWS are used to assess the level of sensitivity. The max. relative difference (33 %) obtained for the herein considered limit boundary β-values indicates a strong dependency of the lining deformation behaviour on the construction process of the existing tunnel; see Tab. 17. With respect to the model depth, significant deviations are obtained as well (14 %); hence, it is recommended to use the distribution plot of the Small Strain Stiffness ratio (G/G_{ur}) as validation tool in order to determine the model depth. In contrast, subdividing the final excavation step has a minor influence on the vertical crown displacements compared to the all-in-once option. Thus, it appears reasonable to simplify the 3D model by summarizing the entire construction effort of the final excavation step in one calculation phase.

Tab. 17: Max. crown displacements obtained with different modelling approaches[9]

modelling aspect	considered options	max. $u_{z,crown}$ [cm]	rel. difference [%]
Load reduction factor β	$\beta = 0.25$	2.4	33
	$\beta = 0.75$	3.2	
Model depth z_{Model}	$z_{Model} = 30m$	2.8	14
	$z_{Model} = 55m$	3.2	
Subdivision of 3rd excavation step	all-in-once excavation	3.1	3
	sequential excavation	3.2	

---

[9] The orange-coded cells mark the standard settings of the large-scale model.

- **Structural behaviour during the construction**

Since the pre-tensioning process of the vertical ground anchors counteracts the ground heave, the max. crown displacements are observed after the final excavation phase; the crown heave is most pronounced in the region of the excavation axis. It is further inferred from the results that the max. crown phase displacements Pu_z are induced by the first excavation step below the roof slab. However, significant heave is also predicted as a consequence of the excavation during the set-up of the working plane; in the present case, it is therefore particularly important to set the “reset displacements to zero” option in accordance with the recording-begin of the measuring devices in order to ensure consistency between the measurement data and the results of the *FEA*.

The development of the bending moments is obtained at different positions of the lining (i.e. crown, side wall, invert) during the construction. The results uniformly predict a change in sign as consequence of the excavation below the roof slab. Moreover, the max. bending moments are obtained after the final excavation phase which complies to the max. crown displacements. The results clearly demonstrate that the critical calculation phase with respect to the lining design is a result of the *FEA*.

- **Deformed shape of the tunnel**

The following conclusions refer to the lining displacements obtained after completion of the construction. The heave of the tunnel crown decreases as the distance between the excavation axis and the tunnel increases. The position of the max. lining displacement varies along the tunnel axis. In the area of the excavation axis, the max. lining displacements are observed at the tunnel crown. However, the max. lining displacements at the pile wall axes occur close to the side walls. In other words, the presented results indicate that the connection line of those points (i.e. where the max. displacement is obtained) is spiral-shaped.

The tunnel lining was modelled as isotropic in an additional calculation in order to compare the crown displacement curve to the anisotropic option; in this context, the latter (approximately) accounts for the presence of joints by reducing the lining stiffness parameters as explained in chapter 2. The isotropic model yields almost the same results with respect to the max. lining displacements (~ 3.2 mm), the position of the inflection points (in the vicinity of the pile wall axes) and the position of the critical bending curvature. However, significant differences of the vertical crown displacements are observed outside the excavation area adjacent to the pile wall axes.

- **Ground heave of the overall structure**

Ground heave is most pronounced at the excavation base of Block 20 whereas the max. heave is obtained at the lower edge of the tunnel stop wall. The construction appears to contribute to the settlements of adjacent buildings. The max. phase displacement of both, the tunnel lining as well as the soil within the excavation area of Block 18, is induced by the first excavation below the roof slab; the latter complies with observations derived from the comparison of vertical crown displacements between different calculation phases.

- **Structural consequence of rainfalls**

Extensive rainfalls are taken into consideration by subjecting a hydraulic radial inner pressure on the intrados of the lining. The structural response of the lining structure is longitudinal settlement which distributes evenly along the entire tunnel length. In contrast, the adjacent soil mass shows the opposite tendency.

- **Structural forces of selected piles**

In a first order approximation, the “structural forces in volume feature” is used to obtain both, the max. bending moments M_{max} as well as the corresponding normal forces, at the position of M_{max}. The results show that the position of M_{max} considerably varies between the investigated piles. Based on the cross-section properties of the piles, the max. absolute values of the tensile/compressive stresses are calculated. The results show that the max. tensile stress exceeds the mean tensile strength ($\sigma_{ct,max} = 8.1 > f_{ctm} = 2.9$ MPa); the latter indicates that the cross-section is in the cracked state. Further studies should be conducted applying a more realistic constitutive model to describe the concrete structures more reasonably.

- **Perspective for further investigations**

The following paragraph discusses a set of aspects that should be subject to further research:

- With respect to the constitutive model, additional calculations should concentrate on the comparison of the results obtained with the HSS as well as the Generalized Hardening Soil model (*GHS*) (Brinkgreve and Laera, 2015). The latter is a user-defined soil model based on the *HSS* model, but with the enhancement that it allows to use different configurations of the stress dependent stiffness.
- Validation of the results against measured data as well as examination of differences compared to the existing 2D analyses.
- Further studies should be performed in order to investigate the distribution of structural forces developing along the tunnel axis. The latter might allow to highlight useful correlations to the spiral-formed shape of the max. lining displacement line which in turn allows for a better understanding of the structural lining behaviour in the transitional area between the excavation and the adjacent soil behind the retaining structure.

- It is recommended to model the piles by means of a more advanced constitutive model compared to the linear elastic model in order to obtain more reliable results with respect to the structural forces.
- Back-analyses of the construction process with respect to the determination of the load reduction factor β.
- For serviceability limit state considerations (water leakage due to birdsmouthing), further investigations should concentrate on both, the implementation of a direct-joint model as well as design guidelines for practical applications.
- Additional studies are required to get a better understanding of the sensitivity of the results to the considered interface and interface stiffness parameters. The same applies to the construction process of structural elements such as the pile wall installation or the excavation of the working plane.

4 References

Avgerinos, V., Potts, D.M., 2017. Numerical investigation of the effects of tunnelling on existing tunnels. Géotechnique 67, 808–822.

Bakker, K.J., 2000. Soil Retaining Structures: Development of Models for Structural Analysis (Ph.D. Thesis). TU Delft.

Bao, Z., 2015. Longitudinal Rigidity of Shield Tunnels Based on Numerical Investigation. ITA WTC 2015 Congress and 41st General Assembly.

Benz, T., 2007. Small-strain stiffness of soils and its numerical consequences (Ph.D. Thesis, Mitteilungsheft Nr. 55). University of Stuttgart.

Benz, T., Wehnert, M., 2015. Neuordnung des Bahnknotens Stuttgart – Simulation der Boden-Bauwerk-Interaktion. BAW Mitteilungen 98, 161–178.

Blom, C.B.M., 2002. Design philosophy of concrete linings for tunnels in soft soils (Ph.D. Thesis). TU Delft.

Brinkgreve, R., Kumarswamy, S., Swolfs, W., Zampich, L., Ragi Manoj, N., 2019. Plaxis 2D Reference Manual 2019 520.

Brinkgreve, R., Kumarswamy, S., Swolfs, W., Zampich, L., Ragi Manoj, N., 2018a. Plaxis 3D Reference Manual 2018 516.

Brinkgreve, R., Kumarswamy, S., Swolfs, W., Zampich, L., Ragi Manoj, N., 2018b. Plaxis 3D Material Models Manual 2018 256.

Brinkgreve, R., Laera, A., 2015. Site response and liquefaction evaluation. Plaxis Manual 42.

Caratelli, A., Meda, A., Rinaldi, Z., Giuliani-Leonardi, S., Renault, F., 2018. On the behavior of radial joints in segmental tunnel linings. Tunnelling and Underground Space Technology 71, 180–192.

Cui, Q.-L., Wu, H.-N., Xu, Y.-S., Shen, S.-L., 2015. Longitudinal deformation pattern of shield tunnel structure and analytical models: a review. Japanese Geotechnical Society Special Publication 1, 1–4.

Do, N.-A., Dias, D., Oreste, P., Djeran-Maigre, I., 2013. 2D numerical investigation of segmental tunnel lining behavior. Tunnelling and Underground Space Technology 37, 115–127.

EANG, 2014. Empfehlungen des Arbeitskreises Numerik in der Geotechnik - EANG. Ernst & Sohn, Berlin.

Erdmann, J., Duddeck, H., 1983. Statik der Tunnel in Lockergestein - Vergleich der Berechnugnsmodelle. Bauingenieur 58, 407–414.

Faltýnek, J., Pruška, J., 2019. Analytical relations for determination of rotation stiffness of the segment tunnel lining longitudinal joint. Prague Geotechnical Days 2019 and 27th Prague Geotechnical Lecture.

Fillibeck, J., 2012. Oberflächensetzungen beim Tunnelvortrieb im Lockergestein - Prognose, Messung und Beeinflussung (Ph.D. Thesis). TU München.

FSV, 2013. Offene Bauweise. RVS 9.41/4.2.9.

Fu, J., Yang, J., Klapperich, H., Wang, S., 2016. Analytical Prediction of Ground Movements due to a Nonuniform Deforming Tunnel. International Journal of Geomechanics 16, 1–14.

German Tunnelling Committee, 2013. Recommendations for the design, production and installation of segmental rings 46.

Gong, C., Ding, W., Soga, K., Mosalam, K.M., 2019. Failure mechanism of joint waterproofing in precast segmental tunnel linings. Tunnelling and Underground Space Technology 84, 334–352.

Guan, Z., Deng, T., Wang, G., Jiang, Y., 2015. Studies on the key parameters in segmental lining design. Journal of Rock Mechanics and Geotechnical Engineering 7, 674–683.

Huang, H., Huang, X., Schweiger, H.F., 2013. Influence of Deep Excavations on Nearby Existing Tunnels. International Journal of Geomechanics 13, 170–180.

Huang, X., Huang, H., Zhang, J., 2012. Flattening of jointed shield-driven tunnel induced by longitudinal differential settlements. Tunnelling and Underground Space Technology 31, 20–32.

Janßen, P., 1983. Tragverhalten von Tunnelausbauten mit Gelenktübbings (Ph.D. Thesis). TU Braunschweig.

Lee, K.M., Ge, X.W., 2001. The equivalence of a jointed shield-driven tunnel lining to a continuous ring structure. Can. Geotech. J. 38, 461–483.

Lee, K.M., Hou, X.Y., Ge, X.W., Tang, Y., 2001. An analytical solution for a jointed shield-driven tunnel lining. International Journal for Numerical and Analytical Methods in Geomechanics 25, 365–390.

Liao, S.-M., Peng, F.-L., Shen, S.-L., 2008. Analysis of shearing effect on tunnel induced by load transfer along longitudinal direction. Tunnelling and Underground Space Technology 23, 421–430.

Liu, J.H., Hou, X.Y., 1991. Shield-driven tunnels. China Railway Press 152–303.

Luttikholt, A., 2008. ULS Analysis of a Segmented Tunnel Lining. Master's Thesis, TU Delft.

Möller, S.C., 2006. Tunnel induced settlements and structural forces in linings (Ph.D. Thesis, Mitteilungsheft Nr. 54). University of Stuttgart.

Murakanu H., Koizumi A., 1978. Study of Load-bearing Capacity and Mechanics of Shield Segment Ring. Japan Society Civil Engineering.

Nguyen, V.T., 2018. Stahlbetonbau. Lecture Graz University of Technology.

ÖBV, 2009. Richtlinie Schidvortrieb.

Osgoui, R., Poli, A., Pescara, M., 2016. Critical comparison between the double-convex and flat radial joints features in segmental tunnel lining. Cappadocia: ISRM International Symposium / Eurock.

Potts, D.M., Zdravković, L., 2001. Finite element analysis in geotechnical engineering: application, 1st publication. ed. Thomas Telford, London.

Selke, P., 2013. Höhere Festigkeitslehre: Grundlagen und Anwendung. Oldenbourg Wissenschaftsverlag, München.

Summerer, W., Hosp, E., 2018. Bergmännischer Aushub in Deckelbauweise Block 18: Statische Berechnung (Statischer Bericht). Rum b. Innsbruck.

Teachavorasinskun, S., Chub-uppakarn, T., 2010. Influence of segmental joints on tunnel lining. Tunnelling and Underground Space Technology 25, 490–494.

Tschuchnigg, F., 2013. 3D finite element modelling of deep foundations employing an embedded pile formulation (Ph.D. Thesis). Graz University of Technology.

Voit, T., 2016. 3D - FEM Modelling of a Deep Excavation. Master's Thesis, Graz University of Technology.

Vucetic, M., Dobry, R., 1991. Effect of soil plasticity on cyclic response Journal of Geotechnical Engineering, 89–107.

Winselmann, D., Städing, A., Babendererde, L., Holzhäuser, J., 2000. Aktuelle Berechnungsmethoden für Tunnelauskleidungen mit Tübbingen und deren verfahrenstechnische Voraussetzungen.

Wohlfahrt, M., 2010. Studie zu Vorentlastungsfaktoren bei oberflächennahen Tunneln. Master's Thesis, Graz University of Technology.

Wood, A.M.M., 1975. The circular tunnel in elastic ground. Géotechnique 25, 115–127.

Yu, H., Cai, C., Bobet, A., Zhao, X., Yuan, Y., 2019. Analytical solution for longitudinal bending stiffness of shield tunnels. Tunnelling and Underground Space Technology 83, 27–34.

Zdravkovic, L., Potts, D.M., John, H.D.S., 2005. Modelling of a 3D excavation in finite element analysis. Géotechnique 55, 497–513.

Zhang, J.-L., Schlappal, T., Yuan, Y., Mang, H.A., Pichler, B., 2019. The influence of interfacial joints on the structural behavior of segmental tunnel rings subjected to ground pressure. Tunnelling and Underground Space Technology 84, 538–556.

5 Appendix A

- **Longitudinal bending rigidity ratio $\xi_{Cont.}$**

The analytical solution presented by Murakanu and Koizumi (1978) is used to determine the longitudinal bending rigidity ratio $\xi_{Cont.}$. The latter accounts for the ring-joint-induced reduction of the longitudinal bending rigidity of the HWS structure; see 2.2.4. The segmental lining is therefore approached as a series of concrete segments and springs as illustrated in Fig. 95, where L_S is the segmental length, L_f is the influence length of the ring joint ($L_f \leq L_S$), EI is the flexural rigidity of the concrete segment in longitudinal direction and K_θ is the rotational stiffness representing the ring joint rigidity against rotation (previously also referred to as K_{RO}).

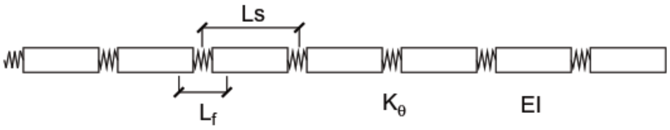

Fig. 95: Theoretical model of tunnel lining (Murakanu and Koizumi, 1978)

The total rotation angle of one tunnel unit length θ (i.e. L_S) is regarded as the sum of the rotation angle due to bending of the respective concrete segment θ_S and the rotation angle developing within the ring joint area θ_f. Assuming the structure to behave ideally elastic, one obtains θ as:

$$\theta = \theta_S + \theta_f = \frac{M \cdot L_S}{E_S \cdot I_S} + \frac{M \cdot L_f}{E_S \cdot I_S \cdot K_f} \tag{A.1}$$

$$K_f = \frac{cos^3 \psi}{cos \psi + \left(\frac{\pi}{2} + \psi\right) \cdot sin \psi} \tag{A.2}$$

$$\psi + coth \psi = \pi \cdot \left(\frac{1}{2} + \frac{n \cdot K_b}{E_S \cdot \frac{A_S}{L_f}} \right) \tag{A.3}$$

In the equations, M is the bending moment, E_S is the Young's modulus of the concrete segments, I_S is the second moment of area, K_f is the longitudinal bending stiffness coefficient of the ring joint, ψ is the rotational angle describing the location of the neutral axis in Fig. 96, n is the number of longitudinal bolts per cross-section, K_b is the translational stiffness of the bolts at the joint and A_S is the cross-sectional area of the concrete lining. Assuming that the equivalent indirect-joint model (i.e. ring joint is not explicitly modelled) develops the same rotation angle θ for a given bending moment M, Equation (20) can be further expressed as a function of the equivalent longitudinal bending stiffness $(EI)_{eq}$:

$$\theta = \frac{M \cdot L_S}{E_S \cdot I_S} + \frac{M \cdot L_f}{E_S \cdot I_S \cdot K_f} = \frac{M \cdot L_S}{(EI)_{eq}} = \frac{M \cdot L_S}{E_S \cdot I_S \cdot \xi_{Cont.}} \tag{A.4}$$

Eliminating E_S, I_S and M on both sides of the equation, the equivalent longitudinal bending stiffness ratio ξ_{Cont} can finally be written in the following expression:

$$\xi_{Cont.} = \frac{K_f \cdot L_S}{K_f \cdot L_S + L_f} \tag{A.5}$$

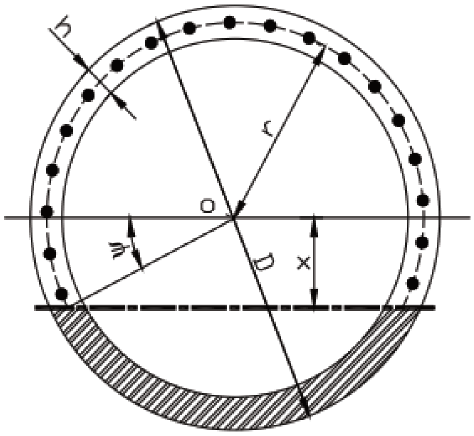

Fig. 96: Definition of cross-sectional parameters (Murakanu and Koizumi, 1978)

6 Appendix B

- **Longitudinal joint modelling – Rotational rigidity K_{RO} – Unloading conditions**

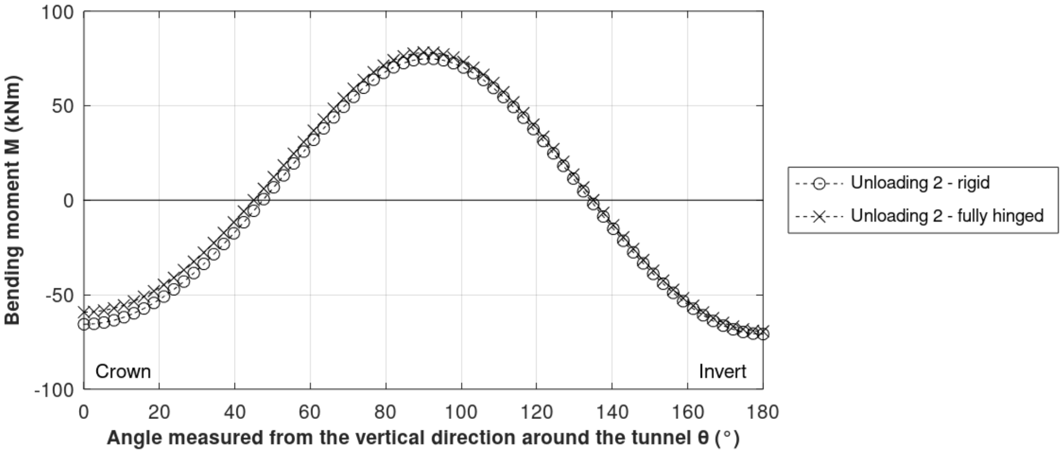

Fig. 97: Bending moment diagram considering different longitudinal joint configurations (unloading conditions)

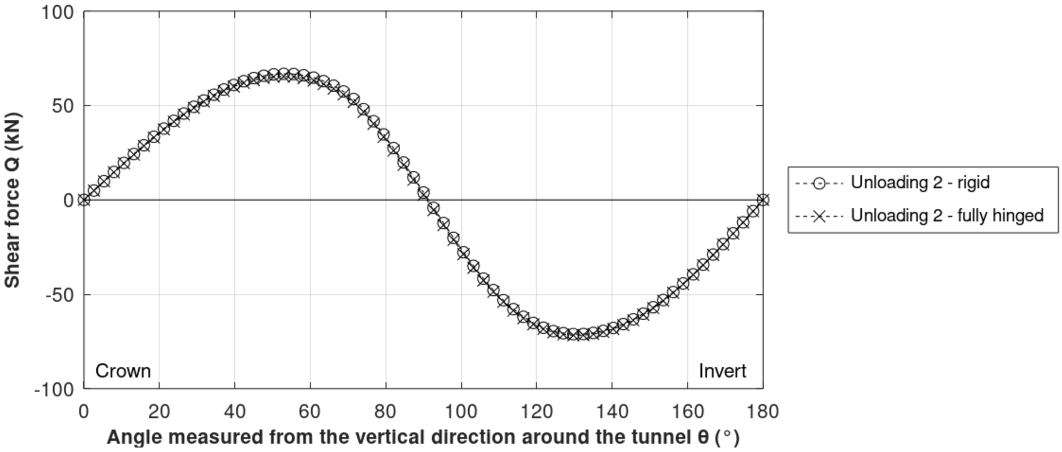

Fig. 98: Shear force diagram considering different longitudinal joint configurations (unloading conditions)

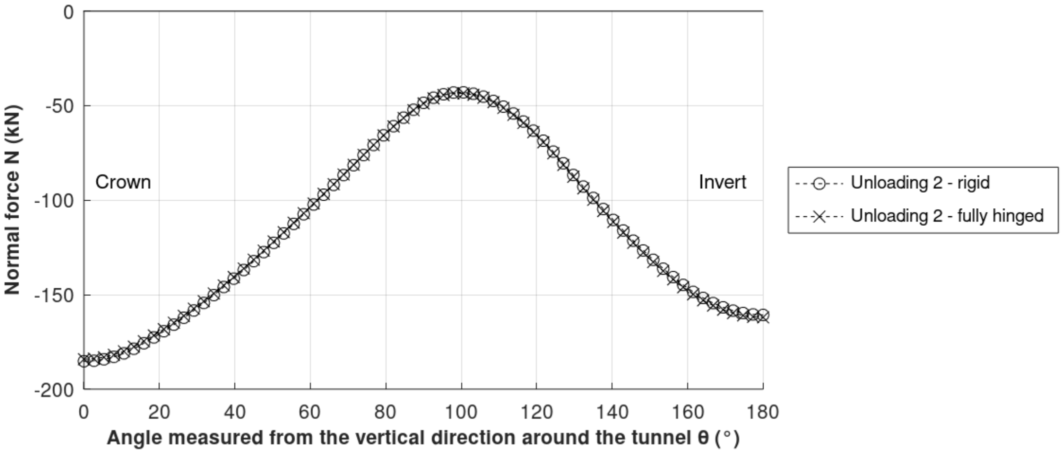

Fig. 99: Normal force diagram considering different longitudinal joint configurations (unloading conditions)

Tab. 18: Absolute lining displacements

absolute tunnel displacements [cm]				
loading type	rotational rigidity of longitudinal joint	crown, u_Y	invert, u_Y	side wall, u_X
Unloading 1	rigid	1.9	5.2	±1.6
	fully hinged	1.9	5.2	±1.6
Unloading 2	rigid	2.8	6.4	±2.0
	fully hinged	2.8	6.4	±2.0

- **Joint-induced shear stiffness reduction – Max. bending moment M_{max}**

Tab. 19: Relationship between shear stiffness coefficient ζ_{Joint} and max. cross-sectional bending moment M_{max} of tunnel lining (loading, *HSS*)

longitudinal position	max. cross-sectional bending moment	shear stiffness coefficient ζ_{Joint}						isotropic
		0.01	0.05	0.10	0.30	0.50	1.00	
middle cross-section	M_{max} (kNm/m)	195.17	185.63	183.15	180.74	179.93	178.90	192.67
	M_{max} (normalized)	1.00	0.95	0.94	0.93	0.92	0.92	

Tab. 20: Relationship between shear stiffness coefficient ζ_{Joint} and max. cross-sectional bending moment M of tunnel lining (unloading, *HSS*)

longitudinal position	max. cross-sectional bending moment	shear stiffness coefficient ζ_{Joint}						isotropic
		0.01	0.05	0.10	0.30	0.50	1.00	
middle cross-section	M_{max} (kNm/m)	97.05	105.61	107.68	109.85	110.44	111.26	142.21
	M_{max} (normalized)	0.87	0.95	0.97	0.99	0.99	1.00	

7 Appendix C

- **Material parameters used in large-scale model - Adjacent surface load**

Tab. 21: Raft foundation parameters

parameter		value	unit
structural element		continuum	
material type		elastic	
type		non-porous	
unit weight	γ	19.0	kN/m^3
Young's modulus	E	29.0	GPa
Poisson's ratio	ν'	0.2	-
shear modulus	G	12.1	GPa
interface reduction factor	R_{inter}	1.0	-

- **Material parameters used in large-scale model – Drainage tunnel (HWS)**

Tab. 22: HWS lining parameters (isotropic material behaviour)

parameter		value	unit
structural element		plate	
material type		elastic	
thickness	d	0.28	m
unit weight	γ	25.0	kN/m^3
Young's modulus	E	34.0	GPa
Poisson's ratio	ν'	0.2	-
shear modulus	G	14.2	GPa
interface reduction factor	R_{inter}	1.0	-

Tab. 23: HWS lining parameters (anisotropic material behaviour)

parameter		value	unit
material type		elastic	
thickness	d	0.28	m
unit weight	γ	25.0	kN/m^3
Young's modulus	E_1	8.3	GPa
Young's modulus	E_2	34.0	GPa
Poisson's ratio	ν'	0.2	-
shear modulus	G_{12}	14.2	GPa
shear modulus	G_{13}	14.2	GPa
shear modulus	G_{23}	14.2	GPa
interface reduction factor	R_{inter}	1.0	-

- **Material parameters used in large-scale model – Block 20**

Tab. 24: Waling parameters

parameter		value	unit
structural element		beam	
material type		elastic	
Young's modulus	E	210.0	GPa
unit weight	γ	78.5	kN/m^3
Cross section area	A	8.68E-03	m^2
Moment of Inertia	I_2	3.66E-04	m^4
	I_3	1.05E-04	m^4
Note: The parameters are taken from a reference model in the Plaxis manual.			

Tab. 25: Strut parameters

parameter		value	unit
structural element		beam	
material type		elastic	
spacing	a	2.5	m
Young's modulus	E	210.0	GPa
unit weight	γ	78.5	kN/m^3
Beam type		Predefined	
Predefined beam type		Circular tube	
Diameter	D	406.4	mm
Thickness	t	10	mm
Note: The struts are considered as circular tube structure (406,4x10 mm).			

Tab. 26: Massive concrete wall parameters

parameter		value	unit
structural element		plate	
material type		elastic	
thickness	d	0.8	m
unit weight	γ	25	kN/m^3
Young's modulus	E	30.0	GPa
Poisson's ratio	ν'	0.2	-
shear modulus	G	12.5	kPa
interface reduction factor	R_{inter}	1.0	-

Tab. 27: Soil nail parameters (tunnel stop wall support)[10]

parameter		value	unit
structural element		embedded beam	
spacing		1.5x1.5	m
connection		hinged	
material type		elastic	
behaviour option		rock bolt	
predefined beam type	massive circular beam		
inclination angle	α	10	°
length	l	10	m
Young's modulus	E	20.0	GPa
bulk unit weigth	γ	0.0	kN/m^3
diameter	D_g	0.13	m
axial skin resistance	layer dependent		
skin resistance	T_{max}	25 (assumption)	kN/m
base resistance	F_{foot}	0.0	kN

Tab. 28: Tunnel stop wall parameters

parameter		value	unit
structural element		plate	
material type		elastic	
thickness	d	0.8	m
unit weight	γ	25	kN/m^3
Young's modulus	E	30.0	GPa
Poisson's ratio	ν'	0.2	-
shear modulus	G	12.5	GPa
interface reduction factor	R_{inter}	0.95	-
Note: The thickness was increased due to convergency reasons.			

---

[10] The Young's modulus E of the soil nails is predominantly governed by the material properties of the grouted body. The herein used E-value complies with soil nail parameters applied in Tschuchnigg (2013).

- **Material parameters used in large-scale model – Block 18**

Tab. 29: Roof slab and header bar parameters

parameter		value	unit
structural element		continuum	
material type		elastic	
type		non-porous	
thickness I height	d I h	1	m
unit weight	γ	25	kN/m^3
Young's modulus	E	34.0	GPa
Poisson's ratio	ν'	0.2	-
shear modulus	G	14.2	GPa
interface reduction factor	R_{inter}	1.0	-

Tab. 30: Pile wall parameters (explicitly modelled piles)

parameter		value	unit
structural element		continuum	
material type		elastic	
type		non-porous	
diameter	D	1.2	m
unit weight	γ	25	kN/m^3
Young's modulus	E	33.0	GPa
Poisson's ratio	ν'	0.2	-
shear modulus	G	13.8	GPa
interface reduction factor	R_{inter}	0.95	-

Tab. 31: Pile wall parameters (simplified as diaphragm wall)

parameter		value	unit
structural element		continuum	
material type		elastic	
type		non-porous	
equivalent thickness	D_{eq}	1.04	m
unit weight	γ	25	kN/m^3
equivalent Young's modulus	E_{eq}	28.7	GPa
Poisson's ratio	ν'	0.2	-
equivalent shear modulus	G_{eq}	12.0	GPa
interface reduction factor	R_{inter}	1.0	-

Assuming both, the same flexural rigidity *EI* as well as axial stiffness compared to the explicitly modelled pile wall, the equivalent thickness D_{eq} as well as the equivalent Young's modulus E_{eq} of the diaphragm wall are calculated based on Equations (C.1-2):

$$(E \cdot A)_{Pile\ wall} = D_{eq} \cdot E_{eq} \tag{C.1}$$

$$(E \cdot I)_{Pile\ wall} = \frac{E_{eq} \cdot {t_{eq}}^3}{12} \tag{C.2}$$

Tab. 32: Lateral shotcrete wall parameters

parameter		value	unit
structural element		plate	
material type		elastic	
thickness	d	0.2	m
unit weight	γ	25	kN/m^3
Young's modulus	E	30.0	GPa
Poisson's ratio	ν'	0.2	-
shear modulus	G	12.5	GPa
interface reduction factor	R_{inter}	0.95	-

Tab. 33: Lateral soil nail parameters (*rdb*)[11]

parameter		value	unit
structural element		embedded beam	
spacing		1.15x1.25 (hxb)	m
connection		hinged	
material type		elastic	
behaviour option		rock bolt	
predefined beam type	massive circular beam		
inclination angle	α	10	°
length	l	12	m
Young's modulus	E	20.0	GPa
bulk unit weigth	γ	0.0	kN/m^3
diameter	D_g	0.13	m
axial skin resistance		layer dependent	
skin resistance	T_{max}	23	kN/m
base resistance	F_{foot}	0	kN
Note: The skin resistance is set in accordance with recommendations given by the on-site geotechnical supervisor.			

---

[11] The Young's modulus E of the soil nails is predominantly governed by the material properties of the grouted body. The herein used E-value complies with soil nail parameters applied in Tschuchnigg (2013).

Tab. 34: Lateral soil nail parameters (*ldb*)

Grout body			
parameter		**value**	**unit**
structural element		embedded beam	
spacing		1.0x1.0	m
material type		elastic	
behaviour option		grout body	
predefined beam type	massive circular beam		
inclination angle	α	10	°
length	l	11	m
Young's modulus	E	20.0	GPa
bulk unit weigth	γ	0.0	kN/m^3
diameter	D_g	0.13	m
axial skin resistance		layer dependent	
skin resistance	T_{max}	23	kN/m
base resistance	F_{foot}	0	kN
Node-to-node-anchor			
parameter		**value**	**unit**
structural element	node-to-node-anchor		
spacing		1.0x1.0	m
material type		elastic	
axial stiffness	EA	1.0E+05	kN
inclination angle	α	10	°
length	l	1	m
Note: It was necessary to model the soil nails (ldb) as ground anchors. However, since the embedded beam elements predominantly determine the structural behaviour of these ground anchors, the ground anchors show almost the same behaviour as the soil nails (rdb). The skin resistance is set in accordance with recommendations given by the on-site geotechnical supervisor.			

Tab. 35: Reinforced invert parameters

parameter		**value**	**unit**
structural element		plate	
material type		elastic	
thickness	d	0.4	m
unit weight	γ	0.0	kN/m^3
Young's modulus	E	31.0	GPa
Poisson's ratio	ν'	0.2	-
shear modulus	G	12.9	GPa

Tab. 36: Vertical soil nail parameters (micropiles)

parameter		value	unit
structural element		embedded beam	
spacing		1.0x1.0	m
connection		free	
material type		elastic	
behaviour option		pile	
predefined beam type	massive circular beam		
length	l	5.5	m
Young's modulus	E	20.0	GPa
bulk unit weigth	γ	0.0	kN/m^3
diameter	D_g	0.13	m
axial skin resistance		layer dependent	
skin resistance	T_{max}	40	kN/m
base resistance	F_{foot}	0	kN

Tab. 37: Pre-stressed anchor parameters

Grout body			
parameter		**value**	**unit**
structural element		embedded beam	
spacing		1.0x1.0	m
material type		elastic	
behaviour option		grout body	
predefined beam type	massive circular beam		
length	l	3.4	m
Young's modulus	E	20.0	GPa
bulk unit weigth	γ	0.0	kN/m^3
diameter	D_g	0.13	m
axial skin resistance		linear	
skin resistance at pile top	$T_{top,max}$	25	kN/m
skin resistance at pile bottom	$T_{bot,max}$	25	kN/m
base resistance	F_{foot}	0	kN
Node-to-node-anchor			
parameter		**value**	**unit**
structural element	node-to-node-anchor		
spacing		1.0x1.0	m
material type		elastic	
axial stiffness	EA	5.5E+04	kN
length	l	2.5	m
$F_{prestress}$		85	kN
Note: The skin resistance is set in accordance with the geotechnical report.			